AD-A007 335

AN EXPERIMENTAL INVESTIGATION OF THE
BOUNDARY LAYER UNDER PACK ICE

Miles G. McPhee

Washington University

Prepared for:

Office of Naval Research

January 1975
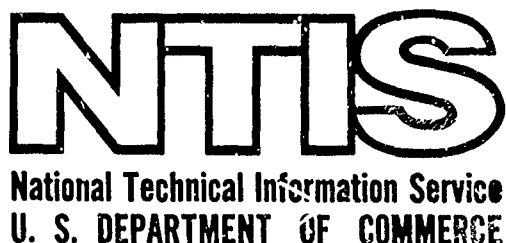
REPORT DOCUMENTATION PAGE	READ INSTRUCTIONS BEFORE COMPLETING FORM

1. REPORT NUMBER	2. GOVT ACCESSION NO.	3. RECIPIENT'S CATALOG NUMBER
T.R. #14 and T.R. #3		AD/A-007 335

4. TITLE (and Subtitle)	5. TYPE OF REPORT & PERIOD COVERED
An Experimental Investigation of the Boundary Layer Under Pack Ice	
	6. PERFORMING ORG. REPORT NUMBER

7. AUTHOR(s)	8. CONTRACT OR GRANT NUMBER(s)
Miles G. McPhee	N-00014-67-A-0103-0021
	N-00014-67-A-0103-0034

9. PERFORMING ORGANIZATION NAME AND ADDRESS	10. PROGRAM ELEMENT, PROJECT, TASK AREA & WORK UNIT NUMBERS
University of Washington Department of Oceanography Seattle, Washington 98195	Project 307-326 Project 307-354

11. CONTROLLING OFFICE NAME AND ADDRESS	12. REPORT DATE
Office of Naval Research Arctic Program Code 461 Arlington, Virginia 22217	January 1975
	13. NUMBER OF PAGES
	176

14. MONITORING AGENCY NAME & ADDRESS(If different from Controlling Office)	15. SECURITY CLASS. (of this report)
	15a. DECLASSIFICATION/DOWNGRADING SCHEDULE

16. DISTRIBUTION STATEMENT (of this Report)

Approved for public release; distribution unlimited.

17. DISTRIBUTION STATEMENT (of the abstract entered in Block 20, if different from Report)

18. SUPPLEMENTARY NOTES

19. KEY WORDS (Continue on reverse side if necessary and identify by block number)
Oceanographic data
Physical oceanographic data
Boundary layer
Pack ice
Arctic Ocean

20. ABSTRACT (Continue on reverse side if necessary and identify by block number)

Measurements of the mean and turbulent flow structure under pack ice were made during the 1972 AIDJEX Pilot Study with small mechanical current meter triplets on three separate masts at several depths throughout the entire rotational boundary layer. In this work the analog between the ice-ocean boundary layer and the surface-atmospheric boundary layer has been explored in detail with composite averages of measured Reynolds stress and mean flow compared to predictions of recent atmospheric models.

DD FORM 1473   EDITION OF 1 NOV 65 IS OBSOLETE   Unclassified   **PRICES SUBJECT TO CHANGE**

20.   The most significant measurements were made during periods of maximum steady ice drift during a storm. Density structure, measured with a CTD probe, showed a well-mixed layer of near neutral stability extending to about 35 m bounded below by a strongly stable pycnocline. This depth corresponded closely to the depth of frictional influence observed during the peak wind period, as indicated by turning of the velocity vector, and from consideration of the turbulent energy profile.

The skin friction velocity, u_*, was determined from momentum flux (Reynolds stress) measurements at 2m and 4m from the ice and consideration of the mean momentum equation. It was found that the combined effect of local pressure gradients and advective accelerations due to topographic variations could not be ignored and an estimate of this effect was included in the calculation. u_* was found to be $1.0 \pm .1$cm-sec^{-1} when the ice velocity relative to the base of the mixed layer was 24cm-sec^{-1}.

Turbulence measurements, when non-dimensionalized by u_*, ρu_*^2, and u_*/f for velocity, stress, and length respectively, fit predictions from recent neutrally buoyant, horizontally homogeneous PBL models quite well, as did the mean longitudinal velocity component. The mean flow component perpendicular to the surface stress (the integral of which is proportional to the total surface stress when averaged over a suitable area) was found to depart markedly from model predictions indicating that form drag associated with pressure ridge keels is an important part of the total drag. A quantitative estimate was made of this effect, and a total drag coefficient, $c_D = \tau_S/\rho V_R^2$, was found to be 3.4×10^{-3} where τ_S is the total average stress on the ice and V_R is the ice velocity relative to the depth of the frictional boundary layer. The ratio of form drag to skin friction was .9.

Composite spectra for the velocity components behaved qualitatively like similar spectra for the atmosphere, exhibiting a -5/3 slope over about a decade along the wave number axis. Peaks in the weighted spectra of vertical velocity components were used to derive a K (eddy viscosity) distribution related to dominant eddy size that agrees well with the PBL models.

Baroclinic currents of considerable magnitude were observed in the pycnocline region and were related to time changes in the density field. It is argued that these secondary currents result from convergence along the top of the pycnocline as a result of Ekman pumping in the mixed layer.

UNIVERSITY OF WASHINGTON
DEPARTMENT OF OCEANOGRAPHY
Seattle, Washington 98195

Technical Report

AN EXPERIMENTAL INVESTIGATION OF THE

BOUNDARY LAYER UNDER PACK ICE

by

Miles Gordon McPhee
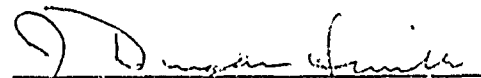
J. DUNGAN SMITH
PRINCIPAL INVESTIGATOR
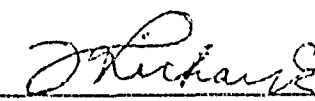
FRANCIS A. RICHARDS
ASSISTANT CHAIRMAN FOR RESEARCH

ABSTRACT

Measurements of the mean and turbulent flow structure under pack ice were made during the 1972 AIDJEX Pilot Study with small mechanical current meter triplets on three separate masts at several depths throughout the entire rotational boundary layer. In this work the analog between the ice-ocean boundary layer and the surface-atmospheric boundary layer has been explored in detail with composite averages of measured Reynolds stress and mean flow compared to predictions of recent atmospheric models.

The most significant measurements were made during periods of maximum steady ice drift during a storm. Density structure, measured with a CTD probe, showed a well-mixed layer of near neutral stability extending to about 35 m bounded below by a strongly stable pycnocline. This depth corresponded closely to the depth of frictional influence observed during the peak wind period, as indicated by turning of the velocity vector, and from consideration of the turbulent energy profile.

The skin friction velocity, u_*, was determined from momentum flux (Reynolds stress) measurements at 2 m and 4 m from the ice and consideration of the mean momentum equation. It was found that the combined effect of local pressure gradients and advective accelerations due to topographic variations could not be ignored and an estimate of this effect was included in the calculation. u_* was found to be $1.0 \pm .1$ cm-sec^{-1} when the ice velocity relative to the base of the mixed layer was 24 cm-sec^{-1}.

Turbulence measurements, when non-dimensionalized by u_*, ρu_*^2, and u_*/f for velocity, stress, and length respectively, fit predictions from

ie —

recent neutrally buoyant, horizontally homogeneous PBL models quite well,
as did the mean longitudinal velocity component. The mean flow component
perpendicular to the surface stress (the integral of which is proportional
to the total surface stress when averaged over a suitable area) was found
to depart markedly from model predictions indicating that form drag asso-
ciated with pressure ridge keels is an important part of the total drag.
A quantitative estimate was made of this effect, and a total drag coeffi-
cient, $c_D = \tau_s/\rho V_R^2$, was found to be 3.4×10^{-3} where τ_s is the total
average stress on the ice and V_R is the ice velocity relative to the depth
of the frictional boundary layer. The ratio of form drag to skin friction
was .9.

Composite spectra for the velocity components behaved qualitatively
like similar spectra for the atmosphere, exhibiting a $-5/3$ slope over about
a decade along the wave number axis. Peaks in the weighted spectra of
vertical velocity components were used to derive a K (eddy viscosity) dis-
tribution related to dominant eddy size that agrees well with the PBL models.

Baroclinic currents of considerable magnitude were observed in the
pycnocline region and were related to time changes in the density field.
It is argued that these secondary currents result from convergence along
the top of the pycnocline as a result of Ekman pumping in the mixed layer.

ii

Table of Contents

iv

List of Tables

v

List of Figures

ACKNOWLEDGMENTS

1. INTRODUCTION

Understanding the complex mechanism by which a turbulent flow exerts force on a surface bounding it has long been of central importance to the study of fluid dynamics. A large body of knowledge has been accumulated about fluid forces that are commensurate with ordinary experience such as drag on airplanes, wind force on buildings, head loss in pipes, etc.; largely because these flows are amenable to direct measurement or simple similarity modeling and practical application of knowledge about them is readily apparent. In the larger scale boundary layers of the oceans and atmosphere the Coriolis force (the apparent force arising from the fact that our reference frame, the earth, is rotating) plays an essential role in boundary layer dynamics, even though it is detectable to our senses only by inference. Thus even a steady-state, horizontally homogeneous idealization presents the formidable problem of describing the three-way balance between a driving force, the Coriolis force, and the gradient of turbulent momentum flux.

In recent years, methods of analysis and tools for turbulence measurement have improved to the point that they can greatly increase our knowledge of turbulent, rotating boundary layers. At the same time, demand for such knowledge has been spurred by evermore sophisticated weather-prediction schemes and pollutant-dispersal research. With the advent of large computers for problem solving and increased interest in general, we seem to be in a period of rapid progress toward understanding the planetary boundary layers. However, when we consider the lack of reliable measurements and the fact that the theory largely ignores time dependence and horizontal topographic

variation, we can safely say that the questions still outnumber the answers by a wide margin.

In 1970, a large, interdisciplinary project called AIDJEX (an acronym for Arctic Ice Dynamics Joint Experiment) was instigated with the goal of elucidating the intricate interaction between sea ice and its environment. The fact that ice motion is governed largely by stresses exerted on it from the atmosphere and ocean provided the impetus for a series of field experiments designed to measure wind and water stress. One phase of the measurement program, dealing with water stress, was carried out by an oceanographic boundary layer research group from the University of Washington.

This dissertation concerns measurements made by that group at the 1972 AIDJEX Pilot Study camp. In it, we have compared these data to predictions of recent theoretical work, pointing out similarities where they exist and attempting to identify sources of disagreement. The objectives of this extensive experiment can probably best be viewed on three levels of increasing generality. First, to satisfy the immediate goals of AIDJEX we needed to determine the total stress exerted on the ice by the ocean during times when the wind stress and ice strain were also being monitored. One of the primary objectives of AIDJEX is a predictive model of ice motion and thickness as a function of relatively easily measured, large scale variables. The importance of an accurate water stress model becomes clear when we consider that oftentimes the relatively small difference between a driving ind stress and a retarding ocean drag must account for such interesting features as pressure ridges and open leads. This is by no means a simple problem, since the total stress is a sum of contributions from surface

friction, form drag and possibly wave drag, although the latter is not considered in this work.

Secondly, it was recognized that the ice could provide a unique platform from which to make measurements in the upper layers of a deep ocean. The dynamics of the mixed layer of the ocean, although extremely important to the interaction between air and sea, are poorly understood, largely because of a lack of good data. When the ice is moving, it provides an excellent vehicle from which to suspend probes for measuring such things as turbulence. Clearly, in more temperate oceans, waves (which make measurements so difficult) must play an important role in the mixed layer and extrapolating directly from an ice-covered ocean is of doubtful validity. Nevertheless, it was felt our data could provide a base to which wave-induced effects could be added.

The broadest aim of the experiment was to shed light on the dynamics of planetary boundary layers in general. In spite of the fact that the idealized neutral rotating boundary layer is felt to be theoretically well understood, there is a notable lack of real data, particularly turbulence data, against which to check the theories. We felt that the remarkable similarity between boundary layers resulting from ice being pushed across a slow moving ocean and from a large pressure-gradient wind in the atmosphere could be exploited, particularly since scales in the ocean are much more amenable to instrumentation. Thus it was hoped that our project would prove to be significant to atmospheric scientists as well as oceanographers.

With the exception of Chapter 10, which deals with baroclinic activity in the pycnocline and is more or less independent, this work is intended to have a continuous development. In Chapter 2 the planetary boundary

layer is described in general terms; Chapter 3 presents specific models. In Chapter 4, the actual experiment is described and in Chapter 5 the density structure of the mixed layer is explored both in theory and with data. Chapters 6, 7, and 8 are devoted to presenting the data in the framework of the theory and models. In Chapter 9 spectral analysis of the data is discussed and used to bolster some of the arguments developed previously. Finally, in Chapter 11 the results are used to synthesize a method for estimating a regional stress value and drag coefficient for the ice stress in terms of ice drift velocity.

An almost overwhelming amount of data was collected during this experiment-- 75 current meter channels sampling every 50 msec were recorded almost continuously for three weeks. Obviously, presenting these data in some cogent manner required a great deal of distillation, and undoubtedly evidence of some interesting phenomena was lost during the process. No claim is made that this paper is a complete summary of the data collected during the project; rather, it represents the author's judgement of what features are particularly relevant to modern boundary layer theory.

2 THE PLANETARY BOUNDARY LAYER

2.1 Background

A great deal of the success of modern fluid-dynamical theory can be traced to Prandtl's idea that a large-Reynolds-number regime can be broken conceptually into a frictionless flow bounded by a thin layer in which frictional effects act to bring the fluid to rest at a solid boundary. Without friction, many flows are amenable to concise and aesthetically pleasing mathematical descriptions (e.g., see Batchelor, 1967) or at least to fairly accurate computer modeling, and the fact that such flows are observed in nature lends credence to Prandtl's conceptual tool.

Boundary layers, particularly turbulent ones, are not nearly so well understood; yet as our understanding of the large scale features of geophysical flows increases, the importance of understanding how the relatively small boundary layer affects such flows becomes more and more significant.

There is also a great deal of intrinsic interest in the boundary layer itself, a fact which should be clear since, for instance, a small change in the conditions of the atmospheric boundary layer can significantly alter our lives (picture Tacoma without the effects of a smelter). To relate closer to our specific project, the prediction of water and wind stress on pack ice is largely a boundary layer problem although the driving forces are of synoptic scale.

This chapter deals with general features of the planetary boundary layer (sometimes hereafter abbreviated PBL). Description of specific models is deferred to Chapter 3.

2.2 The Equations of Motion

The equations governing flow in a boundary layer measured from a rotating reference frame with the x_3 axis oriented vertically can be written down in vector notation with the Einstein summation convention as follows:

The Boussinesq momentum equation--

$$\frac{\partial \tilde{u}_i}{\partial t} + \tilde{u}_j \frac{\partial}{\partial x_j} \tilde{u}_i + 2\omega\varepsilon_{ijk} n_j \tilde{u}_k = -\frac{1}{\rho_o} \frac{\partial \tilde{p}}{\partial x_i} - g \frac{\rho'}{\rho_o} \delta_{i3} + \frac{\partial}{\partial x_j} \tilde{\tau}_{ji} \qquad (2.2.1)$$

where $\tilde{u}_i$ is the instantaneous velocity vector in a frame fixed

with respect to the earth;

ωn_j is the earth's rotation vector;

$\tilde{p}$ is the instantaneous pressure with the hydrostatic part,

$p_o = p_s - \rho_o gz$, removed;

ρ' is the deviation of density from the mean state, ρ_o;

$\tilde{\tau}_{ij}$ is the instantaneous deviatior stress tensor, and

δ_{ij} and ε_{ijk} have the commonly accepted properties.

The continuity equation for an incompressible fluid--

$$\frac{\partial u_i}{\partial x_i} = 0 \qquad (2.2.2)$$

The Newtonian constitutive relation for an incompressible fluid--

$$\tilde{\tau}_{ij} = \mu(\frac{\partial \tilde{u}_i}{\partial x_j} + \frac{\partial \tilde{u}_j}{\partial x_i}) \qquad (2.2.3)$$

A complete specification would also include an equation of state for density as a function of pressure, temperature and salinity; the energy equation; a heat conduction equation; a salt diffusion equation; and an

equation of state for internal energy. These are not written down since they will not be referred to explicitly.

We can write an arbitrary instantaneous quantity, $\tilde{g}$, as the sum of a mean, G, and fluctuating, g, parts:

$$\tilde{g} = G + g \qquad \text{where } G = \frac{1}{T} \int_{-T/2}^{T/2} \tilde{g} \, dt \qquad (2.2.4)$$

and

$$\bar{g} = \frac{1}{T} \int_{-T/2}^{T/2} g \, dt = 0$$

Rigorously, the averaging would be done over T as $T \to \infty$, and terms like $\frac{\partial G}{\partial t}$ would be meaningless. It is convenient to anticipate that large scale driving features in many geophysical flows are tuned to a much lower frequency band than the turbulent features and thus we can retain terms like $\frac{\partial G}{\partial t}$ if it is understood that the time scales involved are large compared to the averaging intervals. Another way of viewing this is to consider the Reynolds averaging process as a low-pass filter.

Applying the Reynolds decomposition (2.2.4) to the momentum equation, (2.2.1), invoking the constitutive relation (2.2.3) where the kinematic viscosity, ν, has replaced μ, along with the incompressibility condition (2.2.2), and averaging we have the mean momentum equation:

$$\frac{\partial U_i}{\partial t} + U_j \frac{\partial}{\partial x_j} U_i + 2\omega \varepsilon_{ijm} n_j U_m = -\frac{1}{\rho_o} \frac{\partial p}{\partial x_i} + \nu \frac{\partial^2 U_i}{\partial x_j \partial x_j} - \frac{\partial}{\partial x_j} \overline{u_i u_j} \quad (2.2.5)$$

where

$$\frac{\partial}{\partial x_j} \overline{u_i u_j} = \overline{u_j \frac{\partial}{\partial x_j} u_i}$$

as a result of the incompressibility condition.

If we subtract the mean equation from the instantaneous equation, multiply the result by u_k, average, then interchange indices and sum, we arrive at the turbulence covariance equations for a rotating reference frame (Wyngaard et al., 1973; see also Mellor and Herring, 1973):

$$\frac{\partial}{\partial t}\overline{u_i u_k} + U_j\frac{\partial}{\partial x_j}\overline{u_i u_k} + \overline{u_k u_j}\frac{\partial U_i}{\partial x_j} + \frac{\partial}{\partial x_j}\overline{u_i u_k u_j}$$

$$= \frac{-1}{\rho_o}\left(\overline{u_k\frac{\partial p}{\partial x_i}} + \overline{u_i\frac{\partial p}{\partial x_k}}\right) - \frac{g}{\rho_o}\left(\overline{\rho' u_k}\delta_{i3} + \overline{\rho' u_i}\delta_{k3}\right) \qquad (2.2.6)$$

$$- 2\omega\left(\varepsilon_{ijm}n_j\overline{u_m u_k} + \varepsilon_{kpq}n_p\overline{u_i u_q}\right) - 2\nu\overline{\frac{\partial u_i}{\partial x_j}\frac{\partial u_i}{\partial x_j}}$$

where the diffusive viscous dissipation term has been dropped from consideration of scaling arguments (J. Wyngaard, personal communication).

We can obtain the turbulent energy budget by contracting (2.2.6) on the index i and carrying out the implied sum:

$$\frac{\partial}{\partial t}\left(\frac{\overline{q^2}}{2}\right) + U_j\frac{\partial}{\partial x_j}\left(\frac{\overline{q^2}}{2}\right) + \overline{u_i u_j}\frac{\partial U_i}{\partial x_j} + \frac{1}{2}\frac{\partial}{\partial x_j}\left(\overline{u_i u_i u_j}\right)$$

$$= -\overline{u_i\frac{\partial p}{\partial x_i}} - \frac{g}{\rho_o}\overline{\rho' u_i}\delta_{i3} - 2\nu\overline{\frac{\partial u_i}{\partial x_j}\frac{\partial u_i}{\partial x_j}} \qquad (2.2.7)$$

where $\overline{q^2} = \overline{u_i u_i}$.

The mean momentum equation, (2.2.5) can be greatly simplified by noting that $W = 0$, that derivatives in the vertical are much larger than those in the horizontal, and that the Reynolds stress term, $\overline{u_i u_j}$, is much larger than the viscous stress term for geophysical flows. With these constraints,

$$\frac{\partial U_i}{\partial t} + U_j\frac{\partial}{\partial x_j}U_i + 2\omega\varepsilon_{ijk}n_j U_k = -\frac{1}{\rho_o}\frac{\partial p}{\partial x_i} - \frac{\partial}{\partial z}\overline{u_i w} \qquad (2.2.8)$$

To this point, we have considered velocity vectors in a frame fixed
with respect to the earth. Since our measurements were made from an ice
platform being pushed across the sea surface by the wind, it is convenient
to put the equations in a reference frame fixed to the ice.
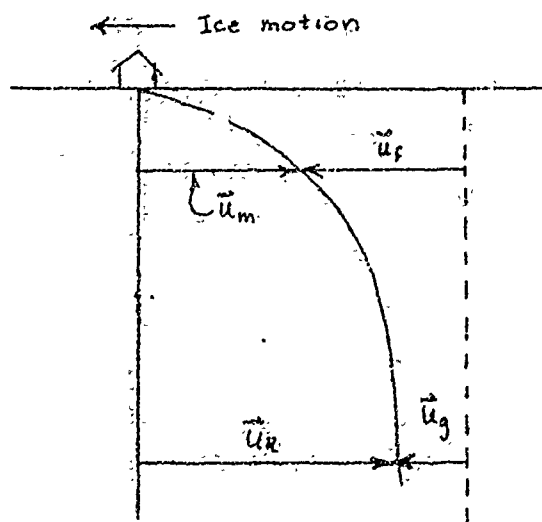
If $\vec{u}_f$ is the velocity vector in a frame fixed with respect to the earth,
$\vec{u}_m$ is the velocity measured with respect to the moving ice, and $\vec{u}_R$ is a
reference velocity, that is, the mean velocity at some level where fric-
tional effects vanish and the mean geostrophic flow of the ocean, $\vec{u}_g$,
accounts for any absolute velocity. If $\vec{u}_g$ is identified with a large
geostrophic pressure gradient in the ocean, then using the vector equivalence,
$\vec{u}_m - \vec{u}_R = \vec{u}_f - \vec{u}_g$, allows us to subtract the geostrophic pressure gradient from
the momentum equation leaving only pressure gradients due to local topogra-
phic or possibly baroclinic effects. The reference level was chosen to be
32 m since that was the deepest triplet still in the mixed layer (see
Chapter 5). Comparison with smoothed acoustic bottom reference (ABR) data
during steady times showed that the mean measured velocity at 32 m tracked
the apparent bottom velocity quite closely, implying that the geostrophic
flow was small compared to ice motion. (For a brief description of the ABR,

see Martin and Thorndike, 1972). A reference level above the pycnocline was chosen to avoid the effects of internal waves and other baroclinic features often observed in a steep density gradient.

With these changes, and the Coriolis parameter, f, defined by $f = 2\Omega \cos\phi$, where Ω is the earth's rotation rate and ϕ is the latitude, the mean steady-state component equations are

$$-\frac{\partial}{\partial z}(\overline{uw}) - f(V - V_R) = F_x = -\frac{1}{\rho_o}\frac{\partial P_{local}}{\partial x} - U\frac{\partial U}{\partial x} + \ldots$$

$$\frac{\partial}{\partial z}(\overline{vw}) + f(U - U_R) = F_y = -\frac{1}{\rho_o}\frac{\partial P_{local}}{\partial y} - U\frac{\partial V}{\partial x} + \ldots$$

(2.2.9)

where the dots represent other horizontally inhomogeneous terms not considered as important as those written explicitly.

If conditions are horizontally homogeneous, so that the right-hand sides of Equations (2.2.9) vanish, the equations are just analogous to the defect law in the atmospheric boundary layer, where the velocity profile must go from zero at the ground to a geostrophic value aloft driven by a nearly constant large-scale pressure gradient. Thus it turns out that in the idealized case, the current measured under a wind-driven ice floc is just the mirror image of the actual wind, if each is scaled properly. This similarity provides a basis for comparing measurements made in the ocean to recent models of atmospheric boundary layers. In fact, due to the rigid surface imposed by the ice, one might expect the ice-ocean boundary layer to be more similar to the atmosphere than to the boundary layer under an unfrozen air-sea interface.

2.3 Scales and General Features of the PBL

If we simplify the problem of flow near the ice to one that is hori-
zontally homogeneous and steady with a constant surface roughness character-
ized by a length, z_o, in a neutrally bouyant fluid, the flow can be specified
by four external parameters; for instance, the surface friction velocity,
$u_* = \sqrt{\tau_s/\rho}$, where τ_s is the surface stress; the Coriolis parameter, f; the
surface roughness, z_c; and the distance from the boundary, z. Thus any
other flow parameter, say the true lateral velocity, $V - V_R$, when non-
dimensionalized by proper scaling, can be expressed as a universal function
of two other non-dimensional groups formed from the external parameters.
For the example cited, we could write

$$\frac{V-V_R}{u_*} = G(fz/u_*, z/z_o) \qquad \frac{U-U_R}{u_*} = J(fz/u_*, z/z_o) \qquad (2.3.1)$$

That u_* and u_*/f are the proper velocity and length scales for the
neutral outer layer is well established in the literature. Blackadar and
Tennekes (1968) argue that if $\underline{h}$ is the boundary layer thickness, u_*, emerges
as a scale from an analysis of the turbulent energy budget as $h/z_o \to \infty$,
although it is not clear that this is more fundamental than eliminating the
other possible scales, f_o and fz, on the grounds that the former is
typically far too small and the latter increases with distance from the
boundary while the true velocity approaches a geostrophic value that is
often small compared to ice drift.

If we form a ratio of the dimensionless groups z/z_o and fz/u_* we have
$u_*/fz_o = Ro_*$, for which the term "surface-friction Rossby number" has been
coined by Blackadar and Tennekes (1968). For geophysical flows this ratio

is large; thus we infer that these two parameters must affect the flow at quite different scales. This leads directly to the concepts of an _inner_ or _surface_ layer vis-a-vis an _outer_ or _Ekman_ layer.

In the surface layer we expect z small, so that $fz/u_* \to 0$ and the flow at this scale loses its explicit dependence on the large scale measures. If we let $\zeta = z/z_o$, then:

$$\frac{V - V_R}{u_*} = G_s(\zeta) \quad , \quad \frac{U - U_R}{u_*} = J_s(\zeta) \qquad (2.3.2)$$

From (3.2.9), where $F_x = F_y = 0$ and

$$T_x = - \overline{uw}/u_*^2 \quad , \quad T_y = -\overline{vw}/u_*^2$$

we have

$$G_s(\zeta) = -Ro_* \frac{\partial}{\partial \zeta} T_x$$

$$J_s(\zeta) = -Ro_* \frac{\partial}{\partial \zeta} T_y \qquad (2.3.3)$$

Clearly, in the limit $Ro_* \to \infty$

$$\frac{\partial T_x}{\partial \zeta} = \frac{\partial T_y}{\partial \zeta} = 0 \qquad (2.3.4)$$

If the x-axis is chosen to coincide with the direction of surface stress we see that $T_x = 1$ and $T_y = 0$ for the surface layer. Ro_* is finite, however, so that the usefulness of the surface layer concept depends directly on the magnitude of Ro_* (Tennekes, 1973).

In the outer layer, $\zeta \to \infty$ and we conclude that the profiles must depend on $\xi = fz/u_*$. We have:

$$\frac{V - V_R}{u_*} = G_o(\xi) = \frac{-\partial T_x}{\partial \xi} \quad , \quad \frac{U - U_R}{u_*} = J_o(\xi) = \frac{\partial T_y}{\partial \xi} \qquad (2.3.5)$$

Equations (2.3.4) and (2.3.5) demonstrate the paradox that arises

if we attempt to describe the large-Rossby-number boundary layer by one

length scale. According to (2.3.5) the stress gradient should reach a

maximum as the flow approaches the surface. But in the surface layer pro-

per, the stress gradient is zero by (2.3.4), and we are forced to conclude

that each scale has its own region of influence as we postulated to begin

with. In the following sections we will investigate some of the properties

of the inner and outer layers of the PBL.

2.4 The Logarithmic Profile in the Surface Layer

A concept that has proved successful in describing the mean features of some turbulent flows is that of an eddy viscosity, or momentum diffusivity, which provides a constitutive relation between the Reynolds stress and the rate of strain of the mean flow. We can write for example,

$$\overline{uw} = -K \frac{\partial U}{\partial z}$$

where $K \simeq v\ell$, v and ℓ being characteristic velocity and length scales of the turbulent flow, by analogy to the treatment of molecular viscosity in the kinetic theory of gases. The scale ℓ is associated with the size of the large eddies that account for turbulent mixing. As Tennekes and Lumley (1972, Chapter 1) point out, this is conceptually dangerous in that it ascribes to the fluid a property of the flow. But it makes the mathematics simpler, and as long as its limitations are recognized, can often provide very useful results.

Near the surface, the size of turbulent eddies is limited by the distance from the boundary, z, and it seems reasonable that $\ell \to z$. Also, since the stress, $\overline{uw}$, is relatively constant near the boundary $u_* = \sqrt{\tau_b/\rho}$ appears as a natural velocity scale and we have

$$K \sim u_* z$$

The relationship is made concrete with the introduction of von Karman's constant, k, and considering the dimensionless stress equation in the limit $Ro_* \to \infty$, we have

$$kz/u_* \frac{\partial U}{\partial z} = 1$$

This can be integrated to give

$$U = \frac{u_*}{k} \ln z/z_o \qquad (2.4.1)$$

In the y-direction the solution is trivial, $V = 0$.

As Tennekes (1973) has pointed out, the surface layer is a useful abstraction, but caution must be used in its application; e.g., von Karman's "constant" is only constant in the limit as $Ro_* \to \infty$. Indeed, Tennekes claims that k varies from an asymptotic value of .33 to the long-accepted .4 and even higher, with decreasing Ro_*. Businger et al. (1971) report a value of .35 after extensive measurements over level, smooth ground in Kansas. At present this seems to be the best value for large Rossby-number flows and will be used where applicable in the remainder of this work.

2.5 Comparison of Oceanic and Atmospheric Scales

For the purposes of this investigation it is useful to compare the
sizes of the respective scales in the atmosphere and under the ice. The
following table summarizes typical approximate values for the neutral
boundary layers.

	Atmosphere	Ocean (ice-covered)
$u_* = \sqrt{\tau_s/\rho}$	30 cm-sec^{-1}	1 cm-sec^{-1}
Surface layer	30 m	1 m
PBL Depth	1000 m	35 m

Table 2.1 Scale Comparisons

From this it is clear that our measurements (from 2 to 54 m) were in
the outer layer and that most micrometeorogical measurements are made in the
surface layer. The large height of the atmospheric Ekman layer accounts
for a dearth of measurements in its outer regions, while the difficulty of
making stationary measurements from shipboard or from a fixed mooring
explains the lack of oceanographic data.

To our knowledge, the data gathered from the ice platform during the
AIDJEX series of experiments represent the first measurements of mean velo-
city and Reynolds stress taken simultaneously throughout an entire planetary
boundary layer.

Another point can be made from the scale comparison in Table (2.1).
We can see by referring to the topographic map, Figure (4-1), that condi-
tions are not horizontally homogeneous, with relief extending through as
much as a tenth of the PBL. On the other hand, the analogous atmospheric

terrain is not mountainous, but rather corresponds to low hills with gentle

slopes.

2.6 Asymptotic Matching and the Geostrophic Drag Law

Blackadar and Tennekes (1968) showed that under the assumptions impli-

cit in expressing the wind profile in the surface layer as a function only

of z/z_o and in the outer layer as a function of fz/u_*, universal relation-

ships amongst the turning angle, α, the geostrophic wind components, the

surface-friction Rossby number, Ro_*, and the friction velocity, u_*, could

be derived. With slight modification their arguments can be applied to

the ice-ocean boundary.

We postulate that some region exists in which the shear can be expressed

as a function of either $\zeta = z/z_o$ or $\xi = fz/u_*$ as each goes to an asymptotic

limit. That is, we postulate a region in which both the inner layer equa-

tion (2.3.2) and the outer layer equation (2.3.5) are valid. Then we can

express the shear as derivatives of the inner and outer layer functions:

$$\frac{\partial U}{\partial z} = u_* \frac{\partial J_s(\zeta)}{\partial \zeta} \frac{\partial \zeta}{\partial z} = \frac{u_*}{z_o} J_s'(\zeta)$$

$$\frac{\partial U}{\partial z} = u_* \frac{\partial J_o(\xi)}{\partial \xi} \frac{\partial \xi}{\partial z} = f J_o'(\xi)$$

But since $u_*/fz_o = Ro_* = \zeta/\xi$

$$J_s'(\zeta) = J_o'(\xi) = constant \qquad (2.6.1)$$

since each side is a function of one argument and each argument is going

asymptotically to a limit.

We can integrate (2.6.1) to get logarithmic profiles in each argument and establish the constants for the surface-layer integration by comparing it to the law of the wall, Equation (2.3.4). We get

$$J_s(\xi) = \frac{1}{k} \ln\zeta - u_R/u_* = J_0(\xi) = \frac{1}{k}(\ln\xi + A) \qquad (2.6.2)$$

Solving for u_R/u_* we get

$$\frac{u_R}{u_*} = \frac{1}{k}(\ln \zeta/\xi - A) = \frac{1}{k}(\ln Ro_* - A) \qquad (2.6.3)$$

For the lateral component, the shear in the matching region is zero and

$$\frac{V_R}{u_*} = -B/k \qquad (2.6.4)$$

The turning angle (the angle the ice drift makes with the applied stress) is given by

$$\alpha = \tan^{-1}\frac{V_R}{u_R} = \tan^{-1}[-B/(\ln Ro_* - A] \qquad (2.6.5)$$

Attempts have been made to extend this type of analysis to non-neutral boundary layers (e.g., Csanady, 1972), but with little success because of the complexities introduced by another variable. Indeed, there is little agreement on the values of the neutral similarity constants A and B in the literature (Shir, 1973, presents a good summary).

For pack ice, Rossby-number similarity may provide a viable way of estimating drag, but its use must be approached with caution. First, the roughness scale, z_0, is not known. In general, it seems as if z_0 might be of the same order as the top surface in which case the surface-friction Rossby number would be considerably smaller than typical atmospheric values, a significant factor since the whole theory depends on the asymptotic

behavior of Ro_*. Also, even relatively smooth ice probably cannot be treated as horizontally homogeneous. On the other hand, the stability structure appears to be nearly neutral and constant under pack ice in contrast to the diabatic atmospheric boundary layers studied in mid-latitudes.

3 MODELING THE OUTER LAYER

3.1 Introduction

Equations (2.2.5) and (2.2.6) demonstrate the closure problem of tur-
bulence. The statistical averaging technique leaves residual terms that
are covariances arising from the non-linear terms in the mean equations.
It is possible to write dynamical equations for these terms also, such as
(2.2.6), but then triple products and other new covariances are introduced,
for which new equations must be written, ad infinitum. In order to solve
equations such as (2.2.5), we must make assumptions about the covariances
that allow the set of equations to be closed.

During this century, a great deal of work has been devoted to searching
for a satisfying theoretical approach to closing the turbulence equations
at first order, i.e., expressing the Reynolds stresses as functions of the
other mean flow parameters. The advent of large computers and sophisticated
numerical techniques has paved the way for alternative solution methods.
For example, it is now possible to integrate the time-dependent, three-
dimensional equations directly. This requires a "closure" of sorts in that
approximations for motions smaller than the grid-scale size must be made.
A third technique is to carry the covariances explicitly in the mean equa-
tions, closing the second-order equations and solving the complete set
simultaneously.

This chapter will describe some specific models in order to lay a theo-
retical framework in which to present actual measurements.

3.2   K-theory and the Ekman Solution

The simplest closure scheme for the simplified mean boundary layer equations, (2.2.9), comes from postulating a constant eddy viscosity. Ekman discovered a solution to this problem for the ocean in 1905 which predicted a spiraling current hodograph and net transport normal to the surface wind.

If the horizontal velocity components are expressed in complex notation

$$W = (U-U_R) + i(V-V_R)$$

and the Reynolds stresses are written

$$\overline{uw} = -K \frac{\partial U}{\partial z} \quad , \qquad \overline{vw} = -K \frac{\partial V}{\partial z} \quad ,$$

with K constant, then for horizontally homogeneous conditions, equations (2.2.9) can be combined to yield

$$W'' + m^2 W = 0 \tag{3.2.1}$$

where the primes denote differentiation with respect to z and $m^2 = if/K$.

Under the constraints that $W \to 0$ as $z \to -\infty$ and

$$W(0) = W_R = -(U_R + iV_R) \quad ,$$

the solution of (2.2.1) is

$$W(z) = W_R e^{mz} ,$$

$$m = \sqrt{f/K} \ e^{i\pi/4} = \sqrt{f/2K} \ (1+i)$$

If the x-axis is chosen to coincide with the velocity at the surface, we can write

$$(U-U_R) = -U_R e^{\gamma z} \cos\gamma z$$

$$V = -U_R e^{\gamma z} \sin\gamma z$$

$$\gamma = \sqrt{f/2K}$$

The stress is given by

$$\Pi(z) = \tau x + i\tau y = K \frac{\partial W}{\partial z}$$

from which

$$\Pi(0) = W_R \sqrt{fK} \, e^{i\pi/4}$$

From this the well-known result that the surface stress is 45 degrees to the left of the surface velocity in the Ekman spiral is apparent.

That a true Ekman spiral has never been observed in natural flows is not too surprising in light of the arguments regarding the proper mixing length for the surface layer cited in Section (2.4): in the surface layer, we expect stress and velocity to be in the same direction. However, if the outer layer is characterized by a constant mixing length then presumably a level does exist just beyond the surface layer in which the stress is nearly the same as the surface value while the angle between stress and velocity at that level is the proper 45 degrees. This then marks the upper boundary for an Ekman spiral. The relationship between the surface current and the current at this level depends on new parameters such as the surface roughness, z_o, which complicate the problem.

Hunkins (1966), using averaged drogue measurements taken from Arctic Drift Station Alpha during the summer of 1958, and assuming that the surface layer was of negligible depth, fit a constant-eddy-viscosity hodograph to his measurements fairly well. He found that $D = \pi\sqrt{2K/f}$ (the Ekman depth) corresponded closely to the depth of the mixed layer which was 18-20 m. From this, the eddy viscosity was calculated to be 23.8 cm^2-sec^{-1}.

Various two-layer K distribution schemes have been proposed in which an inner-layer mixing length proportional to z is reconciled with an outer layer mixing-length distribution. Evaluation of such models suffers from

a lack of measured data. An excellent summary of several such models

is given by Brown (1973).

3.3 Three-dimensional Numerical Integration

Numerical integrations of the complete equations of motion for the boundary layer provide the most detailed models. Deardorff (1972) has presented such a model for neutral and unstable (upward heat flux) conditions in the atmosphere.

Briefly, Deardorff uses a grid 20 by 40 horizontal by 20 vertical to integrate Equations (2.2.1) to a statistically steady state, replacing the stress term by a sub-grid-scale (SGS) Reynolds stress term and using potential temperature fluctuations for the density term. The SGS Reynolds stresses are related to the gradients of grid-scale velocities by an eddy viscosity which is in turn related to products of velocity gradients times the grid volume.

For the neutral calculations, a rigid lid is imposed at $fz/u_* = .45$, which Deardorff criticizes as giving unrealistic results near the top of the boundary layer. As we will show later however, this height corresponds quite closely to the "lid" imposed by the pycnocline in the natural system we observed.

The lower boundary conditions are assumed governed by surface layer conditions taken from Businger _et al._ (1971), for which $Ro_* = u_*/fz_o = 1.5 \times 10^7$.

Mean profiles (some of which will be shown later along with collected data) are the result of averaging over the horizontal grid points and over an ensemble of ten realizations spaced in time.

General features of the model include the following:

(1) Even slight instability drastically reduces the lateral component in the mean wind profile.

(2) Geostrophic drag (u_*/G) increases significantly with increasing instability.

(3) Slight instability increases the longitudinal component of momentum flux, $-\overline{uw}$, and decreases the lateral momentum flux, $-\overline{vw}$, aloft.

(4) Under unstable conditions, the $-\overline{uw}$ profile appears to fall off linearly to the inversion height in contrast to the neutral case in which it decreases to zero by about $fz/u_* = .3$, and takes small negative values at greater heights.

Simulations like Deardorff's require huge computer memories and are expensive to run. They also suffer from having a "black-box" character (Brown, 1973), making it difficult to isolate cause and effect. A third drawback is that at small scales they are quite sensitive to the assumptions made for SGS motions; this is particularly important in simulations of stable conditions where presumably vertical motions are inhibited. For Deardorff's neutral case, this effect is reportedly confined to the bottom two grid volumes.

3.4 Second-Order Closure Models

Recently, models that carry the mean flow equations in full and make closure assumptions for terms in the turbulence covariance equations have been published. Shir (1973) has modeled the neutral outer boundary layer and Wyngaard et al. (1973) have provided models for the neutral and several unstable cases. The success of each model is gauged against Deardorff's (1972) three-dimensional model, apparently for lack of sufficient outer-layer atmospheric measurements.

Second-order models are much less expensive and easier to incerpret than 3-D simulations, yet at the same time provide more information about the PBL than do first-order solutions: for example, turbulent energy and fluxes of momentum and contaminants are predicted explicitly in both of the models mentioned above.

The closure philosophy for the Wyngaard et al. (1973) model involves writing a dynamic equation for the turbulent energy dissipation rate, $\bar{\epsilon}$, and modeling the unknown terms like the pressure-velocity covariances in the covariance equations, (3.2.6), as expansions about the value the term would have in an isotropic field as suggested by Lumley and Khajeh-Nouri (1973). This becomes a very complex procedure and still requires many ad hoc assumptions about the importance of various constants and terms; e.g., turbulent transport is modeled as gradient diffusion by using a length scale related to the "turn-over" time. Most of the unknown constants in the model are calculated from atmospheric surface-layer data.

Shir (1973) writes a dynamic equation for ℓ from the equation $\bar{\epsilon} = c_o q^2/\ell$, where q^2 is twice the specific turbulent energy. He then models

this equation and equates ℓ to the gradient diffusion length scale. He assumes gradient diffusion for the turbulent and pressure transport terms and writes a complicated equation for the pressure-strain correlation. Constants are estimated approximately and then adjusted to give realistic results. Boundary conditions are specified at the first grid point to match the law of the wall, leaving the surface-friction Rossby number a variable parameter.

Both models agree reasonably well with Deardorff's (1972) model and thus support the general conclusions reached by it. For the neutral layer, it is found that the turbulent structure depends only weakly on the Coriolis force so that the latitude and wind direction are not important except in the limiting equatorial case.

3.5 Modeling the Stable Boundary Layer

Although a successful second-order model for the stable PBL has yet
to be published, Businger and Arya (1974) have recently provided a K model
incorporating a stability parameter that appears to give realistic stress
and wind profiles for positive values of μ_* (see Section 5.5).

Using the non-dimensional parameters introduced in Section 2.3, the
non-dimensional stresses can be written

$$T_x = K_* \frac{\partial J_o}{\partial \xi}$$

$$T_y = K_* \frac{\partial G_o}{\partial \xi}$$

$$K_* = K_m f / u_*^2$$

where K_m is the dimensional eddy viscosity. The dimensionless wind shear,
ϕ_m, can be written

$$\phi_m = \frac{kz}{u_*} \frac{\partial U}{\partial z} = \frac{k\xi}{K_*} T_x \qquad (3.5.1)$$

Businger and Arya point out that surface layer similarity predictions, con-
firmed by experiment, imply

$$\phi_m = 1 + \beta z/L \qquad (3.5.2)$$

where β is a constant. They also note that for small ξ, the first of
Equations (2.3.5) can be written

$$T_x = 1 - \left|\frac{V_R}{u_*}\right|\xi + \ldots \simeq \exp\{-\left|\frac{V_R}{u_*}\right|\xi\} \qquad (3.5.3)$$

which exhibits a fairly realistic curvature of the stress profile. They
reason that if the log-linear profile, (3.5.2), extends to some distance
beyond the surface layer as observations indicate, then at least in this
region, (3.5.3) and (3.5.2) can be substituted into (3.5.1) to yield

$$K_* = k\xi \exp\{-|\frac{V_R}{u_*}|\xi\}/(1+\beta\xi\mu_*),$$

$$\mu_* = u_*/fL.$$

They then use this K_* distribution and the derivatives of Equations (2.3.5) to solve iteratively for the mean profiles of velocity and stress.

The results of this model for the limiting neutral case ($\mu_* = 0$) agree well with the neutral model from Wyngaard et al. (1973), lending credence to this method. The effect of increasing stability, as predicted by the model, is to lower geostrophic drag, to increase the angle between surface stress and geostrophic wind, to increase stress profile curvature, and to decrease the penetration distance of frictional effects.

4 DESCRIPTION OF THE EXPERIMENT

4.1 Site

The site of the experiment discussed in this dissertation was the 1972 AIDJEX Pilot Study main camp, first established on February 25, 1972, at approximately 75°N, 148°W, roughly 400 km NNE of Barrow, Alaska. A good summary of the 1972 camp configuration with preliminary reports from most of the scientific projects including ours is given in AIDJEX Bulletin, 14, (July, 1972). More extensive reports on various projects can be found in subsequent issues of the AIDJEX Bulletin.

Our group, consisting of nine people under the leadership of Associate Professor J. Dungan Smith, occupied five buildings including two instrument huts, two living huts and a diving hut, all situated in the northwest corner of the main camp.

We had originally planned to deploy 3 or 4 separate frames, each carrying current-meter triplets at several different levels, across a large pressure ridge with a fairly uniform cross-section along its axis in order to gauge the effect of form drag over such a feature. It turned out, however, that the necessity of the camp being near a smooth runway for large aircraft governed its placement, and we were constrained to choose the only region of obvious surface relief within range of the camp's generators. This proved to be a small multi-year ridge with a maximum keel depth of only 5.3 m, situated at the eastern edge of the frozen lead that served as the camp's runway.

Figure (4-1) from Welch et al. (1973) shows the configuration in which the four frames were actually deployed. Contour lines indicate the relief

of the underside of the ice, obtained by divers taking pressure measurements at the bottom ice surface along a carefully laid out grid system. Contour intervals are .5 m. As the map clearly shows, the ridge trends northeast-southwest for some distance, but slopes abruptly into the smooth ice of the runway which lies roughly northwest-southeast just off the bottom of the map. The diving hole marks the eastern edge of the ridge, both above the surface and below.

Frames 1 and 2 were hung approximately 2 m apart through a large hole in the ice beneath the instrument hut in a region of fairly uniform topography. Frame 1 extended 26 m below the ice and Frame 2 continued from that level to 54 m. Taken together they were considered to measure one profile with triplets at eleven levels and are usually hereafter referred to jointly as the "main frame". Frame 3 was located beneath the apex of the ridge and Frame 4 was situated beyond the ridge at the edge of the runway. Frames 3 and 4, called the "outer" frames, each had triplets at six levels down to 26 m from the lower ice surface. The outer frames were assembled at the diving hole and positioned by the divers using an ingenious beer-keg floatation device. They were suspended from hangers frozen into holes drilled from above so that the orientation was accurately known.

Figure (4-2) is a section drawn in the plane of the current-meter masts showing the relative relief and indicating the levels at which triplets were mounted on the frames. The wavy line indicates approximately the bottom of the mixed layer through which density was nearly uniform. The arrows attached to the North pointer indicates the directions of typical currents measured relative to the ice during the period April 10 through April 13. The surface current was measured at 2 m on the main frame and the deep current at 32 m, near the base of the mixed layer.

4.2 General Description of the Measurements

Although current measurements were begun on Mar. 29 during a period of comparatively high winds, an unforeseen problem in the data collection system resulted in our logging data of questionable value during the first storm. After a couple of days of intensive effort, the problem was found and corrected, but not before the winds had subsided and relative currents had fallen off to below instrument threshold. Thereafter, except for minor alterations to individual channels and occasional power losses, the data logging system performed very well. Considering that the system had to be assembled hurriedly because of the short time imposed by Pilot Study funding and hardware delivery delays, the fact that it worked so well in the field without thorough prior testing is a credit to everyone involved with its development.

After the storm during the last few days in March we were becalmed until the winds picked up again early on Apr. 10. The period from the morning of Apr. 10 through the morning of Apr. 14 was characterized by quite steady westward drift resulting in substantial currents relative to the ice. After Apr. 14, the currents dropped off in the upper 35 m, although in the pycnocline flow persisted for a couple more days. On Apr. 16, the last of the current-meter frames was dismantled and the current measuring phase of the experiment was concluded. The measurements referred to in this work were all taken during the period Apr. 10 through Apr. 15.

The direction of the surface current shown in Figure (4-1) indicates that the relative flow for nearly the whole measurement period was more parallel to the ridge than across it. Thus, in terms of the original

objectives of the experiment, it was as if Nature were adding irony to
insult by directing the flow along, instead of across, a ridge that was
none too large to begin with. Obviously, under these circumstances the
effect of the ridge was difficult to ascertain. Adding to the uncertainty
about topographic effects was the fact that the flow came from a very smooth
region of first-year ice (the runway) onto the rougher multi-year floe on
which the camp was located.

The unfavorable drift direction also resulted in another problem at
least as serious, if not so obvious, as the one mentioned above. Frames 1
and 2 were suspended in an ice-free hole from inside the instrument hut
allowing us to adjust or "tune" the frame orientation so that all three
meters of the orthogonal triplets (described in the next section) would
experience strong enough current components in each direction to keep them
turning, i.e., above threshold velocity. Unfortunately, the outer frames
were frozen into a fixed orientation such that under the prevailing drift
one meter of each triplet did not turn. During the one period when a rea-
sonably strong and steady current from another direction did exist, a
different component in each triplet was below threshold. In retrospect, it
would have been possible to rig the outer frames with swivel-like devices
so that the divers could have adjusted them. But as it happened, Reynolds
stresses were measured at the main frame location only, since meaningful
momentum flux measurements required all three components, given the triplet
configuration. Mean currents at the outer frames were determined with
reasonable accuracy from two components, so that considerable information
was gained from them, in spite of the threshold problem.

4.3 Current Meters and Data Collection

The current meters used during the 1972 AIDJEX Pilot Study had to be small enough and sensitive enough to measure very slow currents and had to respond rapidly enough to current fluctuations to adequately measure Reynolds stresses. They also had to be durable and inexpensive enough to deploy in large numbers in the field. A small, partially ducted, mechanical current meter developed for an ongoing series of turbulence experiments directed by Dr. Smith met these requirements. A brief description of the meters is presented here, but for a more complete specification including the manner in which they were mounted to frames see Smtih (1973).

The meter consists of a near-neutrally buoyant rotor 1.7 cm long by 3.5 cm in diameter encased in a truncated duct 1.3 cm long by 4.1 cm in diameter. The shaft of the rotor is attached to a heavy wire frame via water-lubricated jeweled bearings. The duct is supported on a sealed stainless-steel rod 1 cm in diameter (see Figure 4-3).

Triplets were made by mounting the current meters in a rigid mounting block with the configuration indicated by the following sketch looking down on the triplet:
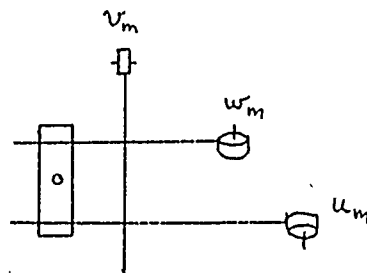
This resulted in an othogonal measurement frame of reference idealized as the following:
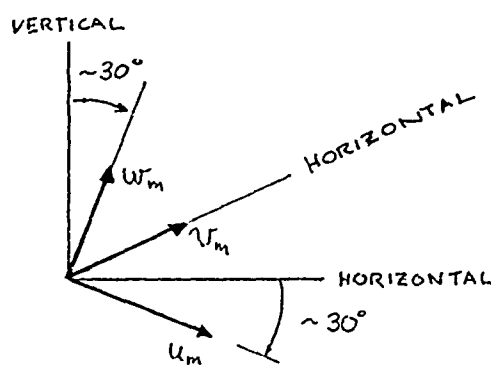
The so-called w_m component was not vertical for the obvious reason that vertical currents would rarely exceed the threshold level of the current meter. The requirement of othogonality then forced the u_m component to be inclined downward at an angle chosen arbitrarily to be about 30 degrees from the horizontal. In actual practice, the angle of dip was not assumed to be 30 degrees since the masts were not exactly plumb, but rather was calculated assuming the flow to be horizontal over a suitable averaging period (see Appendix B).

The current-meter rotor has four impellers. On the end of each a mirror is mounted that reflects light from a small lamp in the center of the supporting rod back to two photo-diodes embedded on each side of the lamp. As the rotor revolves, each photo-diode is activated in turn as the light beam is reflected from a passing blade. Electronics housed in the mounting tube discriminate between the pulses from each diode by assigning them opposite polarity and combine the two pulses into a bipolar pulse (dipulse) output. The direction in which the rotor is turning is thus indicated by the polarity of the leading half of the dipulse.

The pulse train generated by each current meter is transmitted through a specially designed cable to the surface where it can either be recorded

in analog form on an FM (frequency modulating) tape recorder or be fed through a device that converts it to digital information to be processed and recorded by a small digital computer. The latter approach was used for the first time during the 1972 AIDJEX project and made it possible to log data from 75 current meters simultaneously.

The computer used for data acquisition was a Data General Nova 1200 with approximately 8,000 (8K) sixteen-bit words of core memory and a 1300 nanosecond basic cycle time. Options and peripherals at the time of the field project included a hardware multiply/divide unit, a real-time clock, a special current-meter interface, two Ampex magnetic tape drives and controls, and a teletype with paper-tape reader and punch. Since that time the system has expended to include another 8K of core, a hardware floating-point processor, a high-speed paper-tape reader and punch, a CRT display with plotting capability and hard copy, an analog-to-digital interface, and a digital interface. The present system is thus quite versatile and was used to process all the current-meter data from the 1972 project. Programming, done in the Nova Assembly language, has been simplified by a specially designed Tape Operating System. The software (programming) for data collection and processing was desigr.d by the author.

The special current-meter interface (CMIF) consists of a very stable, 20-KHz crystal oscillator and counter, a master memory-address buffer, and a buffer for each current-meter channel. When a dipulse is sensed on a given channel the clock counter is read, the polarity determined and the 16-bit word is sent via fast data channel to a specific location in the computer's memory. The CMIF also generates computer interrupts at a rate determined by the program (12.8, 25.6, 51.2 or 102.4 msec) that direct the

computer software to scan for information sent since the last interrupt and to process and store it.

The CMIF can handle up to 128 channels and is designed so that even if all channels have simultaneous dipulses, the processing delay is less than .05 msec ensuring accuracy to within 1% for currents up to 100 cm-sec^{-1} (Smith, 1972b).

The function of the data-collection software is to convert the information sent from the CMIF, consisting of a polarity indicator and the count of the continuously cycling clock, into meaningful periods between successive pulses and to store these data on magnetic tape for later processing. When the program senses an interrupt from the CMIF it changes the master memory address and restarts the CMIF so that it can be filling a new input buffer (i.e., a table in the computer's memory to which the CMIF transfers data) while the previous data are processed. For each channel the program determines if a pulse has occurred since the last interrupt; if it has, the significant part of the clock counter is added to a temporary accumulation of counts since the last pulse, the resulting period is stored in an output buffer, and a new temporary accumulation is started. If a pulse has not occurred, the total number of counts between interrupts is added to the temporary accumulation, and the period from the previous cycle is stored in the current output buffer. After eight such interrupts the output buffer is written on magnetic tape. The system will handle currents up to about 160 cm-sec^{-1} but can also be made to record efficiently (i.e., with little redundancy) at currents as low as 15 cm-sec^{-1} by adjustments to the clock rate.

The resulting data stored on magnetic tape are integers representing

periods between pulses in units of .05 msec. Conversion to velocities

comes later during further processing. However, the data collection program

has the capability of taking particular samples from each channel, perform-

ing the conversions and outputting the results to the teletype so that the

system can be monitored while data collection is in progress.

Figure (4-4) is a schematic diagram showing the steps described above.

4.4 Data Processing

Figure (4-5) shows schematically the flow of data from the original recordings to final output form. The circles symbolize information stored on magnetic tape while boxes imply tabular or graphical material. The huge amount of data -- filling well over a hundred 2400-foot reels of magnetic tape -- made it necessary to break the processing into several intermediate steps.

Upon first looking at the recorded data we discovered that having mirrors on each of the four rotor blades presented difficulties: the reflective properties of the mirrors were enough different to cause appreciable departure from the assumed 90 degree angle between impellers. Thus, in the period of one complete revolution in a steady flow, four distinct velocities appeared corresponding to each quadrant of the rotor. The variations were at least of the same order as the real turbulent fluctuations, so that there was no choice but to sacrifice some frequency resolution for an accurate period measurement over one complete revolution. This was accomplished by treating every fourth pulse as significant and using the other three to determine the period, between each significant event. The end result was the same as if only one impeller were reflectorized.

Various other problems were discovered with the original data. Some, such as wrong signs and very short periods caused by spikes in the pulse train, were anticipated and easily corrected. Another problem observed on some channels was the failure of one or more impellers to trigger dipulses. This phenomenon interacted with processing out the four-mirror problem to create a curious wave-like feature in the current record; the problem was easily corrected once its source was found.

A particularly vexing problem occurred on a channel that was part of the triplet at 4 m on the main frame. Apparently, an extraneous signal would intermittently trigger the system with pulses of the wrong sign. Although the ensuing short period was thrown out by logic in the editing program, the sign of the following period was changed and this was not detected. This resulted in anomalously high, but believable, Reynolds stresses at intermittent intervals 4 m below the ice and these were referred to in at least one preliminary abstract (McPhee and Smith, 1972). It was taken as a cautionary lesson in the pitfalls awaiting those who handle large amounts of data.

Period-to-velocity conversion is described in Appendix A. The data from original tapes were corrected for the four-mirror problem, edited and converted to velocities, then output on new tapes. These tapes, containing velocity samples accurate to 9 binary places for each of 72 current meters sampled approximately every .2 sec, then became the basic data set for the remainder of the processing, which will be described in greater detail in later sections.
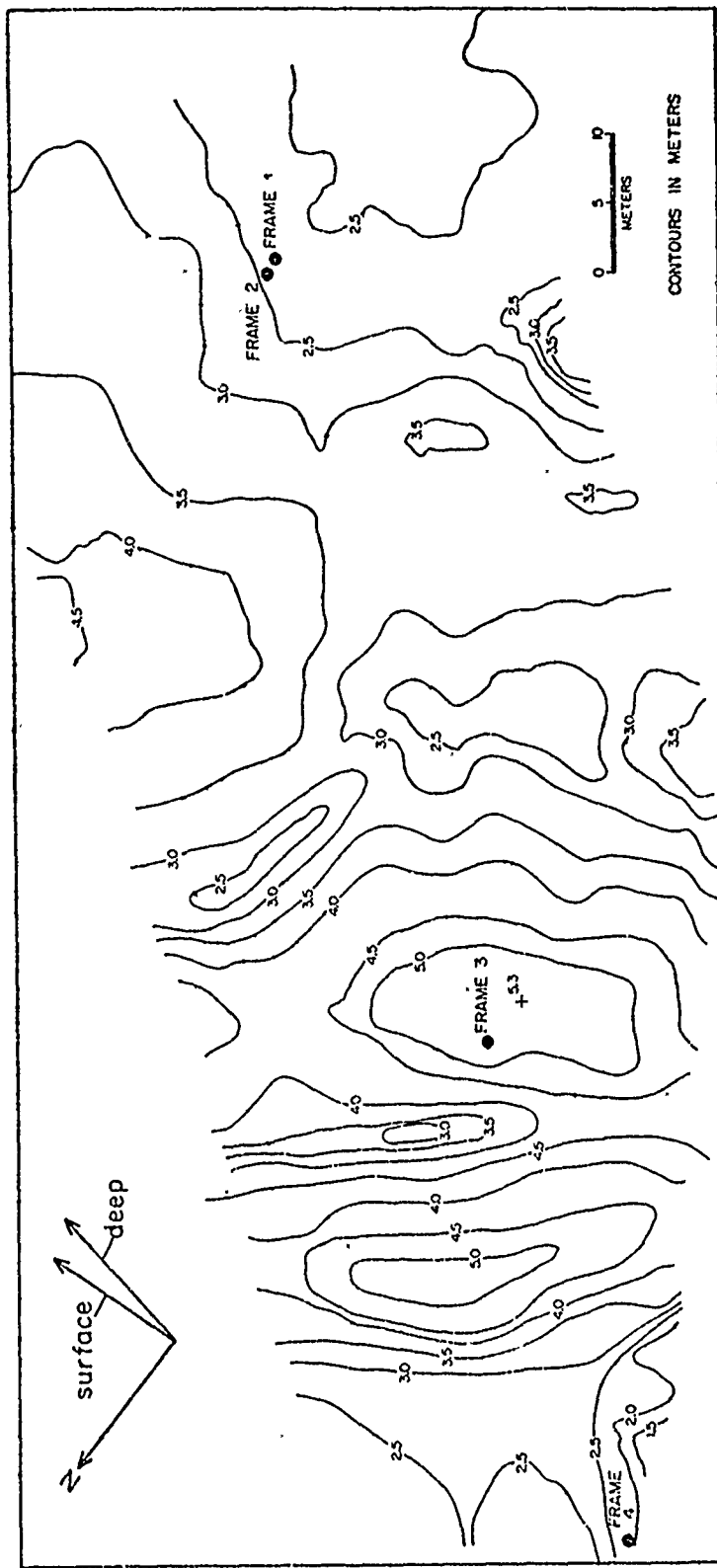
Fig. 4-1 Under-ice topographic map in vicinity of current meter frames
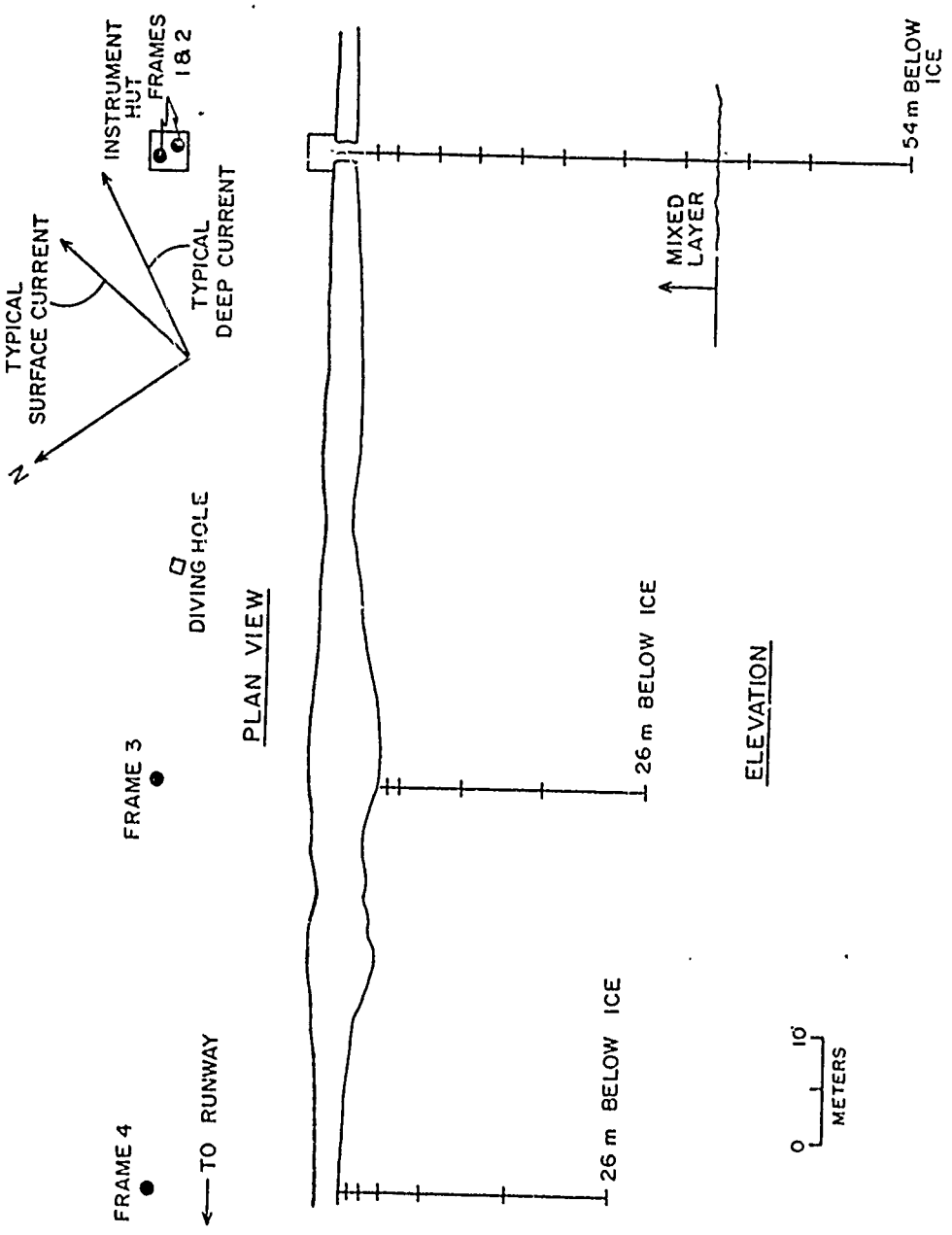
Fig. 4-2 Section drawn through plane of current-meter frames
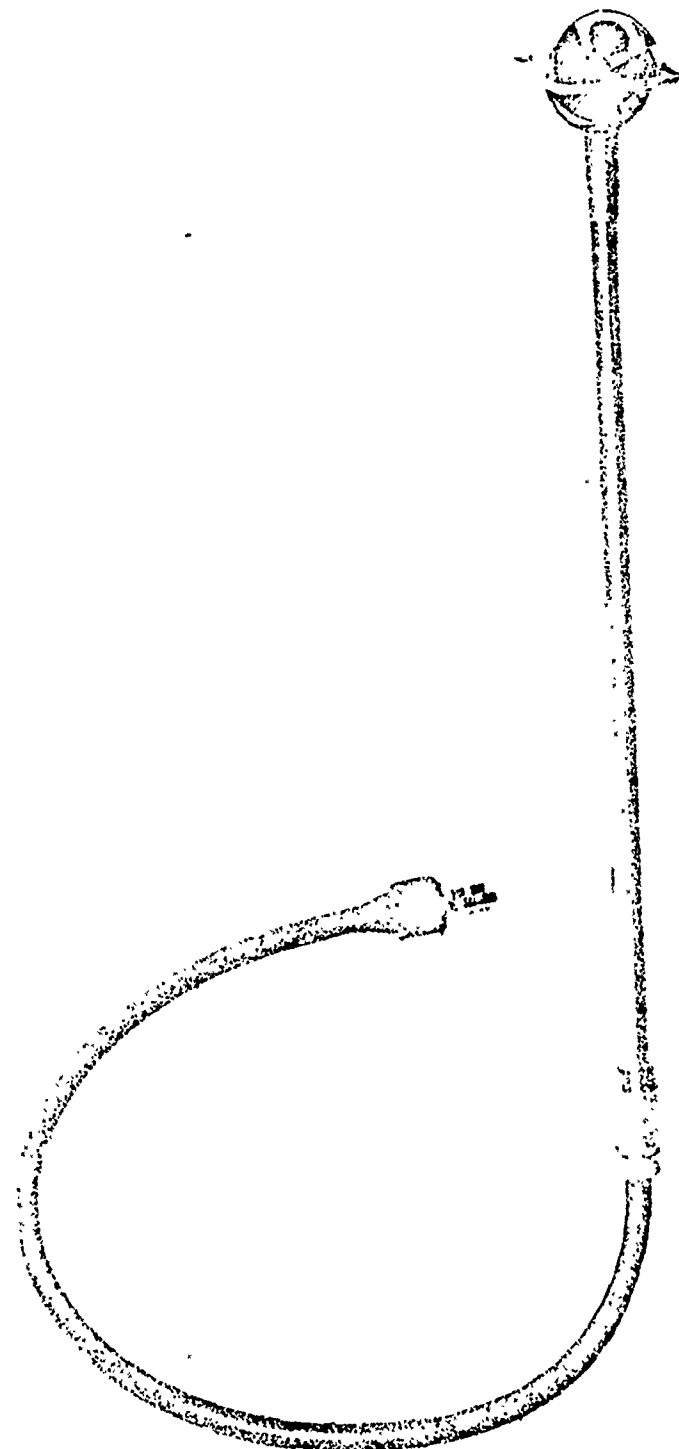
Fig. 4-3   Turbulent Boundary Layer Current Meter
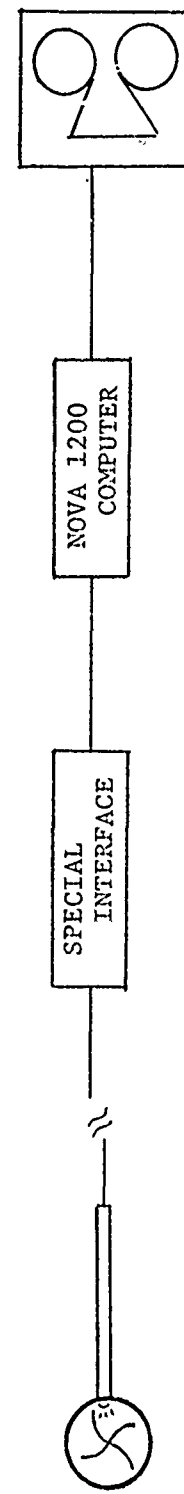
CURRENT METER ELECTRONICS:
send out bipolar pulse
each time mirror passes
light source

SPECIAL
INTERFACE

INTERFACE:
(1) determines sign
from pulse polarity
(2) reads a 20 kHz
counter every time
it receives pulse
(3) combines infor-
mation into 16-bit
binary word and serds
it to a computer mem-
ory location corre-
sponding to channel
number

NOVA 1200
COMPUTER

COMPUTER:
determines time
elapsed since last
pulse by comparing
counts and writes
the period between
pulses on magnetic
tape

TAPE UNITS:
digital data
stored on
magnetic tape
for later
processing

Fig. 4-4 Schematic of the current meter data collection system

ORIGINAL DATA TAPES
Periods between pulses
as binary integers

VELOCITY TAPES
Edited and corrected for
unequal blade angle,
9 binary place fixed-point,
double-precision numbers

Statistics and
spectra of high-
frequency time
series

Plots of
long time
series, spec-
tra of long
series

ONE-MINUTE AVERAGE
TAPES
Velocity and vel-
ocity products
accumulated in
one-minute groups

Results of 20-
minute mean
flow and Rey-
nolds stress
calculations

Composites of
20-minute ave-
rages non-dim-
ensionalized
and plotted

Fig. 4-5 Flow of data from original to final output form

5 DENSITY STRUCTURE IN THE BOUNDARY LAYER

5.1 Introduction

To this point in our discussion of the planetary boundary layer we have assumed that the layer is neutrally bouyant, i.e., density differences do not play a role in the dynamics of the layer. That density is a function of depth and that acting through gravity this dependence can potentially have an appreciable effect on the turbulent structure of the boundary layer is the subject of this chapter.

5.2 Measurements

Density measurements were made during the project with a Guildline Conductivity-Temperature-Depth (CTD) sensor from a location about 10 m west of the main-frame hut. Profiles sampled at approximately one-meter intervals down to 65 m were made at periods ranging from a few minutes to several hours. Deep casts were made daily to a depth of about 1000 m (Morse and Smith, 1972).

Density is almost exclusively a function of salinity in the Arctic during the winter and spring months, since the water column is very near its freezing point to considerable depth. A typical deep profile of density vs. depth is shown in Figure (5-1). Here density is expressed in σ_t units where $\sigma_t = (\rho-1) \times 1000$, and ρ has units $gm\text{-}cm^{-3}$.

A few features are immediately obvious. A well-mixed layer extends some 30-35 m. Beneath this a strong pycnocline extends to nearly 300 m, below which the water column is nearly neutral. Thus, dynamically, the upper part of the ocean is very stable except for a thin layer near the surface.

Since our current measurements were restricted to the upper 54 m of the ocean we were interested mainly in the density structure of the mixed layer. Changes in the structure of the upper pycnocline will be discussed in greater detail later in the treatment of transient currents there.

5.3 The Effect of Buoyancy on Turbulence

The water column can be classified as stable, unstable or neutral according to whether its density gradient is negative (i.e., density increasing with increasing depth), positive or zero. It is clear that in a stable environment work is done against gravity at the expense of turbulent energy while in the unstable case buoyant accelerations enhance turbulence.

A quantitative parameter for describing the interaction between shear turbulence and buoyancy can be derived with the aid of the turbulent kinetic energy budget, Equation (2.2.7). Under the constraints of steady-state, horizontally homogeneous mean flow in the x-direction, it becomes

$$-\overline{uw}\,\frac{\partial U}{\partial z} - \frac{g}{\rho_0}\,\overline{\rho' w} = \frac{1}{2}\,\frac{\partial}{\partial z}\,(\overline{u_i u_i w} + \overline{wp}) + \nu\,\overline{\frac{\partial u_i}{\partial x_j}\,\frac{\partial u_i}{\partial x_j}} \qquad (5.3.1)$$

The first term on the left of Equation (5.3.1) represents the production of turbulent kinetic energy by mean flow shear. It appears with opposite sign in the equation of kinetic energy for the mean flow and thus represents a sink for mean-flow kinetic energy (Tennekes and Lumley, 1972).

The second term is the buoyant energy term. It can be either a source or sink depending on the sign of $\overline{\rho' w}$, the density flux. For instance, $\overline{\rho' w}$ negative implies a downward transport of more dense material and thus would add to the turbulent energy at the expense of potential energy of the fluid.

The terms on the right represent flux divergence- pressure transport and viscous dissipation respectively. Viscous dissipation is the sink in which turbulent kinetic energy is converted to internal energy of the fluid.

The flux Richardson number is defined as minus the ratio of the buoyant energy term to the shear production term.

$$R_f = -\frac{g}{\rho_0} \overline{w\rho'} \Big/ \overline{uw} \frac{\partial U}{\partial z}$$

A critical flux Richardson number above which turbulence cannot be maintained against the restoring force of gravity has been experimentally determined to be about .2 to .25.

A second Richardson number, the gradient Richardson number, is defined as

$$Ri = -\frac{g}{\rho_0} \frac{\partial \rho_0}{\partial z} \Big/ \left(\frac{\partial U}{\partial z}\right)^2$$

The relationship between R_f and Ri can be demonstrated by relating the turbulent fluxes, $\overline{w\rho'}$ and $\overline{uw}$, to their respective mean gradients via eddy coefficients of diffusion and viscosity.

$$\overline{w\rho} = -K_\rho \frac{\partial \overline{\rho}}{\partial z} , \qquad \overline{uw} = -K \frac{\partial \overline{U}}{\partial z}$$

Thus

$$R_f = \frac{K_\rho}{K} Ri$$

If K_ρ and K are about the same, as for example, they are in the atmosphere where potential temperature is the dynamically important property, the two Richardson numbers are sometimes considered interchangeable.

In the Artic Ocean, where density is primarily a function of salinity, the relationship is not so clear. Direct salinity flux measurements are quite difficult and thus the eddy exchange coefficient, K_s, is usually inferred from dynamical considerations and estimates of its value vary by an order of magnitude. Taylor (see Neumann and Pierson, 1966, p. 400) suggests that the ratio K_s/K is from 1/5 to 1/50. Thus a gradient Richardson number as large as 10 might still permit turbulence.

It should be emphasized that the flux Richardson number, since its

definition stems directly from the turbulent energy budget, is the more

universal in the sense that a turbulent flow will behave in a certain way

given a specific Richardson number.

5.4 Measured Average Density Structure

Figure (5-2) shows a typical cast made to approximately 60 m with the CTD described above. Figures (5-3) and (5-4) show averages of casts made on Apr. 12 and Apr. 13, made by classifying samples by depth and averaging over about a dozen different casts on each date. The bars represent the sample standard deviation measured each way from the mean value at each depth. Figure (5-5) shows the different averages for four days during the storm drawn on one graph.

The source of the large variance of measurements in the top 10 to 15 m remains a mystery. If it were due to instrumental sampling error, we would expect it to carry throughout the cast. However, the variance toward the bottom of the mixed layer becomes quite small. Also, measurements in other areas with the same probe have never shown a similar phenomenon (J. Smith, personal communication).

If water of different salinity were being carried by the mean (relative) flow as a contaminant (either active or passive), we might expect such behavior since a plot of velocity variance with depth shows many of the same features: i.e., a great deal of variance near the surface falling off to a minimum at the base of the mixed layer, then picking up again in the pycnocline. If turbulent transport were the mechanism, however, the density variance would be expected to fall off as the turbulent intensity decreased. Casts taken on days when there was virtually no water movement relative to the ice showed as much or more variation in the upper layers. This reasoning seems to argue against the idea that the probe was advected through plumes of more dense water resulting from active lead convection.

Another suggestion that has been offered is that draining brine pockets in the ice could be responsible for the large variance without the necessity of mean velocity shear (an analog would be thermal plumes on a hot day). But if this were the case, near the surface we would expect only positive excursions from the salinity of the rest of the water column in the mixed layer. Instead, excursions on the fresh side are as common as the more saline ones, as Figure (5-2) demonstrates.

The fact that the phenomenon was observed on upward casts seems to rule out flushing problems.

This aspect of the measurements was unsatisfying, since we could not see a clear explanation, either natural or instrumental, for the large varia-tion from cast to cast. It was found that averaging over several casts provided a fairly smooth profile and this was the approach used. Straight lines were fit to the data in the top 35 m of the water column (excluding the uppermost meter, which was in the instrument hole) in a least-squares sense. For the average profile of Apr. 12 (Figure 5-3), the slope of this line was $\frac{\partial \bar{\rho}}{\partial z} = -8.8 \times 10^{-9}$ gm-cm^{-4}; for Apr. 13 (Figure 5-4), $\frac{\partial \bar{\rho}}{\partial z} = -2.2 \times 10^{-9}$ gm-cm^{-4}.

5.5 The Obukhov Length Scale

In atmospheric studies, conditions are usually determined in the sur-
face layer and extrapolated to the outer layer. For instance, it is not
uncommon to classify a boundary layer as unstable because of an upward heat
flux at the surface while the outer layer is characterized by a neutral or
even slightly stable mean potential-temperature profile up to the inversion
(J. Businger, class notes). The dynamical properties of the surface layer
seem to govern the properties of the whole boundary layer-- not too surpris-
ing since most of the dynamical action takes place there.

Straight lines fit to the average profiles for Apr. 12 and Apr. 13 in
a least-squares sense show slightly stable slopes. The point of the dis-
cussion above is that this does not necessarily preclude the possibility
of an unstable boundary layer; in fact, a good analog exists between the
upward heat flux in the atmosphere due to solar heating of the surface and
the downward salt flux due to freezing at the ice-sea interface.

In order to investigate quantitatively the effect of freezing it is
convenient to introduce the Obukhov length scale, L. Since (5.3.1) is an
equation for the time rate of change of energy divided by density, it can
be non-dimensionalized by multiplying each term by an appropriate time scale
divided by the square of a velocity scale. For the surface layer these
scales are ℓ/u_* and u_* respectively. If $\ell = kz$, the non-dimensional form
of (5.3.1) is

$$\frac{-kz\ \overline{uw}}{u_*^3}\frac{\partial U}{\partial z} - \frac{g}{\rho_0}\frac{k}{u_*^3}\overline{\rho'w}\ z\ =\ \phi_D + \phi_\varepsilon \tag{5.5.1}$$

where ϕ_D is the non-dimensional flux divergence-pressure transport term and
ϕ_ε is the dimensionless dissipation.

From the second term in (5.5.1) a length scale may be defined by

$$L = \rho_o u_*^3 / g \, k \, \overline{\rho'w} \qquad (5.5.2)$$

In the <u>surface layer</u> $\overline{uw} = u_*^2$ and we can define the dimensionless wind shear as

$$\phi_m = \frac{-kz}{u_*} \frac{\partial U}{\partial z}$$

Equation (5.5.1) then becomes

$$\phi_m - \frac{z}{L} = \phi_D + \phi_c$$

The significance of the length scale L is now clear. L varies inversely as the density flux and is negative if the flow is unstable and positive if stable. Also, at least for small departures from neutrality (where $\phi_m = 1$), we see that as $|z|$ approaches $|L|$, the contribution from buoyant forces to the turbulent energy becomes as important as the shear production.

A great deal of micrometeorological evidence supports the Monin-Obukhov similarity hypothesis: i.e., that when velocities are scaled with u_* and lengths with L, there are universal descriptions for the dimensionless wind shear and lapse rate in the surface layer (Businger, <u>et al</u>., 1971).

By again suggesting that the surface layer scales are appropriate to the outer layer because they govern most of the dynamics, we can form a dimensionless stability parameter for the outer layer by dividing its characteristic length by the Obukhov length (which is determined in the surface layer). Thus we have $\mu_* = -z_i/L$ if z_i is the depth of the mixed layer (inversion) in the unstable case or $\mu_* = u_*/fL$ if the layer is neutral or stable.

We can make a rough estimate of the freezing rate required at the ice surface to maintain $\mu_* = -1.0$, corresponding to a slightly unstable layer

(for comparison, the value of the dimensionless height, z/L, about halfway through the surface layer would be $-1/100$).

If the salinity of sea-water is taken as 30 parts per thousand and it is supposed that it freezes fresh with a density of $.9$ $gm-cm^{-3}$, then a growth rate of 1 $cm-sec^{-1}$ is associated with the release of $.027$ gm of salt per cm^2. Thus $r = 36s$ where $\underline{r}$ is the growth rate in $cm-sec^{-1}$ and $\underline{s}$ is the mass flux in $gm-sec^{-1}-cm^{-2}$. For a steady state the turbulent density flux, $\overline{w\rho'}$, must equal the mass flux at the surface.

Using typical values for the observed boundary layer-- $u_* = 1$ $cm-sec^{-1}$, $z_i = L = -3.5 \times 10^3$ cm, $k = .35$ -- we can solve Equation (5.5.2) to get $\overline{\rho'w} = -8.3 \times 10^{-7}$ in cgs units. This requires a growth rate of 3.2×10^{-5} $cm-sec^{-1}$ or 2.8 cm per day. Divers observing ice growth around cables at the base of the ice estimated average growth rates on the order of $.1$ cm per day during the period of the experiment (Welch, et al., 1973), thus we can infer that under thick ice during the spring, the freezing mechanism is not strong enough to cause appreciable instability.

As mentioned earlier, if a least-squares straight line is fit to the average density profiles on Apr. 12 and 13, the lines have negative (stable) slopes with magnitudes 8.8×10^{-9} and 2.1×10^{-9} $gm-cm^{-4}$ respectively. If we assume that a constant slope persists to the surface we can estimate the mean density gradient required to maintain $\mu_* = +1.0$ by using an eddy diffusivity constant.

$$\frac{\partial \bar{\rho}}{\partial z} = -\frac{\overline{\rho w}}{K_s}$$

We estimate $K_s = K/5$ (to give a minimum $\partial \bar{\rho}/\partial z$) and use K, the eddy viscosity, as 70 cm^2-sec^{-1} (see Section 9.7). For $\mu_* = 1.0$, $\overline{\rho w} = 8.3 \times 10^{-7}$, we get $\partial \bar{\rho}/\partial z = -6 \times 10^{-8} gm-cm^{-4}$ which is still considerably steeper than the slopes observed.

5.6 Conclusions

The calculations carried out in the preceding section are not intended to give definitive values for the buoyancy parameters, but rather to provide some guidelines. Without measurements within the surface layer, it is questionable whether it is possible to categorize the stability of the boundary layer directly. The arguments of this chapter imply that gradient Richardson numbers are of little value in describing the turbulent structure of the outer layer. The rough calculations indicate that the layer is nearly neutral, possibly only slightly stable. As will be shown presently, the density structure inferred from the dynamical measurements will support this assessment.

Although calculations indicate that freezing cannot induce appreciable instability under thick ice, the situation under a fresh lead or polynya, where rapid freezing, evaporation and heat flux are occurring simultaneously, could be quite different. Since an unstable boundary layer is considerably more efficient at transferring stress, such regions of open water might be much more important to the overall stress balance than their relative area might indicate. Offsetting this effect to some degree is the fact that these areas are presumably much smoother than surrounding ice and thus do not have the form drag associated with older ice.
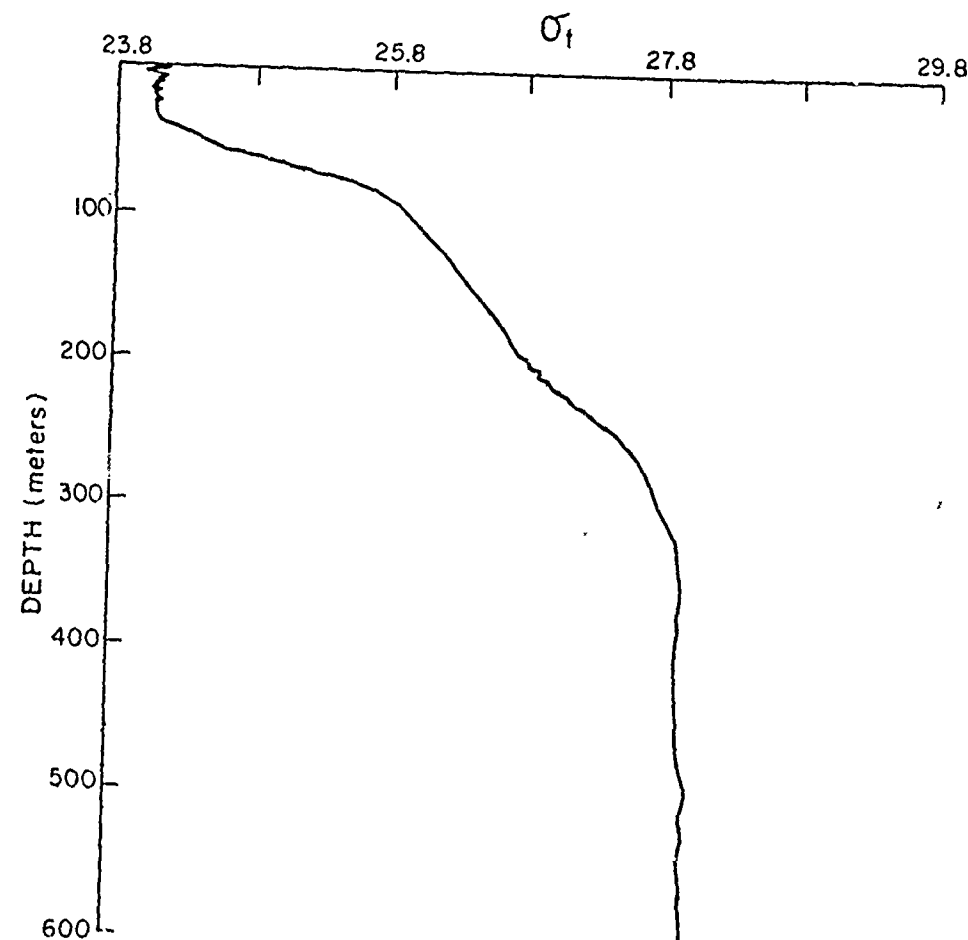
Fig. 5-1 Typical deep profile of σ_t vs. depth, March, 1972
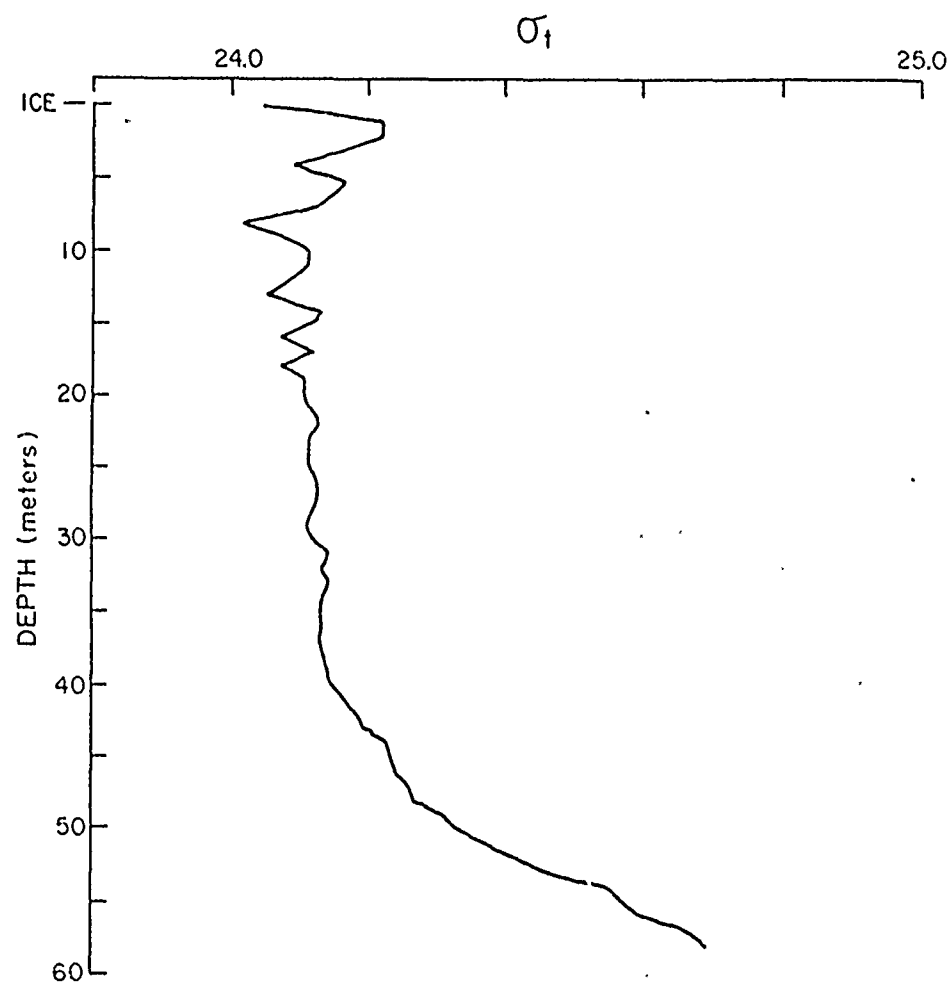
Fig. 5-2 Typical short cast showing large variation of density in upper 15 m
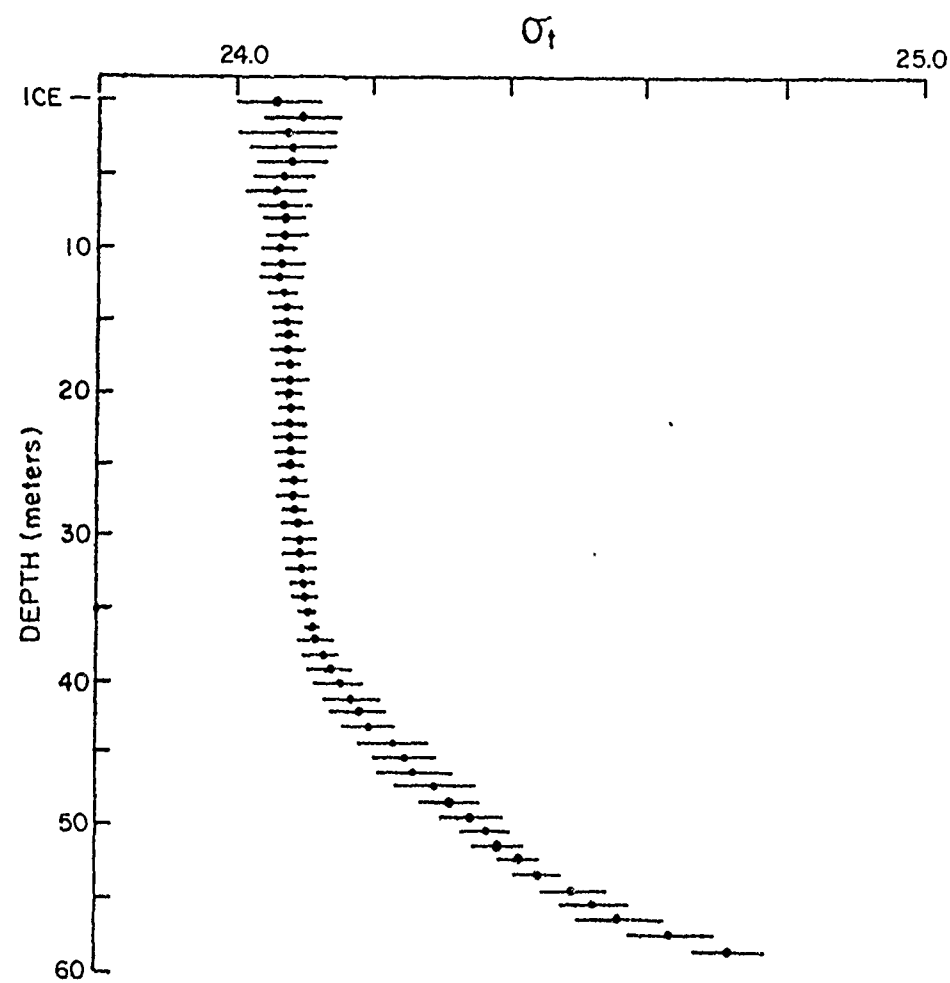
Fig. 5-3 Average σ_t profile from casts made on Apr. 12, 1972.
Bars represent
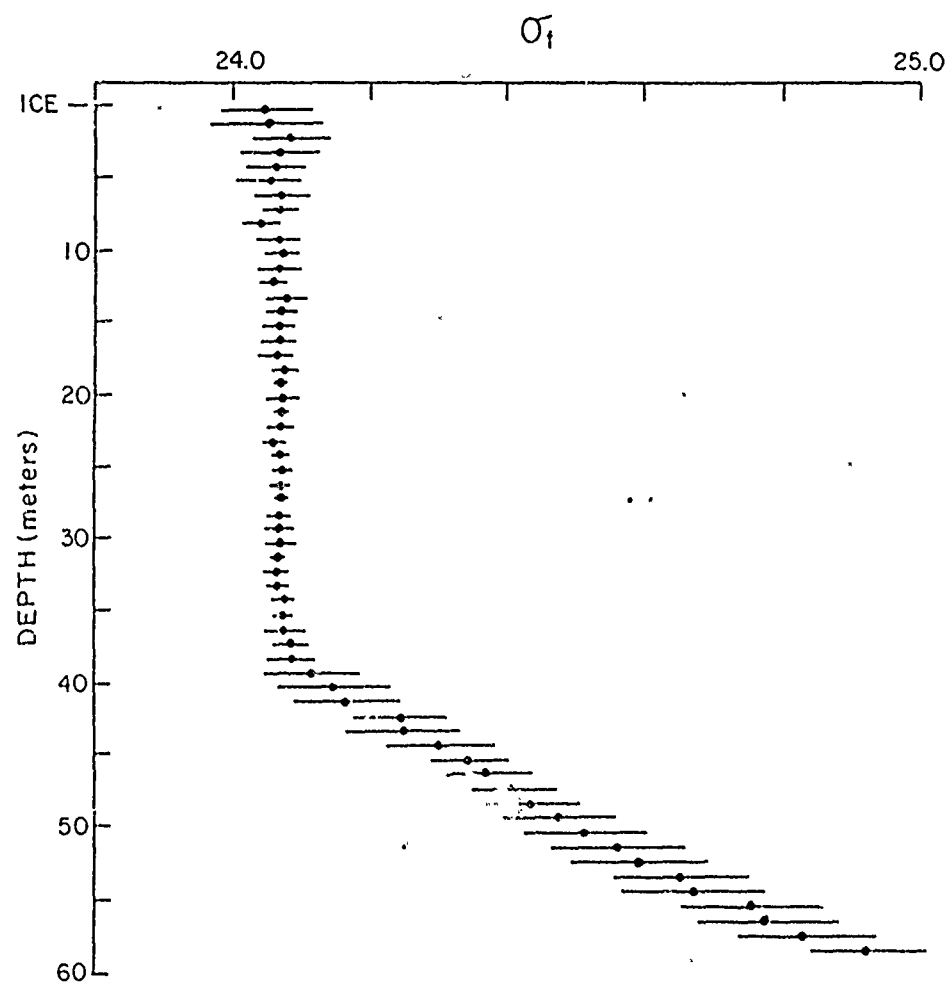
Fig. 5-4   Average σ_t profile from casts made on Apr. 13, 1972
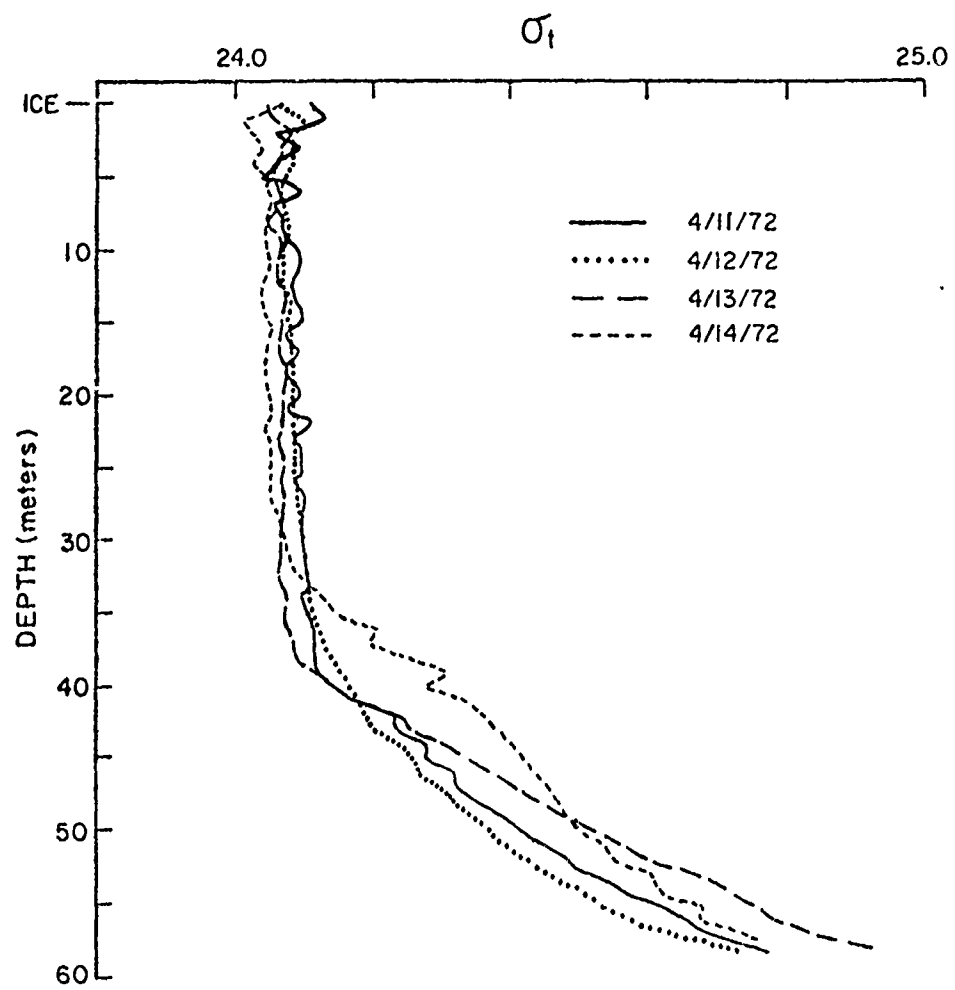
Fig. 5-5 Average daily density profiles for the period Apr 11
through Apr. 14.

6 RESULTS OF CURRENT MEASUREMENTS

6.1 Procedure

In light of the models discussed in Chapter 3, it was decided that the mean current and stress data would be presented in a manner making comparison between our measurements and the models as easy as possible. For this reason, a fixed (with respect to the earth) reference frame was rejected in favor of one attached to the ice. The x-axis was chosen to lie along the direction of surface stress which was approximated by using the mean current direction @ 2 m depth. The assumption of negligible turning in the upper 2 m appears to be borne out by the measurements. A right-handed coordinate system with the vertical axis positive upward was chosen to conform with the development of the equations in Chapter 2.

From $\overline{\tilde{u}_i \tilde{u}_j} = U_i U_j + \overline{u_i u_j}$, the Reynolds stresses are calculated by averaging the instantaneous component products over a specified time interval, then subtracting from each such average the product of the corresponding mean components, i.e.,

$$S_{ij} = \overline{(\tilde{u}_i - U_i)(\tilde{u}_j - U_j)}$$

$$= \frac{1}{N} \{ \sum_{k=1}^{N} \tilde{u}_i(k)\tilde{u}_j(k) - \sum_k \tilde{u}_i(k) \cdot \sum_k \tilde{u}_j(k) \}$$

where N is the number of samples in the averaging time.

In practice the average velocity vector and the Reynolds stress tensor were calculated in the experimental reference frame described in Section (4.3) over the specified averaging time, then rotated into final form with a rotation matrix determined from the mean components. Details of the rotation are given in Appendix B.

6.2 Averaging Intervals

In most theoretical treatments of turbulence, an ensemble average is assumed. If a flow is stationary in time, and certain other conditions are met (Tennekes and Lumley, 1972), the ensemble average is replaced by a time average, taken over T as $T \to \infty$ as discussed in Section (2.2). Clearly, this is an idealization that cannot be met in measurements of natural phenomena. Any success of a statistical treatment of turbulence data rests on the assumption of a spectral gap between what we consider turbulence (a difficult thing to define) and other phenomena such as long gravity waves, tides, synoptic-scale systems, or possibly in our case, independent ice motions.

Monin (1972, Chapter 1) has broken the entire spectrum of meteorological events into nine intervals and has shown evidence that between the first, which he calls micrometeorological oscillations, and the second, mesometeorological oscillations, there is a broad minimum in the area-preserving spectrum, $fS(f)$, of wind velocity. From Reynolds number similarity we expect the ocean to behave much the same. In order to measure turbulence, we would like to cut off our averaging interval somewhere in this minimum.

Besides this constraint, which is really just saying that we do not want deviations from the mean resulting from long-term trends to mask turbulent variances, we also were limited by the physical length of our data files, which were generally from 20 minutes to an hour long.

It cannot be clearly established from the data that a gap in the true energy spectrum exists. The problem is compounded by the fact that the

spectrum of, say, the downstream velocity component fluctuations is not easily related to the true turbulent spectrum at low wave numbers. This is discussed in greater detail in Chapter 9.

Table (6-1) shows the effects of different averaging times on the computed average momentum fluxes for a one-hour segment of data. To clarify further, if one minute is the averaging interval, then $-\overline{uw}$ is calculated for each minute of data and the average of 60 such calculations is shown. Similarly, if 20 minutes is the interval, the average value for three stress calculations is shown.

It is apparent that the major contribution to the stress comes from disturbances with time scales of 5 minutes or less. From tests like that shown in Table (6-1) and because it was convenient in terms of recorded file lengths, an averaging interval of 20 minutes was chosen for all Reynolds stress calculations.

6.3 Composite Averages

Although evidence such as Table (6-1) indicates the presence of a spectral gap, it does not imply that one realization of the turbulent flow field over a period longer than 5 minutes will provide a stable estimate of the actual stress. Atmospheric surface-layer measurements indicate that averaging times of at least an hour under unstable buoyancy conditions were required to estimate stress and that even then these data showed large scatter (Wyngaard, 1973).

According to Lumley and Panofsky (1964, p. 36) if an acceptable level of error is a, the averaging time required for a quantity to be estimated within a is given by the following formula:

$$T \approx 2 \frac{\overline{f'^2}}{\overline{f}^2} \; \mathcal{J} \; \frac{1}{a^2}$$

where $\overline{f'^2}$ is the ensemble variance of f about its mean, $\mathcal{J}$ is the integral time scale

$$\mathcal{J} = \int_0^\infty \rho(t)dt$$

and $\rho(t)$ is the autocorrelation (normalized autocovariance) of $f(t)$.

Clearly, we need some prior knowledge of f in order to estimate its averaging time. Figure (6-1) is an autocorrelation function calculated for the u-component of the 2-m triplet during the storm on Apr. 12. It is an average of several 28 minute samples. By approximating the area under the curve, we can estimate its integral time scale as somewhere in the neighborhood of 35 sec. Using twenty-minute averages, a typical value for $\overline{u'^2}/U^2$ is found to be .01. Thus to ensure 5% accuracy in estimating the true mean speed we must average for something like 280 sec or roughly

5 minutes. The averaging time varies as the inverse square of accuracy, so that to increase the accuracy by 5 times would require averaging for about two hours in a steady flow. If the results that hold for the atmosphere are any indication, we might expect considerable scatter in stress estimates for averaging periods up to an hour and even longer. This was confirmed by comparing individual twenty-minute averages.

It was felt that this problem would be minimized if a composite average were made of many twenty-minute averages representative of fairly steady conditions. To this end the current record was searched for such conditions and composite averages formed.

Figure (6-2) shows measured speeds and bearings for Apr. 12 at two levels: 32 m and 54 m. The dots represent smoothed data from the ABR system showing apparent bottom speed and bearing with respect to an observer on the ice. In the current traces, each solid segment represents a file of data; gaps between are times when data were not recorded.

The triplet at 54 m is situated well into the pycnocline and the current there was plotted to demonstrate the increase in activity compared to the 32 m level which is near the bottom of the mixed layer.

The time segment in Figure (6-2) labeled "Composite Average" starting at about 1230 denotes the time considered best for current measurements in terms of steadiness and maximum speed. Mean flow and stress data for each complete twenty-minute interval during this period were calculated and then all these calculations were averaged to arrive at composite profiles. This formed the basic data set for the project and is summarized in Table (6-2). It represents 15 twenty-minute averages or 5 hours of data. Similar calculations were carried out for 8 hours of composite data collected on Apr. 11 and are summarized in Table (6-3).

Depth (m)	1 minute		5 minutes		10 minutes		20 minutes	
	$-\overline{uw}$	$-\overline{vw}$	$-\overline{uw}$	$-\overline{vw}$	$-\overline{uw}$	$-\overline{vw}$	$-\overline{uw}$	$-\overline{vw}$
2	-.32	+.16	-.55	+.20	-.58	+.20	-.61	+.19
4	-.05	+.11	-.18	+.13	-.18	+.14	-.19	+.14
8	0	+.16	-.03	+.24	-.04	+.25	-.04	+.25
12	+.03	+.12	+.02	+.18	+.04	+.18	+.04	+.19
16	+.08	+.16	+.10	+.22	+.12	+.24	+.11	+.26
20	0	+.06	+.03	+.11	+.04	+.12	+.04	+.13
26	+.01	0	+.02	0	+.02	-.01	-.01	0
32	0	0	+.01	-.02	+.02	-.06	-.05	-.03

Table 6.1

Effect of different Reynolds stress averaging time for
the same one-hour segment of data
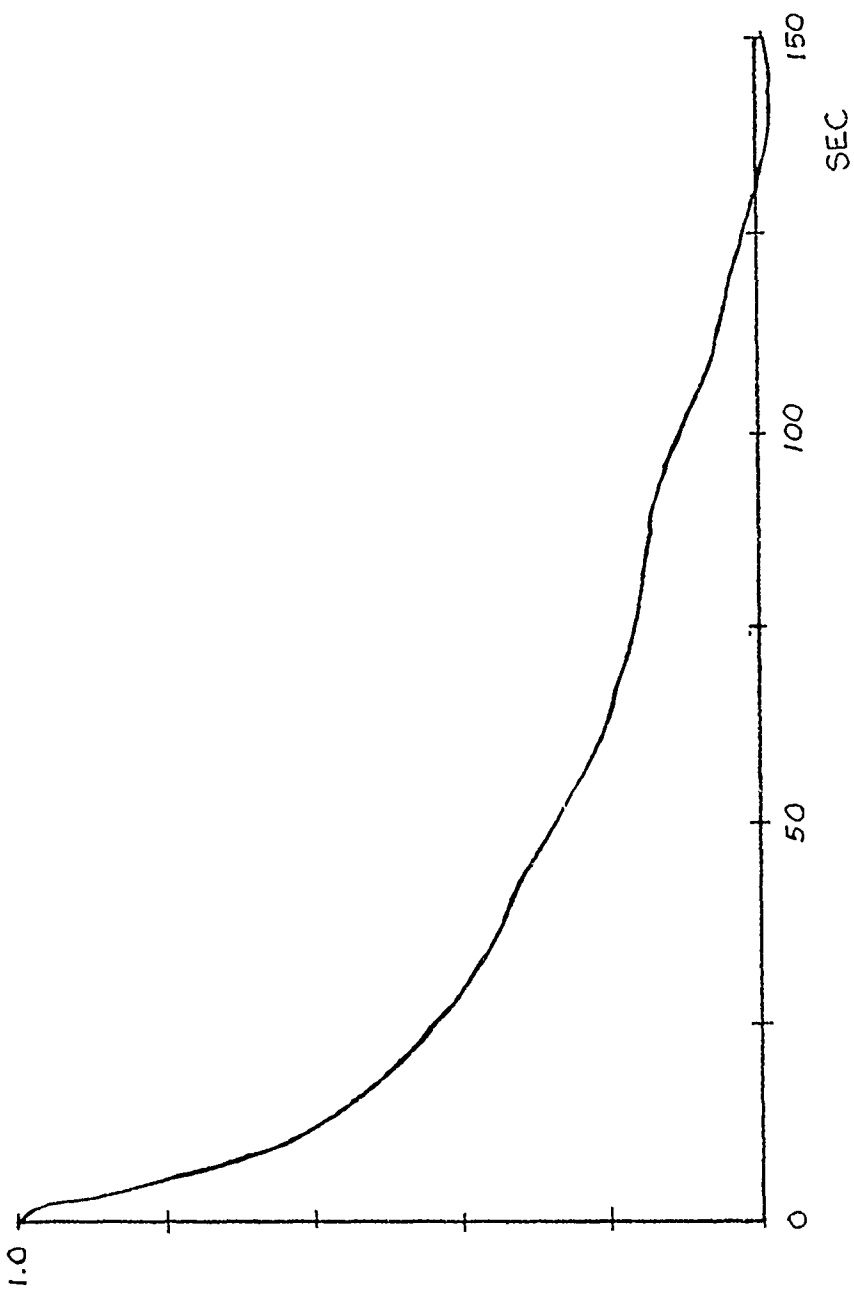
Fig. 6-1 Autocovariance of downstream fluctuations at 2 m depth
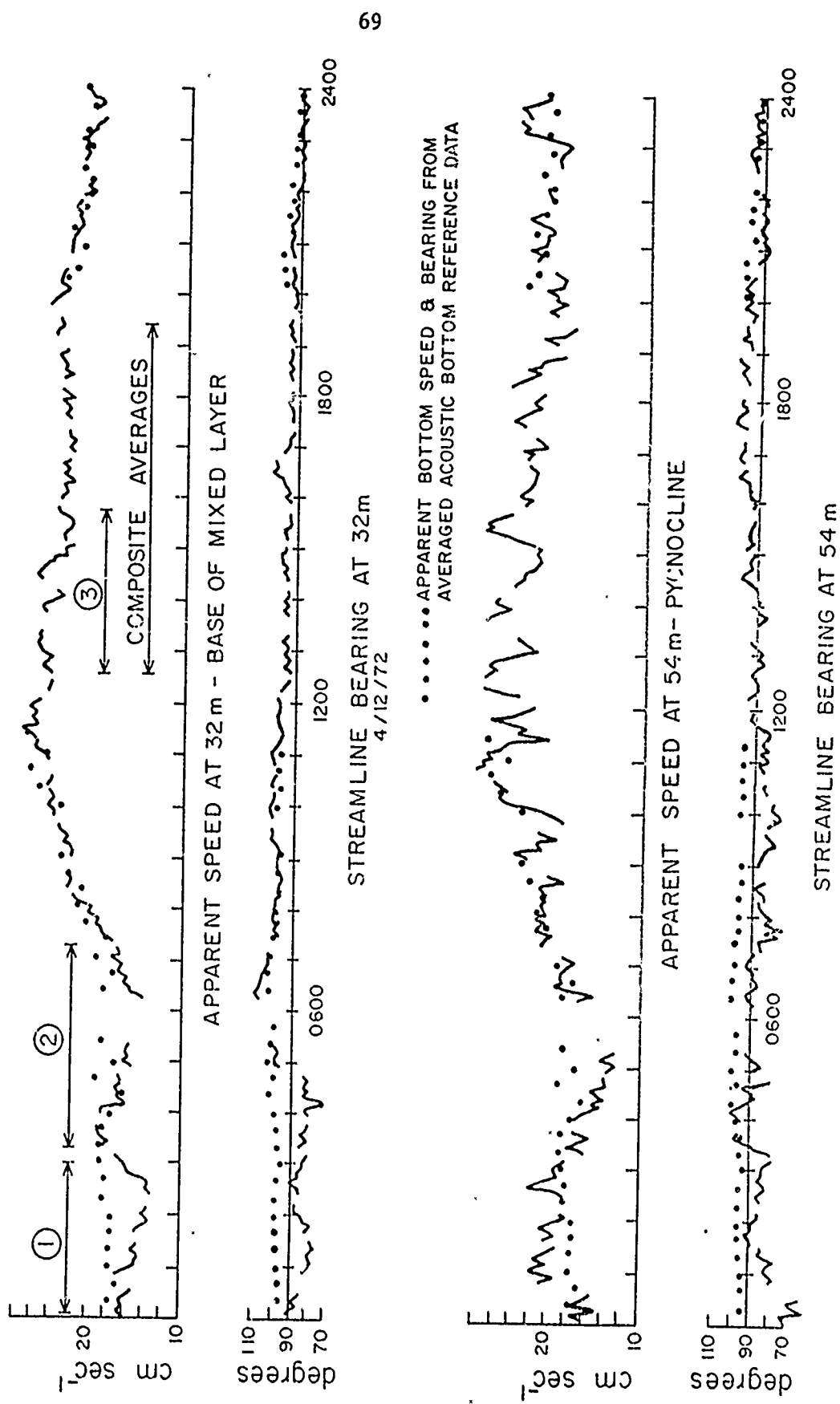
Fig. 6-2 Relative currents at 32 m and 54 m, Apr. 12, 1972

Depth m	Speed cm-sec⁻¹	Bearing degrees	U cm-sec⁻¹	V cm/sec	$\overline{-uu}$ cm²-sec⁻²	$\overline{-vv}$ cm²-sec⁻²	$\overline{-ww}$	$\overline{-uv}$ cm²-sec⁻²	$\overline{-uw}$	$\overline{-vw}$	$|\tau|$
2	19.53	73.0	19.53	0	-4.30	-1.37	-1.14	-.35	-.58	+.33	.67
4	21.78	74.7	21.77	-.66	-1.96	-1.01	-.57	-.02	-.19	+.27	.33
8	22.95	74.4	22.94	-.54	-1.30	-1.09	-.58	-.11	+.08	+.43	.44
12	23.48	74.4	23.48	-.58	-1.15	-.87	-.62	-.17	+.02	+.29	.29
16	23.24	75.8	23.22	-1.14	-1.15	-1.21	-.65	-.15	+.06	+.39	.39
20	23.75	79.4	23.60	-2.63	-.97	-1.28	-.54	-.01	+.02	+.33	.33
26	24.17	88.0	23.34	-6.25	-.83	-.91	-.55	-.05	+.13	+.23	.26
32	23.62	96.7	21.64	-9.47	-.46	-.37	-.31	+.01	+.07	+.05	.09

Table 6.2

Composite Average of 5 hours of data taken

April 12, 1972 ~ 1230-1930

Depth m	Speed cm/sec	Bearing degrees	U	V	$\overline{-uu}$	$\overline{-vv}$	$\overline{-ww}$	$\overline{-uv}$	$\overline{-uw}$	$\overline{-vw}$	$|\tau|$
2	14.01	70.4	14.01	0	-1.64	-.55	-.63	-.12	-.41	+.06	.41
4	15.01	72.6	15.00	-.59	-.95	-.42	-.29	+.02	-.15	+.11	.19
8	16.08	72.5	16.07	-.59	-.55	-.36	-.22	0	-.01	+.13	.13
12	16.73	73.4	16.70	-.89	-.36	-.28	-.22	-.01	-.01	+.08	.08
16	16.45	77.0	16.34	-1.89	-.35	-.44	-.19	-.04	+.04	+.12	.13
20	15.25	84.6	15.75	-4.00	-.27	-.41	-.13	-.03	+.02	+.07	.07
26	15.65	92.8	14.47	-5.94	-.13	-.19	-.06	0	+.02	+.01	.02
32	16.32	95.2	14.67	-7.16	-.09	-.23	-.05	0	+.01	+.01	.01

Table 6.3

Composite Average of 8 hours of data

Taken during period 1300-2230 Apr. 11, 1972

7 CALCULATION OF SURFACE STRESS

7.1 Introduction

Without means of directly measuring the stress on the underside of the ice, we must infer its value from current measurements. In this chapter some standard methods for estimating the surface stress will be discussed, and it will be shown that such methods give ambiguous results when applied to our data. Then it will be shown that horizontal homogeneity, upon which most methods depend, cannot be assumed in our case, and u_* will be calculated from a combination of measurements.

7.2 Surface Layer Methods

If conditions are steady enough to get suitable time averages, we can make direct measurement of the Reynolds stress, $-\rho\overline{uw}$, at a level close enough to the surface to be considered within the surface layer as discussed in Section (2.2) and equate it directly to the surface stress, ρu_*^2 (for simplicity, hereafter ρ will be considered to have the value 1.0 and surface friction stress and u_*^2 will be considered identical). Recalling that in the surface layer the lateral stress is zero, it is obvious from Table (6-2) that at 2 m there is already considerable turning of the stress "vector." However, the modulus of the stress at 2 m, .67 cm^2-sec^{-2}, sets a lower bound on any surface stress calculation and we can say immediately that $u_*(min) = \sqrt{.67} = .8$ cm-sec^{-1}.

A consequence of Rossby-number similarity discussed in Section (2.6) is that the logarithmic profile is not confined to the surface layer proper but extends into the lower outer layer in order to satisfy the matching requirements. Tennekes (1973) suggests that in the neutral boundary layer, the log profile may be expected in roughly the lower tenth of the total boundary layer thickness, which he defines as $\xi = fz/u_* = .3$.

We can assume a log profile and use measured values of U at 2 and 4 m to solve for u_*, i.e., we integrate the dimensionless wind shear equation

$$\phi_m = \frac{kz}{u_*}\frac{\partial U}{\partial z} = 1$$

between the limits $z = -4$ and $z = -2$, to get

$$u_* = k(U_4 - U_2)/\ln 2$$

Using mean values from Table (6.2) and k = .35 we get

$$u_* = 1.1 \text{ cm-sec}^{-1}$$

The use of k = .35 requires some explanation. It is the value reported by Businger, et al. (1971) for conditions on the Kansas prairie with $Ro_* = u_*/fz_0 \sim 10^7$. We can anticipate by solving the law of the wall, Equation (2.4.1), with $u_* = 1 \text{ cm-sec}^{-1}$ that $z_0 \sim .1$ cm and $Ro_* \sim 10^5$. From the arguments given by Tennekes (1973) and discussed in Section (3.4), we might expect k to be larger than .35. For k = .4, $u_* = 1.3$ cm-sec. Thus even if the log profile is valid to 4 m, which we have not demonstrated, there is still considerable uncertainty in the value in u_* due to the uncertainty in k.

We can investigate the effects of slight stability on u_* by integrating the log-linear profile, Equation (3.5.2), and using $\mu_* = 1.0$ and $L \sim 35$ m, i.e., the same hypothetical case discussed in Section (5.5). Using the value $\beta = 4.7$ reported by Businger, et al. (1971), we get

$$u_* = k(U_4 - U_2)/(\ln 2 + \frac{4.7(2)}{36})$$

which yields

$$u_* = .8 \text{ cm-sec}^{-1}$$

for the same data. Clearly, even slight stability has a large effect on the calculation of surface stress.

Using the neutral value for u_*, we can evaluate the depth $z = .03 \, u_*/f$ which marks an outer limit on the validity of the log profile according to Tennekes (1973). For $u_* = 1.1$, $f = 1.4 \times 10^{-4}$, this is about 2.4 m, so that

the value of U at 4 m in a log profile calculation is possibly not justified.

From the examples and arguments given, it is fairly clear that surface layer profile methods will not give a clear estimate of the surface stress from our data.

7.3 Momentum Integral Methods

We can define functions $M_y(z)$ and $M_x(z)$ such that

$$M_y(z) = \int_0^z [V(z') - V_R] \, dz'$$

$$M_x(z) = \int_0^z [U(z') - U_R] \, dz'$$

(7.2.1)

If we multiply each by $-\rho$, they can be identified with the total mass transport <u>above</u> the level z in the y- and x-directions respectively.

By integrating the mean component equations, (2.2.9), from the surface to some level z we have

$$-fM_y(z) = \int_0^z F_x \, dz - \overline{uw}(z) + u_*^2$$

$$fM_x(z) = \int_0^z F_y \, dz - \overline{vw}(z)$$

(7.2.2)

where we have lumped local pressure gradients, advective accelerations, etc., into the force vector $\widetilde{F}$.

Before Equations (7.2.2) can be applied to the data set of Table (6-2) we need to estimate the importance of the local rate of change of the mean true velocity. If we take the change in the mean downstream components for the first and last data files of the composite average and divide by the time between them we have for the triplet at 2 m

$$(U-U_R)_{END} - (U-U_R)_{START}/\Delta t \sim \frac{\partial U_f}{\partial t} \sim 3 \times 10^{-6} \text{ cm-sec}^{-2}$$

By comparison, $-f(V-V_R)$ at 2 m is $\sim 12 \times 10^{-4}$ cm-sec^{-2} so that apparently the time derivative term can be ignored for currents as steady as those chosen for the composite average.

Hunkins (1974b) made integrated mass-transport calculations using one-hour mean currents measured independently at the 1972 AIDJEX site and found the mean time dependent term to be an order of magnitude less than the Coriolis term. His measurements included relatively unsteady currents.

If we assume the flow to be steady and horizontally homogeneous then

$$-u_*^2 = \tau_x(z) + fM_y(z) \tag{7.2.3}$$

$$\tau_x(z) = -\overline{uw}(z)$$

Thus, if a level at which stress vanishes can be identified, the surface stress can be calculated from the mean V profile alone.

Table (7-1) shows a numerical integration of $M_y(z)$ for the data in Table (6-2). It is obvious that if we ignore measured stresses and assume that the stress vanishes near the reference level, 32 m, then

$$u_*^2 = 3.0 \text{ cm}^2\text{-sec}^{-2}$$

However, if we utilize the stress measurement at 2 m and apply Equation (7.2.3) we get

$$u_*^2 = .8 \text{ cm}^2\text{-sec}^{-2}$$

For 4 m we get .7 $\text{cm}^2\text{-sec}^{-2}$, etc.

Thus, if we retain the condition that horizontal homogencity holds, i.e., that $\int F_x dz = 0$, then we must conclude that either our stress measurements or direction measurements are wrong or that the method fails. Rather than admit any of these, we shall investigate the effect of including a topographic term.

7.4 A Non-Homogeneous Estimate

In order to estimate the magnitude of the topographic force, $\tilde{F}$, we can find the difference of its integrated effect at two levels by considering directly measured quantities.

Let

$$\mathcal{F}_x(z) = \int_0^z F_x(z') \, dz'$$

$$\mathcal{F}_y(z) = \int_0^z F_y(z') \, dz'$$

We can write the first of Equations (7.2.2) as

$$\mathcal{F}_x(z) + u_*^2 = -[fM_y(z) + \tau_x(z)]$$

Again using a finite difference approach we can determine $\bar{F}_x(z)$ between levels from $\Delta\mathcal{F}_x(z) = \bar{F}_x \Delta z$. These calculations are summarized in Table (7-2).

This technique does not divulge information about the function F_x in the upper 2 m. The origin of the force field is not clear but we assume that it is set up by some large-scale inhomogeneity and that in the surface layer it does not vary wildly. If we decide to treat F_x as constant in the upper 4 m, we can estimate the surface stress from

$$u_*^2 = -[fM_y(z) + \tau_x(z)] - \bar{F} \cdot z \qquad @ \ 2 \ m$$
$$= .97 \ cm^2\text{-sec}^{-2}$$

It might seem more logical to extend F_x to the surface with the slope given by our estimate at 3 and 6 m. If that is done

$$u_*^2 = 1.1 \ cm^2\text{-sec}^{-2}$$

However, it might seem just as plausible to say that F_x decreases to zero at the surface; this yields

$$u_*^2 = .9 \text{ cm}^2-\text{sec}^{-2}$$

Thus we chose $\underline{u_*^2 = 1.0 \pm .1 \text{ cm}^2-\text{sec}^{-2}}$ as the estimate utilizing the maxi- mum amount of information available.

To summarize, the method for estimating stress involves:

(1) Taking long enough averages to get stable estimates of the momentum flux at 2 and 4 m.

(2) Using mean velocity profiles to estimate the function $M_y(z)$ at 2 and 4 m.

(3) Calculating $\mathcal{F}_x(z)$ as the difference of the sums of $\tau_x + M_y$ at 2 and 4 m.

(4) Adding $-(\tau_x + M_y) + \langle\mathcal{F}\rangle$ to get u_*^2.

In Chapter 8 the composite profiles are non-dimensionalized by u_* and u_*/f where u_* is calculated by this method. Comparison with theoretical treatments tends to confirm the validity of this procedure, although certainly not to better accuracy than given above.

7.5 Reflections on the Momentum Integral Method

So far we have tacitly assumed that the surface stress, u_*^2 is skin friction, i.e. tangential stress due to viscosity and the no-slip condition at the surface. Although it is not a priori obvious, we assume that the turbulent structure responds basically to this type of stress since the surface layer is small compared to the horizontal distance between the larger features. However, in determining the total stress the ice exerts upon the water, form drag, i.e. the normal stress (pressure) exerted against bluff irregularities in the ice surface (Batchelor, 1967, Chapter 5), must be considered. Clearly, forces such as F discussed in the previous section will manifest themselves as form drag.

We can conceptually break the downstream Coriolis force, $f(V-V_R)$ into two parts: one that balances the turbulent stress gradient and one that balances the local pressure-gradient, advective-acceleration term, F_x. Thus

$$-fv_E = \frac{\partial \tau_x}{\partial z}$$

$$-fv_L = F_x$$

The values for v_E and v_L are tabulated in the rightmost two columns of Table (7-2).

The origin of v_L is not clear, but seems to indicate that non-linear terms other than the vertical Reynolds stress gradient are important. It is obvious that v_L, whatever its cause, is important in stress calculations involving mean profiles in the entire boundary layer. Figure (7-1) shows velocity profiles for the three frames for the period 1230 to 1930 (AST) on Apr. 12. The zero reference level is the under-ice elevation at the main

frame. Integration of the outer frame profiles will yield an even higher estimate of surface stress than the main frame. Figure (7-2) contains the same information for Frames 1 and 3 (main and ridge) in the form of hodographs. The under-ice topography map, Figure (4-1), shows that topographic changes in the vicinity of the outer frames are more abrupt, possibly explaining the curious shapes of the current profiles there.

Figure (7-3) demonstrates the effect of a different "fetch" on the main-frame profile. During most of the storm from Apr. 10 through Apr. 13, the ice motion was almost due west, but for a few hours on Apr. 14 the current direction changed. The profiles marked by diamonds were taken from a twenty-minute average early in the storm on Apr. 11 and the circles represent a twenty-minute average taken on the afternoon of Apr. 14. In terms of speed, conditions during the latter case were not steady, but the direction and shape of the profile are representative of several hours of data, implying that the flow direction has an appreciable effect on the shape of the velocity profile. Unfortunately, threshold problems with the independent current-meter component, v_m, on the outer (fixed) frames made determination of mean profiles there impossible during the latter time.

Figure (7-4) shows a comparison of measurements made by the Lamont group (Hunkins, 1974b) to ours for the period 1200-2400 (AST) on Apr. 12. The Lamont current-meter array was situated approximately 110 m southeast (roughly downstream) of our main mast in what appeared from the upper surface to be smoother ice. The ice velocity was determined for the 12 hour period from satellite navigation data as reported by Hunkins (1974b). The ABR was non-functional during part of this time and thus did not provide an independent ice motion measurement.

The solid vectors emanating from the points labeled "Ice" are stress vectors (acting on the ice) calculated using the momentum integral (mass transport) technique as described by Hunkins (1974b). For the Lamont measurements the reference level was 25 m, while for ours it was 32 m. From these we see the somewhat startling result that flow profiles measured at two points quite close to each other, each apparently exhibiting similar surface layer behavior and about the same amount of total turning, give estimates of stress that vary by a factor of nearly 2 1/2. It can be argued that if we were to integrate to 25 m, our stress estimate would be somewhat lower, but the main point is that the major contribution to the momentum integral in our profile comes because there is no appreciable turning above 16 m in contrast to Hunkins' profile in which turning starts at about 8 m. Reference to Figure (7-2) is helpful in visualizing the area of the momentum integral, $f \int (V-V_R)dz$.

Hunkins (1974b) has demonstrated that the momentum integral will give a measure of the total stress on the ice including form drag if it is averaged over a suitable horizontal area. The evidence presented in this section implies that determining a suitable horizontal average may require very extensive measurements. We shall return to this in the last chapter.

Depth m	$V-V_R{}^a$ $\mathrm{cm\text{-}sec}^{-1}$	$V-V_R$	$\overline{(V-V_R)}\Delta z$ $(\times 10^2)$	$fM_y(z)^b$ $\mathrm{cm}^2\text{-}\mathrm{sec}^{-2}$	$-\overline{uw}{}^c$ $\mathrm{cm}^2\text{-}\mathrm{sec}^{-2}$
0	+9.47 *			0	
		9.47	−18.9		−.58
2	+9.47			−.26	
		9.14	−18.3		−.19
4	+8.81			−.52	
		8.87	−35.4		+.08
8	+8.93			−1.02	
		8.91	−35.6		+.02
12	+8.89			−1.52	
		8.61	−34.4		+.06
16	+8.33			−2.00	
		7.58	−30.4		+.02
20	+6.84			−2.43	
		5.03	−30.2		+.13
26	+3.22			−2.85	
		+1.61	−7.2		+.07
32	0			−2.95	

* No turning in upper 2 m assumed

a V_R is reference lateral velocity at 32 m

b
$$M_y(z) \;=\; \int_0^z [V(z') - V_R]dz'$$

c Measured momentum flux values from Table (6.2)

Table 7.1

Mass transport calculations for the cross-stream component

Depth	Δz	$\tau_x(z) + u_*^2$	$\Delta \tau_x$	$\bar{F}_{x}$ (x 10^4)	v_L	v_E
0						
	-200					
2		+.84	-.13	+6.5		
	-200				-.3	9.1
4		+.72	+.23	-5.8		
	-400				+7.1	1.8
8		+.94	+.36	-14.0		
	-400				+8.5	0.4
12		+1.50	+.44	-11.0		
	-400				+8.4	0
16		.+1.94	+.50	-12.5		
	-400				+6.3	0.5
20		+2.41	+.31	-5.2		
	-600				+2.8	0.4
26		+2.72	+.15	-2.5		
	-600					
32		+2.87				

Table 7.2

The force field and velocity decomposition

discussed in Sections (7-4) and (7-5)

cm sec^{-1}

CROSS-STREAM DEFECT
$V_{32}- V$

cm sec^{-1}

DOWNSTREAM DEFECT
$U_{32}- U$
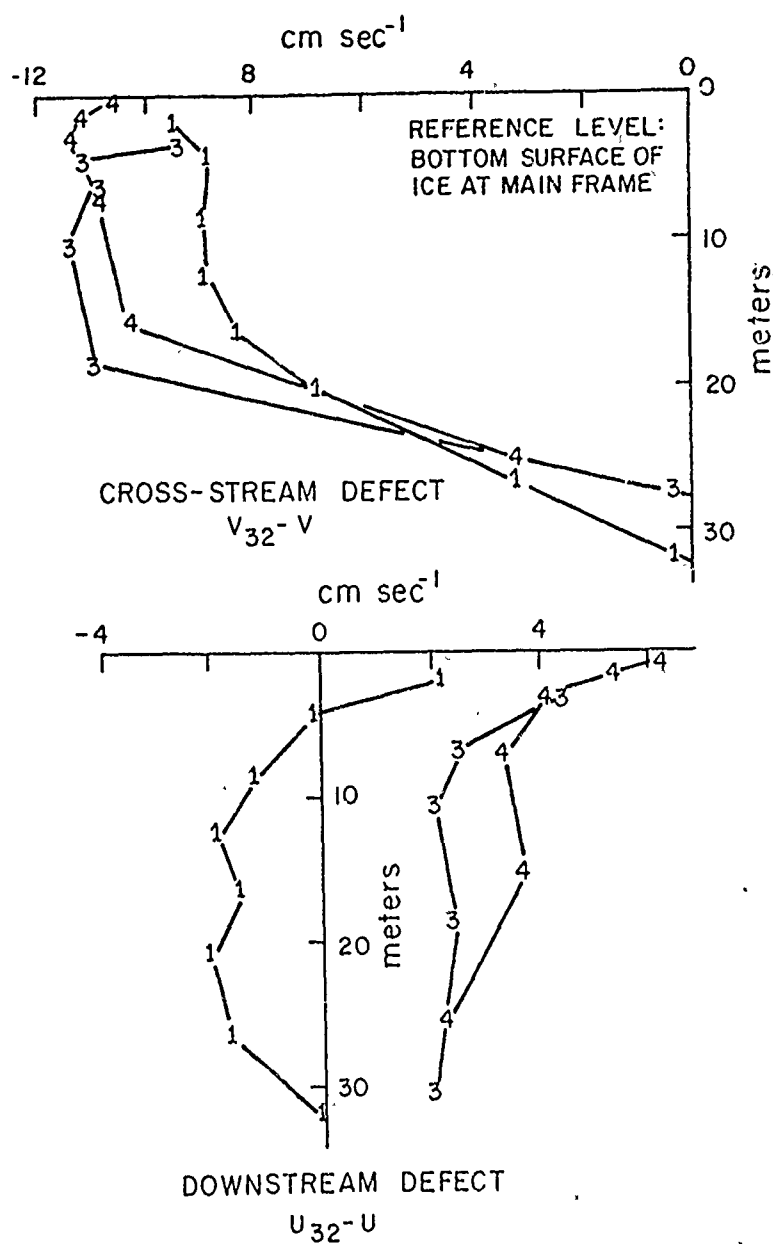
LABELS	MEASUREMENTS FROM
①	MAIN FRAME UNDER INSTRUMENT SHED
③	FRAME #3 UNDER PRESSURE RIDGE
④	FRAME #4 FLAT BEYOND RIDGE

Fig. 7-1 Mean current profiles on all three masts for the
composite averaging period on Apr. 12. Reference
velocity is at 32 m on the main frame.
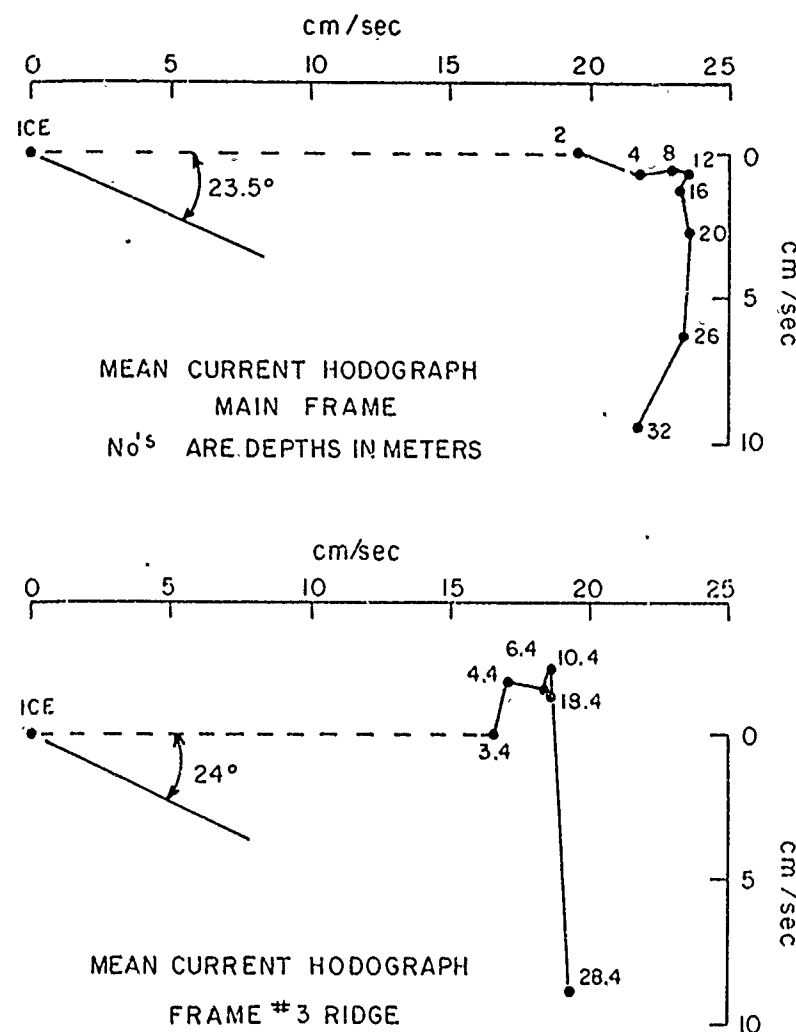
Fig. 7-2 Hodographs of composite currents for main frame and Frame 3
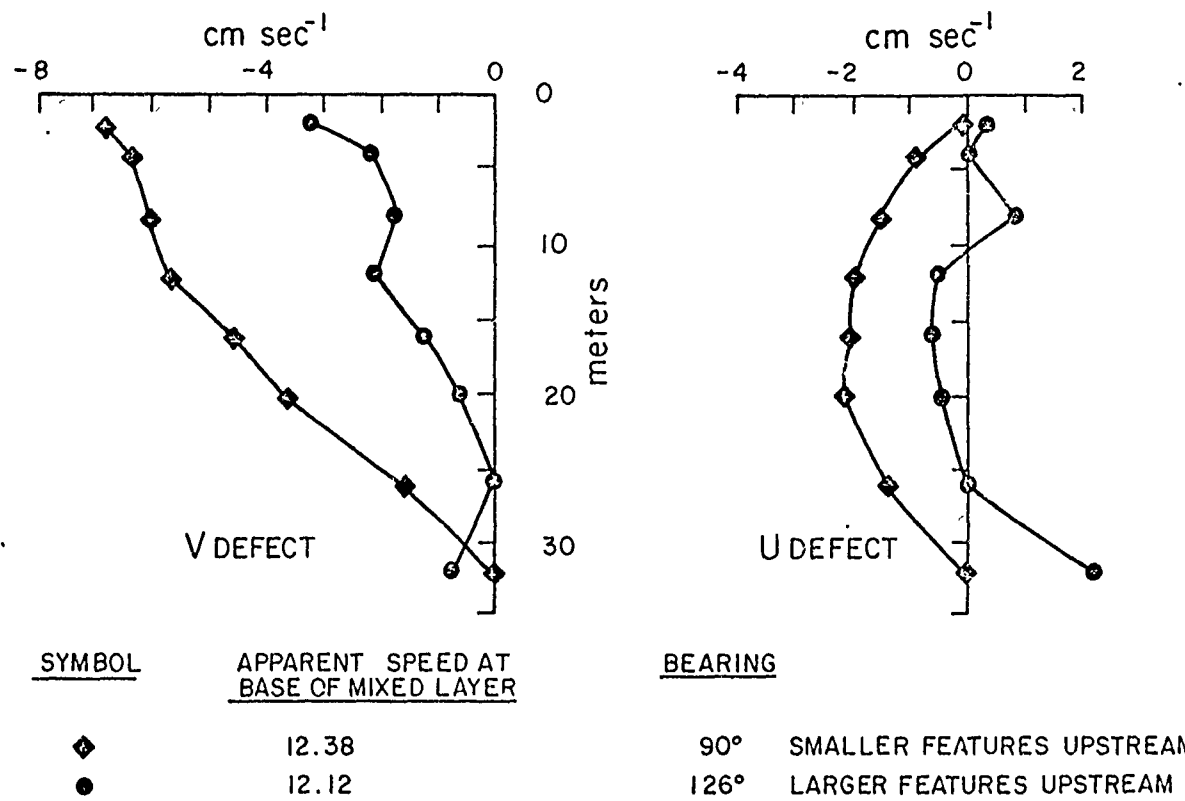
Fig. 7-3 Twenty-minute mean cross-stream profiles showing the effect of different flow direction
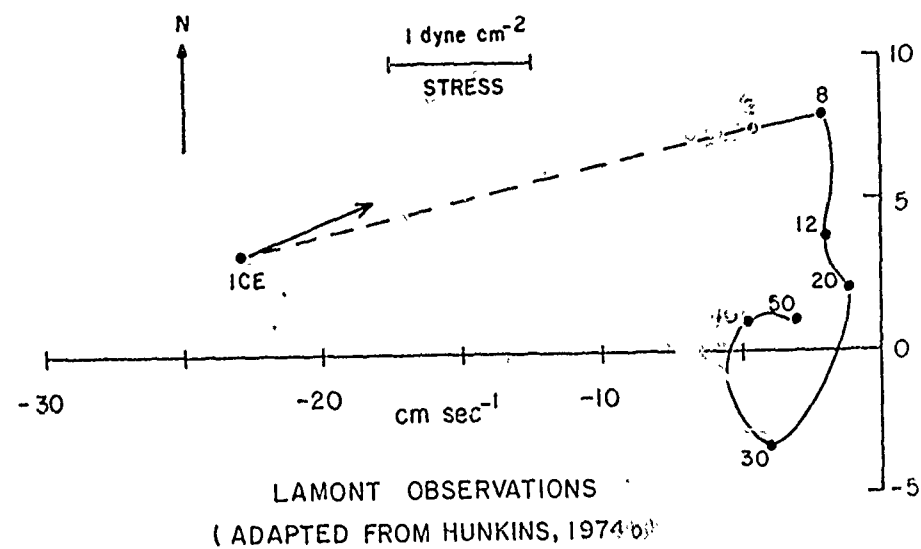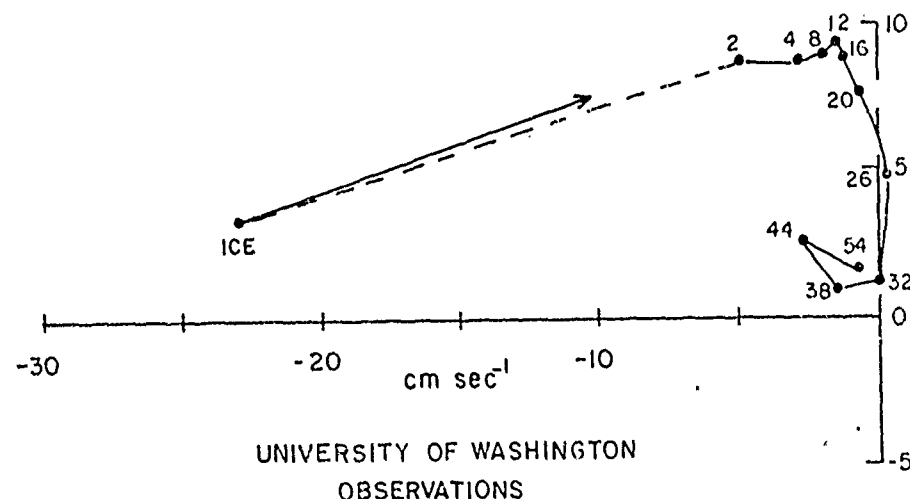
Fig. 7-4   Comparison of independent measurements made about 110 m
apart at the AIDJEX site, 1200-2400 (AST) on Apr. 12, 1972

8 COMPARISON OF MEASUREMENTS AND THEORY

8.1 Turbulence Theories

With the friction velocity calculated for the composite data set,
Table (6-2), we can calculate a scale length for the outer layer:

$$u_*/f = .01/1.4 \times 10^{-4} = 70 \text{ m}$$

With this length scale and u_* we can non-dimensionalize the mean profiles
of velocity and velocity covariances. Figures (8-1) through (8-4) show
theoretical predictions from several models plotted as curves with solid
markers showing measured (non-dimensionalized) values. These graphs prob-
ably represent the most important results of this project.

A word of explanation is in order regarding the choice of theoretical
curves in these figures. In most cases there was so little difference among
the models for the neutral PBL that results from Businger and Arya's first-
order model are shown for convenience since we wanted to show the effect
of positive stability. The stable case shown is the one closest to neutral
treated in their model. Clearly, a K-model will not explicitly predict
turbulent variances and the non-horizontal shear stress, $\overline{uv}$, however, and
for these, the values from Wyngaard, et al., (1973) and Deardorff (1972)
are shown. Incidentally, the pycnocline at 35 m in effect imposes a "lid"
on the PBL at about $\xi = .5$.

Figure (8-1) depicts the mean dimensionless downstream current. Al-
though not shown, because of the scale of the plot, its value at the surface
(U_R/u_*) is 22. For the Wyngaard et al. model the surface value is about
32. This discrepancy is reconciled by noting that in the surface layer U

is a fairly strong function of Ro_*, which $\sim 10^7$ for the standard conditions of the model. For $Ro_* = 10^5$, Shir's (1973) model predicts the corresponding value of U/u_* to be 24.

Figure (8-2) demonstrates the V profile's departure from ideal already discussed in Section (7.4) and attributed to topographic effects. The open circles represent v_E/u_* calculated as described in Section (7.4). Figure (8-3) shows the shear stresses. The curve for $\overline{uv}/u_*^2$ is taken from Wyngaard et al. Considered together, Figures (8-1), (8-2) and (8-3) demonstrate well the coupling between the stress gradient, the Coriolis force and the form drag force, $\vec{F}$. Clearly the $\overline{uw}$ stress gradient alone is not sufficient to balance the downstream Coriolis force associated with the V component. On the other hand, the $\overline{vw}$ stress and the U component fit their respective horizontally homogeneous models quite nicely, indicating that the lateral component of $\vec{F}$ is not important in that balance. Thus we conclude that $\vec{F}$ must be in the direction of ice motion and it is natural to consider it a manifestation of form drag.

Figure (8-4) shows dimensionless variances, the sum of which is twice the turbulent energy. Curves from Deardorff's model seem to show more of the structure demonstrated by our measurements than the simpler second-order model. The fact that measured levels of turbulent kinetic energy deep in the layer are higher than model predictions might be because the mixed layer is bounded by an active pycnocline rather than by a rigid lid as in Deardorff's model or by nothing as in the Wyngaard et al. model.

At first glance, it seems that the turbulent field is not much affected by the form drag field that makes itself so noticeable in the mean V component, and we are tempted to classify the layer as slightly stable, mainly

because of the behavior of the downstream stress, $\overline{uw}$. There are several objections to this, however. First, the measured $\overline{vw}$ stress fits a neutral model very well. Secondly, the turbulent energy does not behave as if there were a vertical force affecting it, particularly the $\overline{w^2}$ component, which fits Deardorff's neutral model very closely. Thirdly, the arguments of Section (4.5) indicate that a much steeper slope to the density profile would be required for $\mu_* = 10$, say, than was observed.

Intuitively, the suppression of $\overline{uw}$ with depth might be explained by again referring to the local pressure-gradient force $\vec{F}$. We can picture it as a standing field being advected along with the ice with just the right magnitude to bring Equation (2.2.9) into balance. In the region deeper than 2 m this force is negative, so that we can visualize a blob of fluid with excess momentum being transported downward by a turbulent eddy but feeling a restraining force in the x-direction. The net effect then will be to inhibit momentum exchange in a manner somewhat analogous to the action of a stably stratified environment except that it occurs in the x-direction. Since we chose the x-axis to coincide with the ice motion, the cross-stream momentum exchange is not affected so much.

Some insight may possibly be gained by writing down a pair of the co-variance equations. For simplicity, but with no rigorous justification, we assume that the effects of non-homogeneity are not significant except in the pressure-velocity covariance terms. Then for steady-state conditions we can write the $\overline{u^2}$ and $\overline{v^2}$ covariance equations (from Equation (2.2.6)) as

$$\overline{uw}\,\frac{\partial U}{\partial z} + \frac{1}{2}\frac{\partial}{\partial z}\,\overline{uuw} = -\overline{u\frac{\partial p}{\partial x}} - 2\omega(\overline{uw}\cos\phi - \overline{uv}\sin\phi) + \frac{\overline{\varepsilon}}{3} \qquad (8.1.1)$$

$$\overline{vw}\,\frac{\partial V}{\partial z} + \frac{1}{2}\frac{\partial}{\partial z}\,\overline{vvw} = -\overline{v\frac{\partial p}{\partial y}} - 2\omega\,\overline{uv}\sin\phi + \frac{\overline{\varepsilon}}{3} \qquad (8.1.2)$$

In general, it is dangerous to try to infer much from cursory looks at complicated equations, but we can see from (8.1.1) that $\overline{uw}$ is closely coupled to $u\frac{\partial p}{\partial x}$ and we expect this term to be strongly affected by a local pressure gradient such as we have discussed. On the other hand, $\overline{vw}$ in Equation (8.1.2) is coupled to events in the x-direction (at least in this simplified version) only through the rotation term.

We thus conclude, although the evidence is somewhat ambiguous, that the boundary layer was essentially neutral and that the flattening of the $\overline{uw}$ stress profile was the result of topographic effects rather than stable stratification.

Figure (8-5) and (8-6) compare the non-dimensionalized profiles for the two composite averages summarized in Tables (6-2) and (6-3). For the latter case, Apr. 11, the average reference speed was 16.32 cm-sec^{-1} and $u_*^2 = .7$ cm^2-sec^{-2}. Current direction was almost the same in each case.

Of particular significance is the behavior of the cross-stream velocity near the bottom of the boundary layer. In Case A (reference speed = 16.3 cm-sec^{-1}), the reference level, 32 m, has dimensionless depth $\xi = .55$. In the second case, with u_* larger, the 32 m level falls at $\xi = .45$. The depth of the mixed layer remained constant at about 35 m, so we conclude that the depth of influence of the topographic force, $\overline{F}$, responds to u_*/f scaling rather than to the depth of the mixed layer. The importance of this will be discussed in Section (11.1).

The fact that the turbulent energy is larger on Apr. 12 may be related to the fact that we observed more activity in the pycnocline on that day (see Section 10.5) although this is not clearly established.

8.2 Similarity Constants

If we assume that the log profile is valid to 2 m and use the values for u_* calculated by the method outlined in Section (7.3) we can solve for z_o from

$$\ln z_o = \ln 200 - kU(2)/u_*$$

For $k = .35$ and $U(2)/u_* = 20$

$$z_o = 0.18 \text{ cm}$$

With the surface roughness scale established we can solve Equation (3.6.3) and (3.6.4) for the similarity constants $\underline{A}$ and $\underline{B}$

$$A = \ln Ro_* - \frac{kU_R}{u_*}$$

$$B = \frac{-kV_R}{u_*}$$

From the data for the two composite cases studied we can solve to get:

Date	u_*	Ro_*	A	B
4/11	.7	2.8×10^4	2.9	3.3
4/12	1.0	4.0×10^4	3.0	3.6

Although these values are within ranges reported for the atmosphere in the literature, our results show that topography can distort the profiles significantly and we expect the coefficients A and B to vary with position. In particular, we do not expect the non-dimensional cross-stream component V_R/u_* to be constant. It may be that B can be related to the gross roughness features of the ice and that A is not particularly sensitive to topography. If this is the case, the similarity approach may provide a viable means of predicting stress from ice motion or vice versa.

$(U_{32}-U)/u_*$
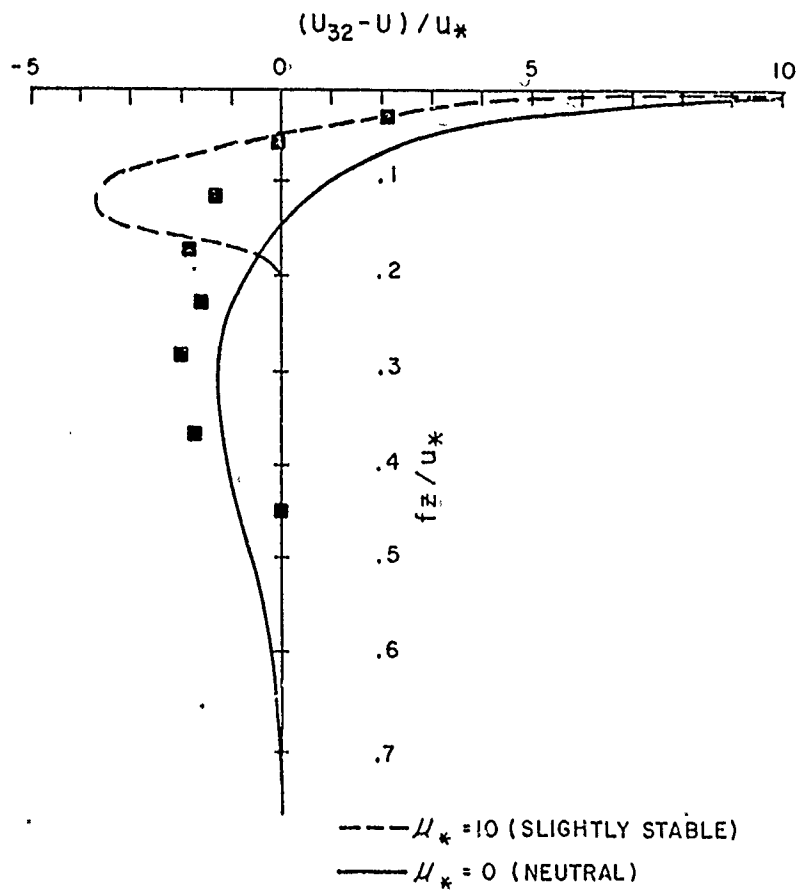
DOWNSTREAM DEFECT

Fig. 8-1 Non-dimensional downstream component with respect to
32 m reference. Curves are model predictions from
Businger and Arya, 1974. Solid markers are experi-
mentally determined data.
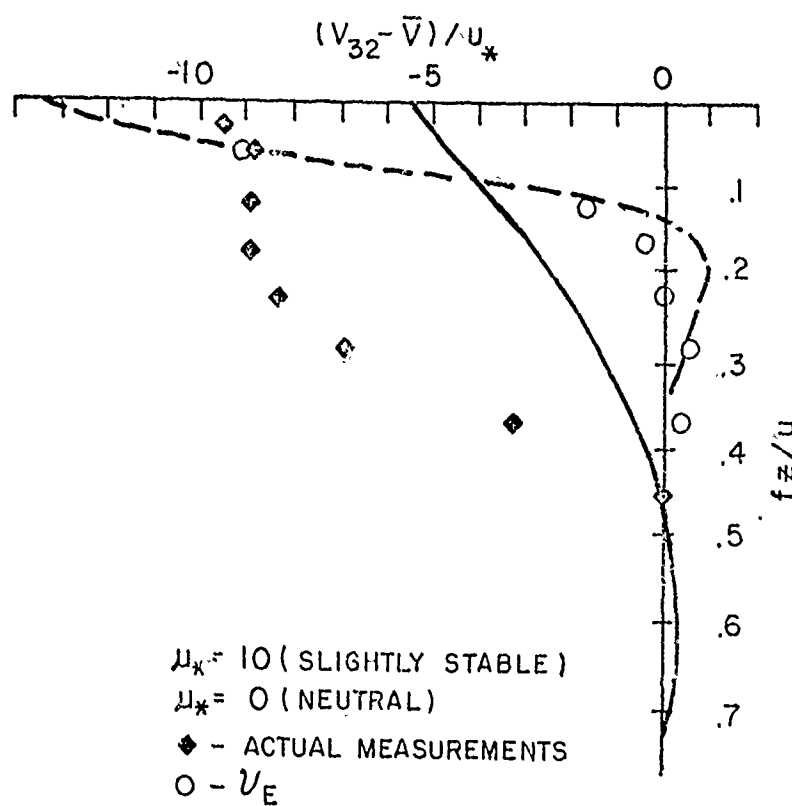
Fig. 8-2 Non-dimensional cross-stream component with respect to 32 m reference. See Section (7-5) for explanation of v_E. Curves are from Businger and Arya, 1974.
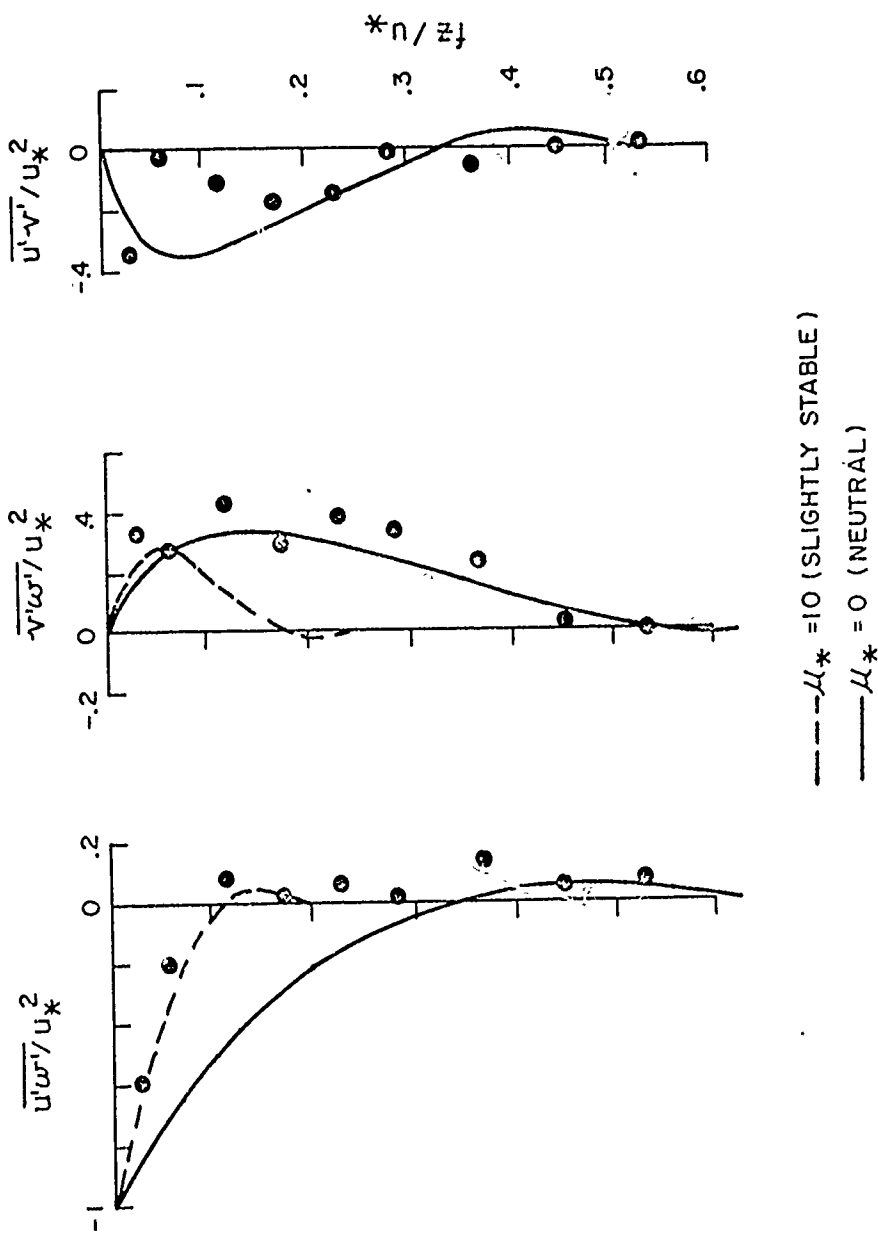
DIMENSIONLESS SHEAR STRESSES

Fig. 8-3 Non-dimensional shear stresses
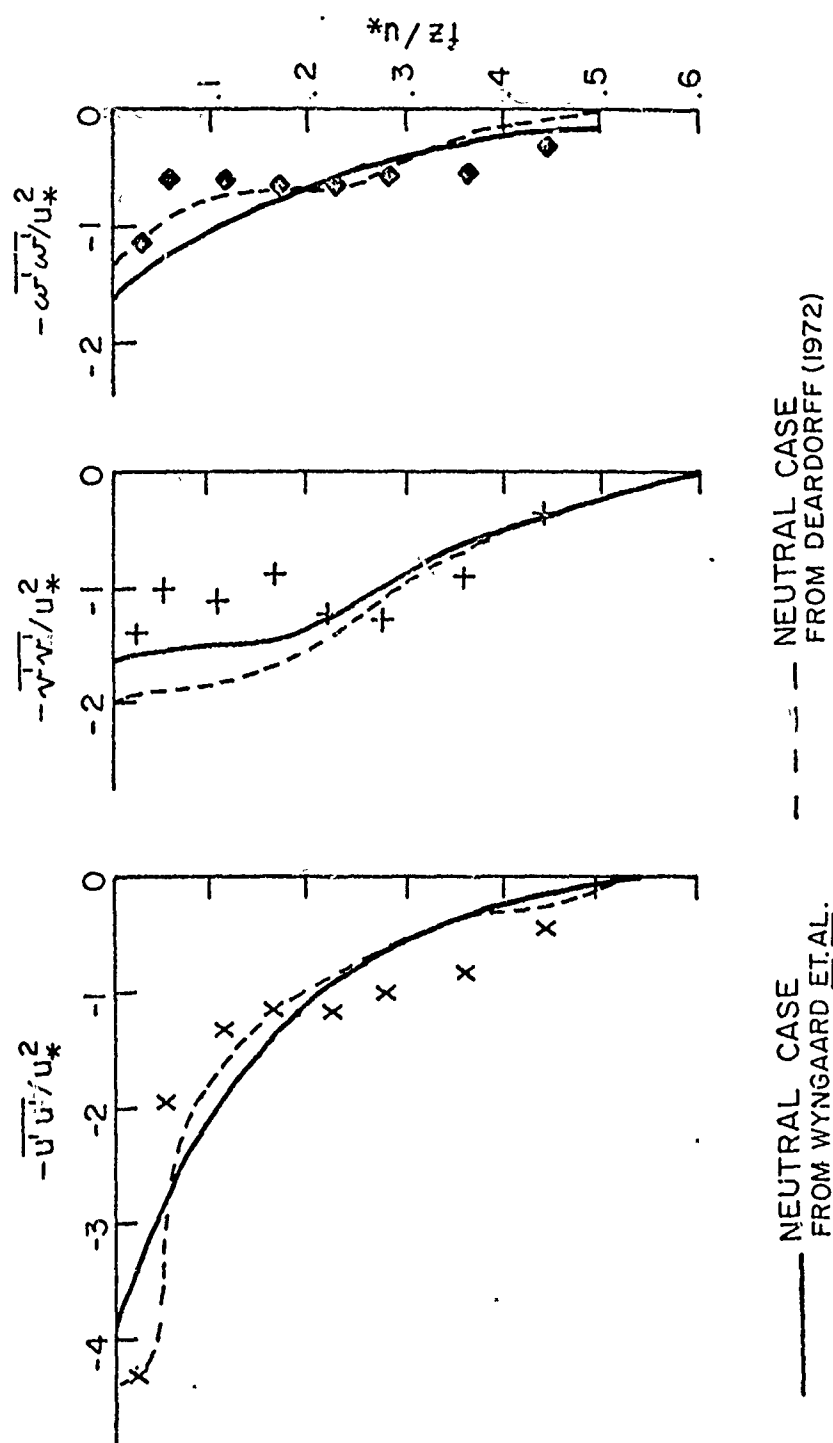
Fig. 8-4 Non-dimensional variances

$$(V_{32} - V)/u_*$$
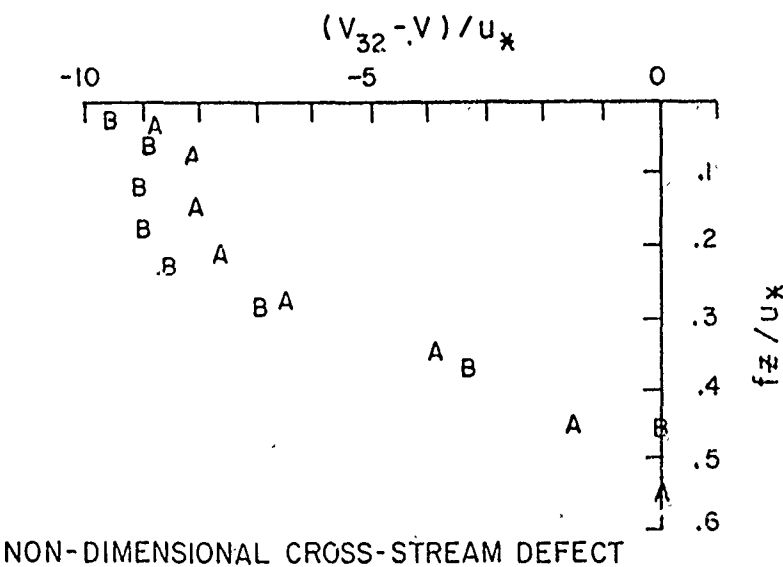
NON-DIMENSIONAL CROSS-STREAM DEFECT

$$(U_{32} - U)/u_*$$
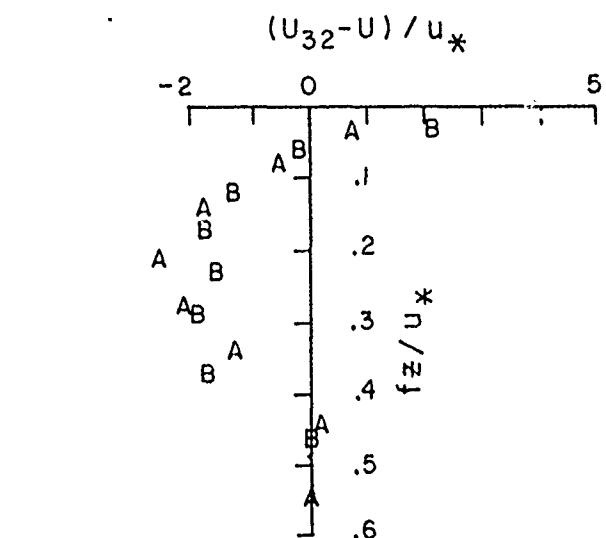
NON-DIMENSIONAL DOWNSTREAM DEFECT

LABELS	DESCRIPTION
A	8 HOUR COMPOSITE OF 20-MINUTE AVERAGES TAKEN 4/11/72 PM AVERAGE SPEED AT 32m.: 16.32 cm sec^{-1} AVERAGE BEARING 96°
B	5 HOUR COMPOSITE OF 20-MINUTE AVERAGES TAKEN 4/12/72 PM AVERAGE SPEED AT 32m.: 23.67 cm sec^{-1} AVERAGE BEARING 97°

Fig. 8-5 Comparison of non-dimensional mean-flow profiles for composite flows of different magnitude
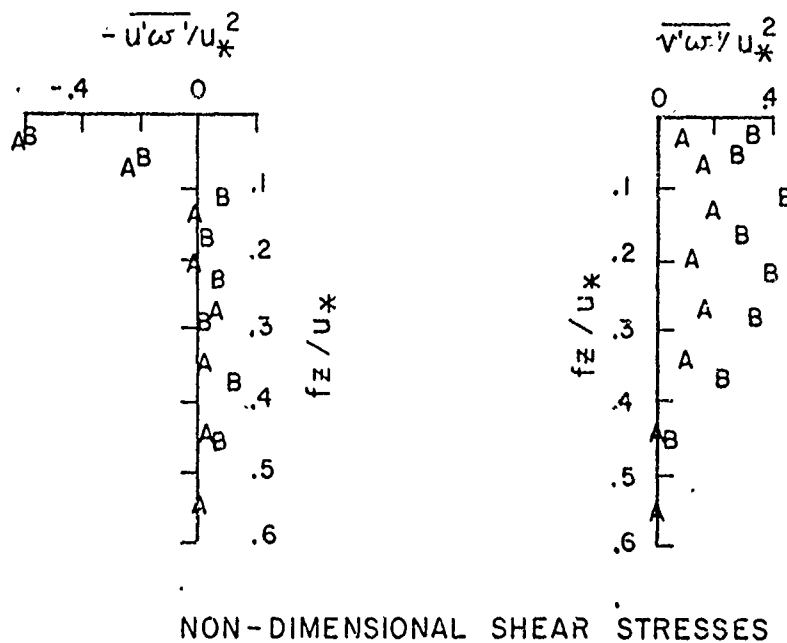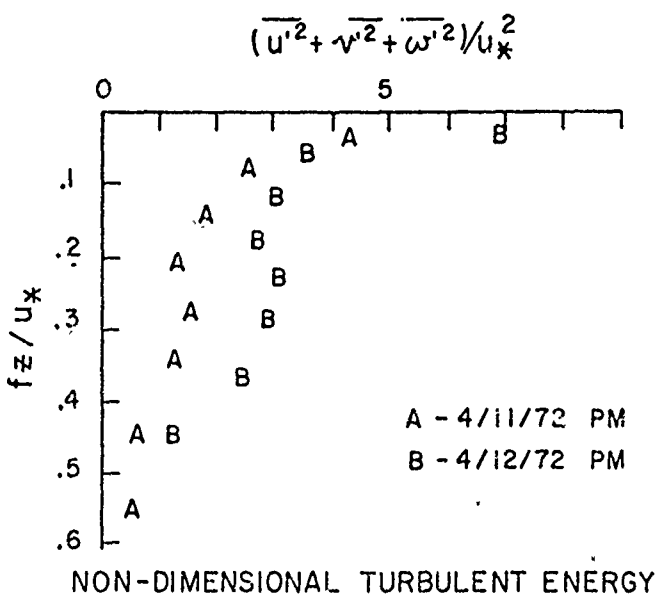
Fig. 8-6 Comparison of non-dimensional turbulent energy and
shear stress profiles for composite flows of different
magnitude

9. TURBULENCE SPECTRA IN THE OUTER LAYER

9.1 Introduction

There are two rather distinct reasons for investigating the spectral structure of turbulence measurements: first, that the spectrum can provide the best direct evidence as to whether or not the data collected have in fact measured the turbulent velocity field, and secondly, for the intrinsic interest in the comparison of measurements to turbulent spectral theory.

Extensive measurements of turbulent velocity spectra have been made in the surface layer of the atmosphere, and in the lower part of the outer PBL with the aid of towers and airplanes. However, the data collected during the 1972 AIDJEX project are probably the first for which simultaneous spectra have been calculated throughout the entire outer layer under more or less steady conditions of mean current and stability.

In this chapter, a cursory review of turbulent spectral theory is presented with emphasis placed on lending some justification to the methods of analysis used. Results are presented and used to derive an eddy viscosity profile from a mixing-length argument.

9.2. Spectral Theory

9.2.1 Definition of the Turbulent Energy Spectrum

Briefly, the turbulent energy spectrum is defined as the integral over spherical shells of radius $\kappa = \sqrt{\kappa_i \kappa_i}$ in wave-number space of one-half the sum of the diagonal components of the spectrum tensor $\phi_{ij}(\underset{\sim}{\kappa})$, which is the three-dimensional Fourier transform of the correlation tensor, $R_{ij}(\underset{\sim}{r})$.

$$R_{ij}(\underset{\sim}{r}) = \overline{u_i(\underset{\sim}{x},t)u_j(\underset{\sim}{x} + \underset{\sim}{r},t)}$$

where the overbar represents an ensemble average and the tilde denotes a vector.

$$\phi_{ij}(\underset{\sim}{\kappa}) = \frac{1}{(2\pi)^3} \iiint\limits_{-\infty}^{\infty} R_{ij}(\underset{\sim}{r}) \exp\{-i\underset{\sim}{\kappa}\cdot\underset{\sim}{r}\}\, d\underset{\sim}{r}$$

$$E(\kappa) = \frac{1}{2} \iint \phi_{ii}(\underset{\sim}{\kappa})\, d\sigma$$

$$\kappa^2 = \kappa_i \kappa_i$$

(Tennekes and Lumley, 1972, Chapter 8)

One-dimensional spectra can be defined by considering the correlation tensor along a spatial line, e.g.,

$$R_{ij}(\xi,0,0) = \iiint\limits_{-\infty}^{\infty} \phi_{ij}(\underset{\sim}{\kappa}) \exp\{i\kappa_1\xi\}\, d\kappa_1\, d\kappa_2\, d\kappa_3$$

$$= \int\limits_{-\infty}^{\infty} F_{ij}^{1}(\kappa_1) \exp\{i\kappa_1\xi\}\, d\kappa_1$$

where

$$F_{ij}^{1}(\kappa_1) = \iint\limits_{-\infty}^{\infty} \phi_{ij}(\underset{\sim}{\kappa})\, d\kappa_2\, d\kappa_3$$

(Lumley and Panofsky, 1964)

In general, the relationships between the energy spectrum and the various one-dimensional spectra are complicated, but under the assumptions of homogeneity and isotropy in space, stationarity in time and incompressibility, there exist simple relations between the one-dimensional spectra and the energy spectrum.

9.2.2 Isotropic, Homogeneous Turbulence

An isotropic, second-order tensor that depends on a single vector argument must have the form

$$\phi_{ij}(\underset{\sim}{\kappa}) = A(\kappa)\,\kappa_i\kappa_j + B(\kappa)\,\delta_{ij}$$

(Batchelor, 1953).

For an incompressible fluid, $\dfrac{\partial u_i}{\partial r_i} = 0$, and if the fluid is homogeneous

$$\frac{\partial}{\partial r_j}\,[R_{ij}(\underset{\sim}{r})] = \frac{\partial}{\partial r_i}\,[R_{ij}(\underset{\sim}{r})] = 0$$

and

$$\kappa_j\phi_{ij}(\underset{\sim}{\kappa}) = 0$$

since the functions are a Fourier-transform pair. Thus

$$A(\kappa)\kappa_j\kappa^2 + B(\kappa)\,\delta_{ij}\,\kappa_j = 0 \qquad\qquad B(\kappa) = -\kappa^2 A$$

The total energy in wave-number space between spheres of radius κ and $\kappa + d\kappa$ for an isotropic field is given by

$$\frac{1}{2}\,\phi_{ii}(\kappa)\,4\pi\kappa^2\,d\kappa = E(\kappa)\,d\kappa$$

Using these relations the spectrum tensor can be written in terms of the energy spectrum as

$$\phi_{ij}(\underset{\sim}{\kappa}) = \frac{E(\kappa)}{4\pi\kappa^4}\,(\kappa^2\,\delta_{ij} - \kappa_i\kappa_j)$$

Thus

$$F_{11}^{\ 1}(\kappa_1) = \iint\limits_{-\infty}^{\infty}\phi_{11}(\underset{\sim}{\kappa})\,d\kappa_2\,d\kappa_3$$

$$= \iint\limits_{-\infty}^{\infty}\frac{E(\kappa)}{4\pi\kappa^4}\,(\kappa^2 - \kappa_1^{\ 2})\,d\kappa_2\,d\kappa_3$$

By considering a transformation to polar co-ordinates in the κ_2, κ_3 plane, the integral can be expressed as

$$F_{11}^{\ 1}(\kappa_1) = \frac{1}{2} \int_{\rho=0}^{\infty} \frac{E(\kappa)}{\kappa^4} \rho^2 \rho \, d\rho$$

where

$$\rho^2 = \kappa_2^{\ 2} + \kappa_3^{\ 2} = \kappa^2 - \kappa_1^{\ 2}$$

Transforming to κ space by noting that in the κ_2, κ_3 plane, $\rho \, d\rho = \kappa \, d\kappa$; we have

$$F_{11}^{\ 1}(\kappa_1) = \frac{1}{2} \int_{\kappa_1}^{\infty} \frac{E(\kappa)}{\kappa^3} (\kappa^2 - \kappa_1^{\ 2}) \, d\kappa \qquad (9.2.1)$$

A function of κ alone, when differentiated by κ_1, will be an exact differential inside the integral, and since $E(\kappa)$ is bounded

$$\frac{\partial F_{11}^{\ 1}(\kappa_1)}{\partial \kappa_1} = -\kappa_1 \int_{-\kappa_1}^{\infty} \frac{E(\kappa)}{3} \, d\kappa$$

$$\frac{\partial}{\partial \kappa_1} \left(\frac{1}{\kappa_1} \frac{\partial F_{11}^{\ 1}}{\partial \kappa} \right) = \frac{E(\kappa_1)}{\kappa_1^{\ 3}} \qquad (9.2.2)$$

or finally

$$E(\kappa) = \kappa^3 \frac{\partial}{\partial \kappa} \left(\frac{1}{\kappa} \frac{\partial F_{11}^{\ 1}}{\partial \kappa} \right) \qquad (9.2.3)$$

(Batchelor, 1953)

Similarly, it can be shown

$$F_{11}^{\ 2} = F_{22}^{\ 1} = \frac{1}{2} \left(F_{11}^{\ 1} - \kappa \frac{\partial}{\partial \kappa} F_{11}^{\ 1} \right) \qquad (9.2.4)$$

A few comments on the development so far are in order:

(1)   The correlation tensor from which the energy spectrum is calculated is a function of three space variables and is consequently difficult to measure.

(2) The one-dimensional correlation tensor is easier to measure
but is still a function of space at a given instant in time.

(3) While the energy spectrum vanishes at zero wave number, the
one-dimensional spectra do not, since integrating over a
plane of wave-number space destroys directional information
and treats, for instance, a disturbance of high wave number
impinging on the surface obliquely the same as a disturbance
of lower wave number propagating parallel to the surface.
(Tennekes and Lumley, 1972, refer to this as aliasing, al-
though it should not be confused with instrumental aliasing.)

(4) No simple relationship between the energy spectrum and a
one-dimensional spectrum exists except under the rather re-
strictive assumption of isotropy. There is little reason to
assume that the turbulent field is isotropic at low wave-
numbers.

To carry our treatment further then, we have to make assumptions about
the shape of the spectrum, particularly at higher wave numbers, and also re-
late our time-series measurements to spatial correlations.

9.2.3 Universal Equilibrium and the Inertial Subrange

A large body of experimental evidence suggests that the basic mechanism of turbulence, i.e., the transfer of kinetic energy of the mean flow to internal energy of the fluid, depends only on two processes: the production of energy via non-linear inertial transfer at large scales and the viscous dissipation of energy at small scales. As the Reynolds number of a particular flow increases, the disparity in scales increases and if the Reynolds number is high enough the energy dissipation is found to be proportional to u^3/ℓ where u and ℓ are velocity and length scales characterizing the large features of the flow (Tennekes and Lumley, 1972). In other words, at sufficiently high Reynolds number, changing the viscosity, ν, will not alter the gross features of a turbulent flow. This, of course, is implicit in neglecting the viscous stress term compared to the Reynolds stress term in the equations of motion.

The wide separation of energy input and dissipation scales has another important consequence best expressed in the wave-number domain: as wave-number increases the degrees of freedom of the dynamical system increase and order imposed at large scales is decreased. Thus at high enough Reynolds number the range of the spectrum in which dissipation occurs is locally isotropic and depends only on the viscosity, ν, and the energy dissipation rate, ε (Kolmogorof, 1941; see Batchelor, 1953). Length and velocity scales, called Kolmogoroff microscales, can be defined from ν and ε such that $\eta = \nu^{3/4}\varepsilon^{-1/4}$ is a length scale and $v = (\nu\varepsilon)^{1/4}$ is a velocity scale. By dimensional arguments, the dimensionless parameter $E(\kappa)/v^2\eta$ is a universal function, E_{ε}, of another dimensionless group $\eta\kappa$:

$$E(\kappa) = v^2 \eta \, E_e(\kappa\eta) \tag{9.2.5}$$

Thus the spectrum of a turbulent flow in the equilibrium range has a universal description when scaled by the Kolmogoroff microscales, η and v.

As the gross Reynolds number of a particular flow increases, the dissipation range shifts toward higher wave-numbers. The possibility then exists of a region in which universal equilibrium is achieved but in which the effects of viscosity are not significant. Such a region is called the inertial subrange, where energy is "cascaded" from lower to higher wave-numbers with very little interaction between the turbulent flow and the mean-flow forces (production) on the one hand, or between the turbulent flow and molecular forces (dissipation) on the other.

In the inertial subrange the energy spectrum has a simple expression since $\partial E / \partial v = 0$. Let $\zeta = \kappa\eta$, differentiate (9.2.5), and rearrange,

$$\frac{\partial E_e}{E_e} = -\frac{5}{3} \frac{\partial \zeta}{\zeta}$$

$$E_e = \alpha \zeta^{-5/3}$$

$$E(\kappa, t) = \alpha \varepsilon^{2/3} \kappa^{-5/3} \tag{9.2.6}$$

(Batchelor, 1953)

The corresponding longitudinal one-dimensional spectrum can be found by integrating Equation (9.2.1)

$$F_{11}{}^1(\kappa) = \alpha_1 \varepsilon^{2/3} \kappa^{-5/3} \tag{9.2.7}$$

Similarly, the vertical and lateral one-dimensional spectra are found from Equation (9.2.4) to be

$$F_{33}{}^1(\kappa) = F_{22}{}^1(\kappa) = \frac{4}{3} F_{11}{}^1(\kappa) \tag{9.2.8}$$

The concept of local homogeneity can be introduced in a manner analogous to that of local isotropy. Thus, given a high enough Reynolds number, any turbulent flow can be considered homogeneous and isotropic at small scales. Furthermore, if an inertial subrange exists in the flow, it can be identified from simple criteria: namely, the minus five-thirds power law and the four-thirds ratio of cross-stream to longitudinal spectral amplitudes (Busch, et al., 1968).

9.2.4 Taylor's Hypothesis

It was postulated by G. I. Taylor that if the mean stream velocity in a stationary, homogeneous flow is large compared to the downstream root-mean-square turbulent velocity, the spatial structure of the turbulent field can be considered frozen and advected past a fixed observer at the mean stream speed.

The hypothesis can be extended by making the transformation $x = Ut$ and treating the time autocorrelations as one-dimensional space actocorrelations (Lumley and Panofsky, 1964).

Taylor's hypothesis furnishes a basis for the assumption that we can regard our triplets as probes being dragged through a turbulent flow field measuring that field as a function of space.

Lumley and Panofsky (1964) suggest that near the ground Taylor's hypothesis is valid for $\overline{u^2} \div U^2 \sim 1/9$ provided lag distances in the atmosphere are less than 90 m. At 2 m from the ice, we found typical ratios of $\overline{u^2}/U^2 \sim 1/100$ indicating that the hypothesis is justified, particularly for wave numbers characterizing the inertial subrange.

9.3 Instrumental Aliasing

Suppose that for a given instant in time along a particular spatial direction there exists a continuous function of position, $f(x)$, e.g., the autocovariance of the downstream velocity component. Suppose further that this function is sampled at length intervals L. The measured function, $f_s(x)$ is the product of the actual function and the so-called Dirac comb,

$$f_s(x) = f(x) \sum_{j=-\infty}^{\infty} \delta(x - jL)$$

or

$$f_x(x) = \sum_{j=-\infty}^{\infty} f(jL)\delta(x - jL)$$

The function $\delta_L(x) = \sum_{j=-\infty}^{\infty} \delta(x - jL)$ is periodic and can easily be shown to have the Fourier transform

$$\mathscr{F}\{\delta_L(x)\} = k_o \delta_{k_o}(k) = k_o \sum_{n=-\infty}^{\infty} \delta(k - nk_o)$$

(Hsu, 1967, Chapter 5) where $k_o = 1/L$. Multiplication in the spatial domain corresponds to convolution in the wave-number domain, so

$$F_s(k) = \mathscr{F}\{f_s(x)\} = \frac{1}{L} \sum_{n=-\infty}^{\infty} F(k) * \delta(k-nk_o)$$

that is, $F_s(k)$, the transform of the measured function, is made up of the kth component of the true transform plus components at $k+k_o$, $k+2k_o$, etc. It is apparent that if there are no components of $F(k)$, the true transform, for $|k| > k_o/2$, then the measured transform will be the scaled true transform. Conversely, if components at $|k| > k_o/2$ exist, these components will be folded back on the measured transform, which is then said to have been aliased. The wave number $k_N = 1/2L$ is called the Nyquist wave number (or

Nyquist frequency in the frequency domain).

The problem of aliasing in geophysical measurements is inescapable,
but if it can be shown that the measurements are made to scales small enough
that from our knowledge of the physical processes involved we know higher
wave-number compoenets are small, the measured transform will very nearly
reproduce the actual transform.

As related to our measurements, if we can show that we have measured
at small enough scales so that turbulent energy in higher wave numbers can-
not much affect the energy spectrum when aliased to lower wave numbers, then
we can say we have measured the turbulent flow field. In other words, we
need to show that we have measured well into the equilibrium range of the
energy spectrum so that disturbances of smaller scale cannot appreciably
alter the Reynolds stress tensor.

From the calibrations for head-on currents, the distance a current meter
travels for one complete revolution in still water is given by the formula
$\underline{d} = 7.4 + 1.1 \underline{t}$ in cm where $\underline{t}$ is the period for one revolution. In the
range of velocities encountered, the distance between samples is approxi-
mately 8 cm. This implies that if Taylor's hypothesis is valid, then turbu-
lent eddies with scales smaller than 8 cm will not be detected even by a
meter aligned into the flow. For a meter with its axis at some angle from
the streamline, the minimum sampling distance will be increased by the
factor sec (θ), where θ is the angle of attack. For a triplet aligned
in some arbitrary way with the average streamline, the minimum sampling
length is determined by the slowest-turning meter.

In the time series used to calculate spectra, the average of the slowest
component divided by the mean speed was about 1/3 to 1/4 corresponding to a

sampling length of 24 to 32 cm, or a Nyquist wave number of 1.6 to 2.1

m^{-1}. This argument would hold rigorously were the time series actually

discretely sampled. As J. Smith (personal communication) has pointed out,

the mechanical nature of the current meter used acts as an effective filter

for frequencies higher than its turning frequency. For this reason we do

not expect aliasing in the usual sense to be a problem; however, the argu-

ment is still effective for determining that part of the spectrum to which

we can measure, and the criteria outlined above are still valid.

9.4 Calculations

In practice, discrete Fourier transforms were calculated using a slight-ly modified version of the Data General Users Group fast Fourier transform routine supplied by Ron Stuttheit of Scripp's Institute of Oceanography. It transforms a maximum size array of 1024 points in about 1 sec. The fast Fourier transform is a high-speed algorithm for computing discrete trans-forms and its use has no effect on the properties of the discrete Fourier transform described in Appendix C.

Calculating spectra from discretely-sampled, finite length time series is an endeavor fraught with hazard. One of the more obvious problems is the fact that a finite realization of a time series assumed stochastic is actually the product of the infinite series with a rectangular data window, a function whose value is one for all measured times and zero for others. Since multiplication in the time domain implies convolution in frequency space, we see that our estimate of the spectrum is the true spectrum con-volved with the transform of the rectangular window. If the true spectrum is characterized by sharp peaks, this convolution will result in serious "leakage" of energy to other frequency components.

It is also true that although increasing the length of the time series being analyzed allows greater frequency resolution, it does not increase the quality of the spectral estimate (Jenkins and Watts, 1968).

Numerous methods exist for alleviating these problems and improving the spectral estimates. For instance, various tapered data windows have been suggested that have better frequency domain characteristics, i.e., they reduce leakage compared to the rectangular data window. It should be

pointed out however, that from the nature of turbulence, a very random sort

of phenomenon, we do not expect sharp peaks in its spectrum and do not

anticipate leakage to be a major problem; but, for the same reason, there

is apt to be a great deal of variance in the spectral estimates from one

realization to the next (a good example of this is given for white noise

in Chapter 6 of Jenkins and Watts, 1968).

In their classic paper on the subject, Blackman and Tukey (1958) sug-

gest calculating the autocovariance function from a time series for lags

up to some fraction of the total number of samples, weighting this function

by an empirical data window, then transforming to get the power spectral

density estimate. It should be emphasized that this technique pre-dated

the advent of fast algorithms for discrete transformation. Also, the

number of lags calculated in the autocorrelation series is usually 1/10 to

1/9 of the total number of samples, so that frequency resolution is decreased

considerably.

The fast Fourier transform algorithm has made the transformation of

many long time series feasible and allows greater flexibility in reducing

the variance in spectral estimates. Kanasewich (1973) suggests that, for

a long data set, dividing the series into I subsets and then calculating

the average energy density for each frequency is an excellent way to proceed.

The asymptotic variance (the expected variance of spectral estimates if the

spectrum were uniform or "white") should decrease as 1/I.

After several tests comparing the latter technique to the Blackman and

Tukey approach showed little significant difference, the direct transfor-

mation and multiplication approach was chosen for its relative simplicity.

The actual computation of spectra presented in the next sections was done following the steps outlined below:

(1) A time series of N points for each component is formed by block averaging the velocity data, usually in groups of 8 corresponding to a time step of 1.62 sec. N was usually 1024 although it could be divided by multiples of two.

(2) An average streamline reference frame is determined by rotating out the average V and W components. Each point vector in the series is rotated into this frame and the mean speed, U, is removed from the resulting u component, leaving three series of fluctuating components: downstream, u; lateral, v; vertical, w, all with zero mean.

(3) Each series is transformed and the spectral estimate, $S(n)$, is calculated by taking the absolute square.

(4) Each spectral estimate is multiplied by its index, n, and classified according to the log of its dimensionless wave number, $\kappa z = nz/N\, \Delta t\, U$.

(5) Several runs are accumulated, averaged and plotted $\log[nS_\alpha(n)/\sigma_\alpha^2]$ vs. $\log \kappa z$, $\alpha = u, v, w$.

By using the weighted spectral estimate $nS(n)$ rather than $S(n)$ the function loses its dependence on the particular units chosen for the frequency or wave-number axis. Also, it is a fairly standard representation for atmospheric turbulent spectra with which comparison to spectra measured above the surface layer can be made (e.g., Panofsky and Mazzola, 1971).

9.5 Results

In order to calculate averaged spectra the current record was searched for reasonably steady periods and from these, time series approximately 28 minutes long were chosen more or less at random. In all, thirty such series taken over the period Apr. 11 through Apr. 13 were analyzed and combined in the manner described in the preceding section. Figures (9-1) through (9-3) show the results of this procedure. For small wave numbers the number of samples was comparatively small resulting in fairly large variance; a smooth line was drawn by eye to estimate the spectrum. This was usually limited to wave-number ranges below the peak in the w-spectrum. An example of an untouched computer plot for the u-spectrum corresponding to Figure (9-1) is shown in Figure (9-4). Because the spectrum in Figure (9-4) has been scaled by the variance, the vertical axis is offset from that in Figure (9-1) although the shape of the curve remains the same (this was one reason for using a log plot for the weighted spectrum rather than the "area-preserving" plot). ·

We can use the spectra in Figure (9-1) to investigate the effect of instrumental filtering. In Section (9.3) we set a lower limit on the Nyquist wave number at about 1.6 m^{-1}. At 2 m, this corresponds to a dimensionless wave number of 3.2 which places us somewhere near the right edge of the graphs (the reason for this is that we block-averaged eight samples). When we consider that the weighted spectrum, $nS(n)$, falls off much slower than the true spectrum, the fact that the weighted u-spectrum has fallen off by a decade and a half confirms that aliasing of energy in wave numbers higher than the Nyquist wave number is negligible. From Figures (9-2) and

(9-3) it is clear that the dimensionless Nyquist wave number moves right-
ward with increasing depth faster than the spectra do, and we conclude that
the triplet at 2 m is the critical case. Thus the first question posed
for spectral analysis is answered: the response of our data-collection
system is sufficiently fast to measure the turbulent flow field.

Some other observations can be made about the spectra in Figure (9-1).
They are qualitatively similar to atmospheric surface-layer spectra com-
piled by Busch and Panofsky (1968), particularly with respect to the peak
in the w-spectrum. However, as has been demonstrated elsewhere, 2 m is out
of the surface-layer and surface-layer scaling is not necessarily correct.
Also, the Reynolds number for flow beneath the ice is smaller than in the
atmosphere by probably a couple of orders of magnitude and we expect vis-
cosity to affect the spectrum at lower wave numbers.

For the triplet at 2 m there appears to be evidence for an inertial
subrange, i.e., there exists a short region in which all three spectra fall
off with a -2/3 slope and the ratio $S_w(n)/S_u(n) \sim \log^{-1}(.1) = 1.3$. At 4 m
and 8 m regions of -2/3 slope appear in all the spectra but the v- and w-
spectra have generally the same magnitude as the u-spectrum.

We can calculate the dissipation rate, ε, from Equation (9.2.7):

$$\varepsilon = [\frac{F(\kappa) \, \kappa^{5/3}}{\alpha_1}]^{3/2}$$

Busch and Panofsky (1968) suggest a value for the constant, $\alpha_1 = .15$ and
using the values $kz = 1$, $kS(k) = .1$

$$\varepsilon = 2.7 \times 10^{-3} \, cm^2\text{-}sec^{-3}$$

We can estimate the shear production of turbulent energy as

$$- \overline{uw} \frac{\partial U}{\partial z} \sim \overline{uw} \frac{u_*}{kz}$$

with average values from Apr. 11 and Apr. 12. This is approximately

$$\mathcal{P} = 6 \times 10^{-3} \text{ cm}^2\text{-sec}^{-3}$$

This is a crude calculation that depends on the log profile to estimate the slope and uses an estimate of stress conditions for the time that spectra are actually calculated, but nevertheless the results seem to indicate that production is significantly larger than dissipation. This may not be too surprising in light of the flattening of the $\overline{uw}$ stress profile discussed in Section (8.1). We would expect the same mechanism to act as a sink for turbulent energy, in much the same way as a stably stratified medium extracts energy from a turbulent flow.

9.6 Vertical Spectra

Figure (9-5) shows average normalized vertical spectra obtained by averaging spectra from 30 different time series and smoothing the resulting average by eye in the lower wave numbers. The abscissa is the non-dimensional wave number, kz, where k is the wave number determined from the mean velocity using Taylor's hypothesis. The most notable feature is the rightward shift of the spectra with increasing depth. The spectrum of vertical velocity at 32 m appears to be different from the others; this may be due to diffusion of effects taking place in the pycnocline such as internal waves.

Measurement of vertical spectra are fairly common for the surface layer of the atmosphere and are usually presented in a form similar to that shown. The peak of the spectrum is taken to be the characteristic wave number $k_m = 1/\lambda_m$ where λ_m is the length scale of eddies that transfer energy from the mean flow to the turbulence. If an inertial subrange exists, then in it the spectrum should fall off as $k^{-5/3}$ or with a -2/3 slope in the representation shown.

Surface-layer similarity theory predicts that the peak in the w-spectrum should scale with the distance from the boundary and thus the spectrum should depend only on the non-dimensional wave number and the stability parameter, z/L (Busch, et al., 1968). Busch and Panofsky (1968) found that in the atmospheric surface layer under neutral or unstable conditions, the vertical spectra from different levels at three sites coincided with a peak at non-dimensional wave number kz ~ .4. Under stable conditions the spectrum retains its shape but is shifted toward higher wave number since gravity

tends to limit the size of energy-carrying eddies in the vertical.

Away from the surface layer, the effect of the boundary on eddy sizes should become less and less important. Presumably a maximum scale size is reached at some distance from the boundary beyond which we would expect spectral peaks to shift toward higher dimensionless wave number. This is confirmed by our observations and also from observations in the atmosphere from towers and airplanes (e.g., Panofsky and Mazzola, 1971).

9.7 Inferred Mixing Length and K Distributions

The concept of eddy viscosity draws heavily from the idea of a characteristic length scale for turbulent momentum transfer that allows the turbulent stress to be related to the mean velocity shear. Thus $-\overline{uw} = K \frac{\partial U}{\partial z}$, where K, the eddy viscosity, has dimensions $L^2 T^{-1}$ and is proportional to a characteristic velocity times a characteristic length by analogy to the molecular viscosity of an ideal gas.

In the neutral atmospheric surface layer the dimensionless wind shear $\phi_m = \frac{kz}{u_*} \frac{\partial U}{\partial z}$ is equal to 1.0 provided von Karman's constant is .35 (Businger, et al., 1971). Thus K is identified as proportional to the friction velocity times the distance from the surface. But since the ratio z/λ_m is also constant, K is proportional to u_* times λ_m, an even more fundamental relationship in terms of mixing-length theory.

For the outer boundary layer, K-theory is on shakier footing. As described earlier, various K models have been proposed that can yield credible results, but without placing such emphasis on the physical meaning of a mixing length. Deardorff's (1972) results indicate that for the unstable case, K passes through $\pm \infty$ and becomes negative: taxing to the imagination if thought of in terms of a mixing length.

It would be interesting, however, to investigate the relationship between K and the vertical spectral peaks in the neutral or slightly stable outer layer, since wavelengths associated with the peaks suggest a scale length for the outer region. We postulate that $K = c_1 u_* \lambda_m$, and use surface layer arguments to evaluate c_1 from measurements at 2 m, since we expect the log profile to be valid there (Tennekes, 1973).

$$K = \overline{-uw} \frac{kz}{u_*}$$

$$c_1 = \frac{\overline{-uw}\ kz}{u_*^2 \lambda_m}$$

in the log profile region only.

From the spectra in Figure (9-5) it is evident that in some cases a "peak" is hard to identify. In most of the curves, though, a region where the spectrum falls off with a -2/3 slope can be found, so it is reasoned that choosing the point where the spectrum first matches a straight chord with -2/3 slope would provide a consistent estimate of the characteristic wave number for the energy-producing eddies. Obviously, this entails some subjectivity on the part of the observer and should be considered as an order-of-magnitude estimate only.

The calculations described were carried out and are summarized in the following table. Typical measurements at 2 m were used to evaluate c_1 = .1.

Depth	$\log z/\lambda_m$	λ_m(m)	fz/u_*	Kf/u_*^2
2	-.30	4.0	.03	5.9×10^{-3}
4	-.07	4.7	.06	6.9×10^{-3}
8	-.03	8.6	.11	12.6×10^{-3}
12	+.18	7.9	.17	11.6×10^{-3}
16	+.33	7.5	.22	11.0×10^{-3}
20	+.30	10.0	.28	14.7×10^{-3}
26	+.83	3.9	.37	5.7×10^{-3}
32	+1.52	1.0	.45	1.5×10^{-3}

Table 9-1

K-distribution Calculations

These values are plotted in Figure (9-6) along with curves from Dear-dorff (1972) and Businger and Arya (1974) for two stability classes, neutral and slightly stable.

For comparison, an eddy viscosity can be calculated from simple Ekman theory by equating the Ekman depth with the depth of the mixed layer (Hunkins, 1966). Solving for K when $z = 32$ m $= \pi \sqrt{2K/f}$ we get $K = 70$ cm^2-sec^{-1}. We can non-dimensionalize this to get $fK/u_* = .01$, which fits in fairly well with the values shown.

It should be reiterated that the result shown in Figure (9-7) is not derived from the mean current profile, but rather from vertical velocity spectra. As we have indicated previously, the lateral velocity profile cannot be described as a balance between the Reynolds stress gradient and the Coriolis force. Clearly, under these conditions the Reynolds stress cannot be related simply to the mean profile gradient becasue a large portion of the V component balances the form-drag force, F_x. An interesting feature of this exercise is that although the measured $\overline{uw}$ profile behaves as if it were in a stable environment, (see Fig. 8-3), the eddy viscosity associated with peaks in the w-spectra is closer to what we would expect in a neutrally stable column. Thus the arguments of Section (8.1) wherein we argued that the flattening of the $\overline{uw}$ profile was due to the form-drag force, F_x, are bolstered by the results of this section.
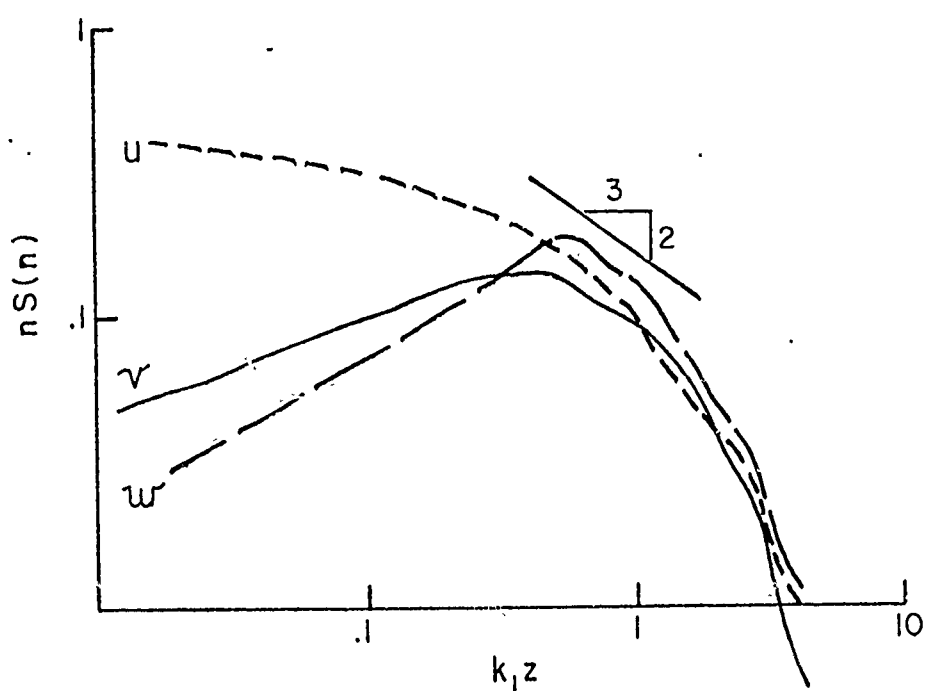
Fig. 9-1 Averaged and smoothed weighted spectra of downstream, u, cross-stream, v, and vertical, w, velocity components for Triplet 1, 2 m below ice
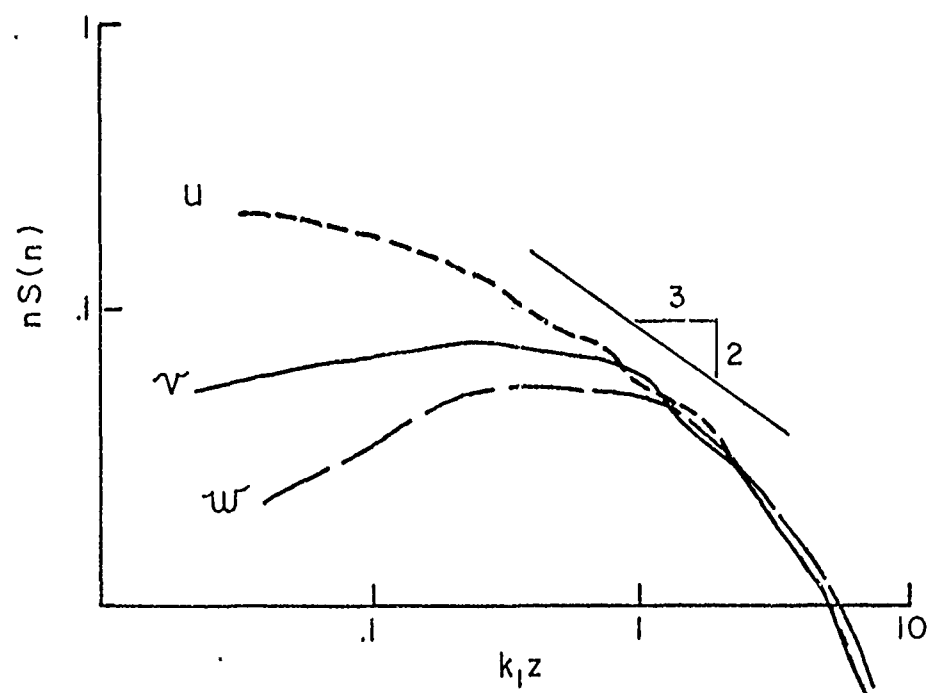
Fig. 9-2 Averaged and smoothed weighted spectra for Triplet 2,
4 m below ice
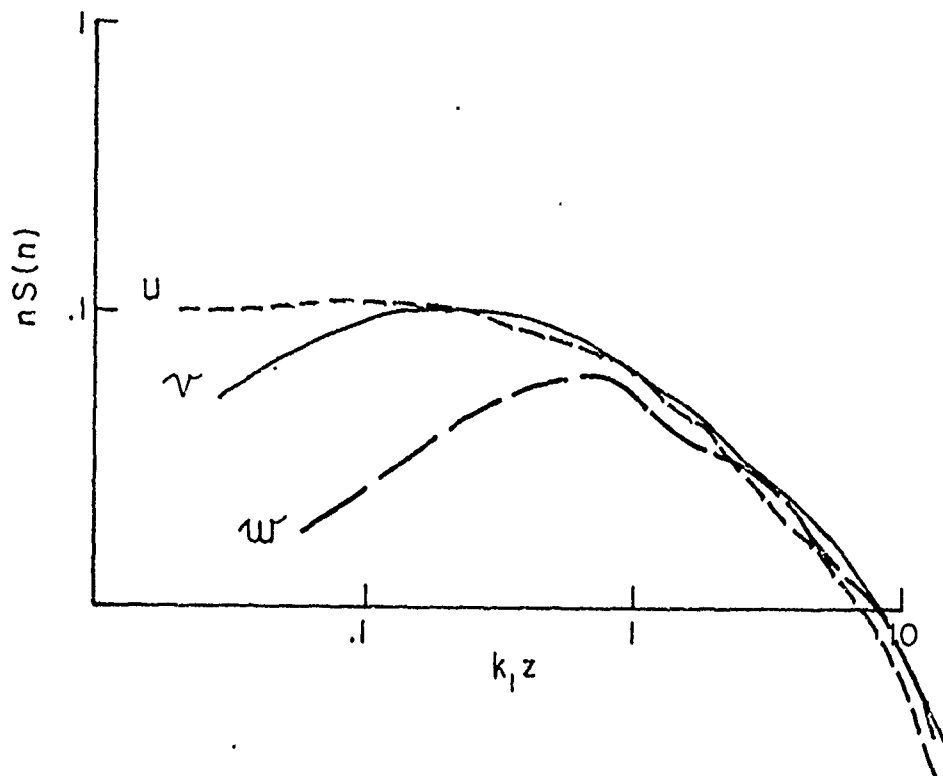
Fig. 9-3 Averaged and smoothed weighted spectra for Triplet 3,
8 m below ice
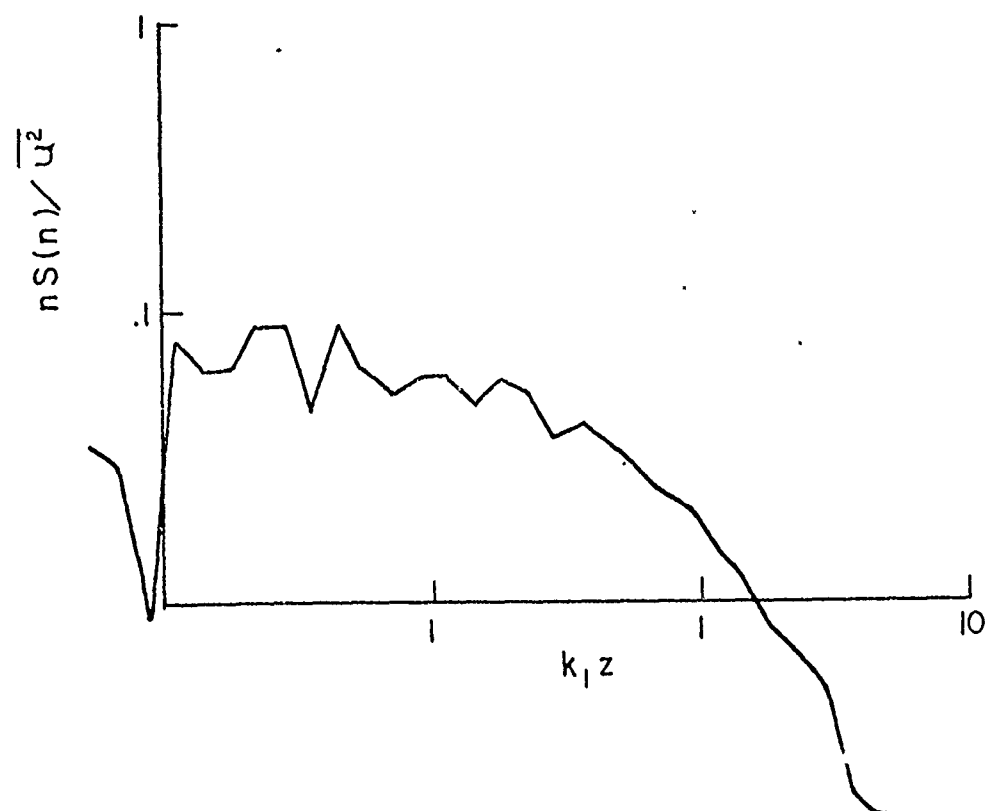
Fig. 9-4 Normalized average weighted u spectrum corresponding
to Fig. 9-1 without visual smoothing
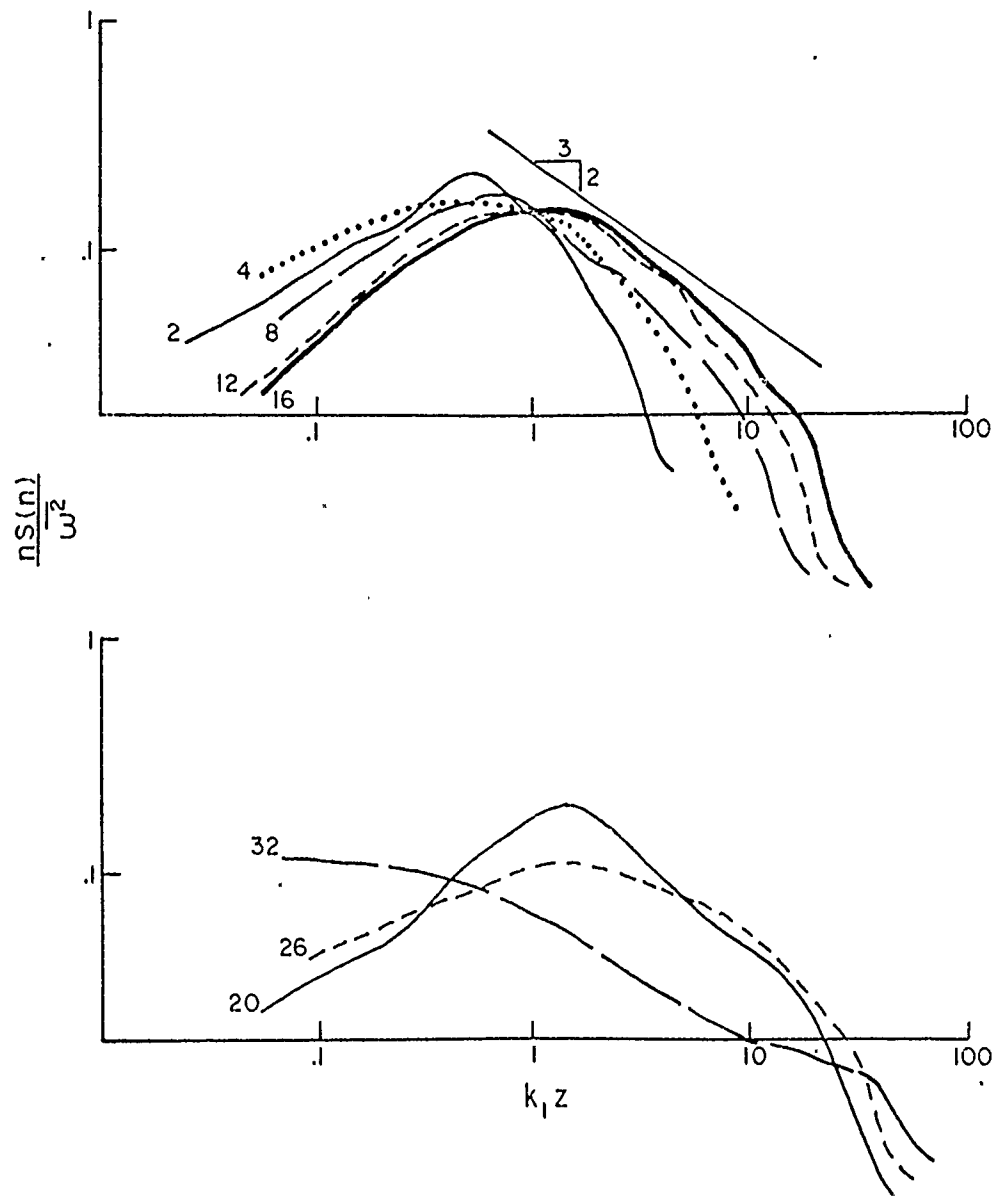
Fig. 9-5 Normalized averaged and smoothed vertical weighted spectra at 8 levels. Numbers are depths in meters.
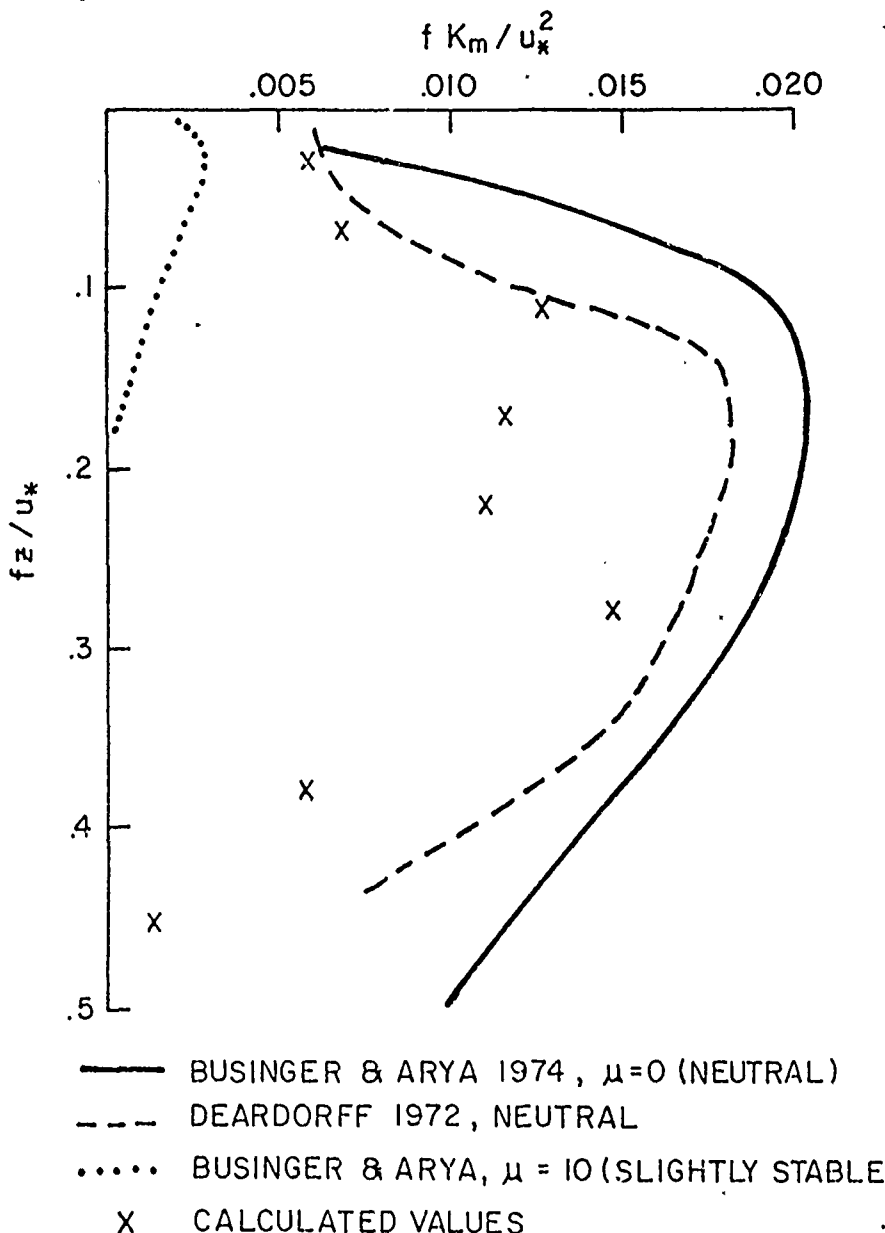
Fig. 9-6 Distribution of dimensionless eddy viscosity

10   SUB-MIXED-LAYER BAROCLINIC CURRENTS

10.1   Background

It has been mentioned previously that the triplets located within the pycnocline showed the existence of many more transient current phenomena than those located toward the base of the mixed layer.

Probably to a large extent these could be attributed to internal waves propagating along the steep density gradient. It was recognized that our data could provide some information about the nature of these waves, but that a rigorous investigation of them was beyond the scope of this particular project.

On the other hand, it became apparent that other, larger-scale phenomena were also present that could account for considerable mass transport. In fact, toward the latter part of the storm on Apr. 14, as currents were falling off to threshold in the mixed layer, we observed currents in the pycnocline that persisted for more than a day and that were nearly comparably to the maximum ice-drift velocity.

10.2 Time Development of the Density Structure

Figure (10-1) is a plot of isopycnals (lines of constant density) vs. time for the period Apr. 6 to Apr. 15, and below that a plot of the average density of the water column above 60 m expressed in σ_t units. In each case, the graphs were made from daily average σ_t plots of which Figures (4-2) and (4-3) are examples.

If the isopycnals and isobars (lines of constant pressure) in a flow are parallel the flow is said to be barotropic, while if they intersect the flow is termed baroclinic. Since depth and pressure surfaces closely coincide in the ocean, the structure of the pycnocline is baroclinic over the time scale of the storm.

In general, as winds and ice motion increased from Apr. 10 through Apr. 12, the mixed layer deepened and became slightly denser while at a given level in the upper pycnocline the density decreased significantly. On Apr. 13 the trend began to reverse and on Apr. 14 a sharp change occurred with large increases in density in the upper pycnocline and freshening of the mixed layer.

The average density above 60 m is plotted to show that while at a particular level in the pycnocline that the density might change by as much as .15 σ_t units over the development of the storm, the density of the whole column above that level was roughly conserved, at least until Apr. 14.

Figure (10-2) from Hunkins (1974a) STD measurements at the AIDJEX site provides a better overall view. Here isohalines are drawn instead of isopycnals but the density structure follows salinity quite closely. Also, times are shown in Greenwich Mean Time which leads Alaska Std. Time by ten

hours, so that, for instance, 1200 GMT is 0200 AST on the same date. The

plot has been modified to include barometric pressure.

Figure (10-3) shows in greater detail the density structure over a

nine-hour period beginning at about 0900 on Apr. 14 (AST). The isopycnals

in the upper pycnocline slope quite sharply and steadily upward, while

below 45-50 m the slope is opposite. Figure (10-4) shows two casts, one

toward the start of the period, one toward the end.

10.3 Baroclinicity and Geostrophic Shear

Baroclinic conditions require geostrophic shear, a fact that can be demonstrated by differentiating the geostrophic balance equation, i.e.

$$f \, v_g = \frac{1}{\rho} \frac{\partial p}{\partial x}$$

$$f \frac{\partial v_g}{\partial z} = \frac{1}{\rho} \frac{\partial}{\partial z} \left(\frac{\partial p}{\partial x} \right) + \frac{\partial p}{\partial x} \frac{\partial}{\partial z} \left(\frac{1}{\rho} \right)$$

$$= \frac{-g}{\rho} \frac{\partial \rho}{\partial x} - \frac{1}{\rho^2} \frac{\partial p}{\partial x} \frac{\partial \rho}{\partial z} \qquad (10.3.1)$$

where we have used the hydrostatic relation

$$\frac{\partial p}{\partial z} = -\rho g$$

That the last term in Equation (10.3.1) is small can be seen by considering a case in which $\partial \rho / \partial x = 0$. Then

$$\frac{\partial v_g}{\partial z} = \frac{-1}{\rho} v_g \frac{\partial \rho}{\partial z}$$

or

$$\left| \frac{\Delta v_g}{v_g} \right| = \left| \frac{\Delta \rho}{\rho} \right|$$

and we see that to create a change in geostrophic current of the same order as the original would require an enormous density gradient so we can say

$$\frac{\partial v_g}{\partial z} \doteq \frac{-g}{\rho f} \frac{\partial \rho}{\partial x} \qquad (10.3.2)$$

10.4 Calculations and Measurements

In order to estimate the geostrophic shear (called thermal wind in the atmosphere) associated with the horizontal density gradients depicted in Figures (10-3) and (10-4) we can try as a first guess a length scale associated with our westward ice drift and calculate the expected north-south currents. In other words, we determine $\Delta\rho$ from the density casts and an advective length scale for the distance between casts, and use these values for a finite-difference integration of the thermal wind equation, (10.3.2). These calculations are summarized in Table (10-1).

Figure (10-5) shows the actual north-south currents observed using the mean current at 32 m as the subtracted reference. In these plots the velocities have been filtered with a twenty-minute running average to remove internal waves of shorter period. Considering the crudeness of our treatment in arriving at the velocity values in Table (10-1), the correspondence with measurements is remarkable.

Although it is not clear from the plots, prior to about 0900 the isopycnals were relatively flat, so that the time development of the currents in Figure (10-6) is illustrative of the response time for this sort of forcing. It apparently takes on the order of three hours for currents as high as 14 cm-sec^{-1} to respond geostrophically to their forcing mechanisms at this latitude.

At other times sub-mixed-layer currents were observed although none were as striking as those occuring on Apr. 14 and Apr. 15. A vector plot of the velocities at the four lowest triplets during the morning of Apr. 13 (Figure (10-7)) shows an extremely complicated structure to the velocity

field and presumably the density field. For instance, at 0330 a relatively strong south-west flow at 44 m has turned more than 90 degrees to southeast at 54 m.

10.5 Discussions and Conclusions

East-west currents during the period shown in Figure (10-6) were small. This, combined with the fact that we could use the advective length scale to calculate geostrophic velocities, suggests that the east-west motion of this disturbance was small and that it could be considered a front aligned predominantly in the north-south orientation. The origin of this front is not well understood, but the following heuristic explanation, which borrows heavily from Holton's treatment of synoptic-scale spin-down and associated secondary circulations in the atmosphere (Holton, 1972, Chapter 6), is offered as a possibility.

The idealized Ekman equations for an ocean with no barotropic pressure gradients can be written

$$f \, \vec{e}_z \times \vec{u} \; = \; \frac{1}{\rho} \frac{\partial}{\partial z} \vec{\tau}_n \tag{10.5.1}$$

where $\vec{e}_z$ is the vertical unit vector and $\vec{\tau}_n = \tau_{zx} \vec{e}_x + \tau_{zy} \vec{e}_y$ is the "stress vector."

If we define D_e as the depth at which stress vanishes (the depth of the Ekman layer) we can rearrange and integrate Equation (10.5.1)

$$- \int_{-D_e}^{0} \nabla_h \cdot \rho \, \vec{u} \, dz \; = \; \frac{1}{f} \vec{e}_z \times \vec{\tau}_0 \tag{10.5.2}$$

where $\vec{\tau}_0$ is the surface stress.

If we take the horizontal divergence of Equation (10.5.2) and apply some vector manipulation, we have

$$- \int_{-D_e}^{0} \nabla_h \cdot \rho \vec{u} \, dz \; = \; \frac{1}{f} \nabla_h \cdot (\vec{e}_z \times \vec{\tau}_0) \; = \; - \frac{1}{f} \vec{e}_z \cdot \nabla \times \vec{\tau}_0$$

From continuity

$$\rho \, \frac{\partial w}{\partial z} \; = \; -\nabla_h \cdot \rho \vec{u}$$

and if the surface vertical velocity is zero, this becomes

$$w_0 \; = \; \frac{1}{\rho f} \, \vec{e}_z \cdot \nabla \times \vec{\tau}_0$$

(C.B. Leovy, class notes)

Thus we have the result that the curl of the ice-stress field, which can be related to the vorticity of the ice-velocity field, is balanced by a vertical velocity at the base of the mixed layer.

In cyclonic motion about a low pressure area in the Northern hemisphere, the curl of the wind stress will be positive and can be estimated by $\Delta\tau/\Delta L$ where ΔL is the advective length scale. For the period Apr. 10 to Apr. 12, $\Delta\tau/\Delta L \sim 7 \times 10^{-7}$ giving $w_0 \sim 5 \times 10^{-3}$ cm-sec^{-1} upward.

Another way of viewing this is to recognize that there must exist a small upward flow at the base of the boundary layer to compensate for Ekman divergence in the boundary layer proper. Note that the "mirror image" analogy breaks down here. In the atmosphere, the Ekman transport is toward lower pressure, i.e. toward the center of the cyclone, while in the ocean it is directed away from the center.

If the fluid were neutrally buoyant, this upward flow would be balanced by a very small inward flow throughout the whole interior of the fluid.

In the actual case, vertical motions are inhibited in the strongly stable pycnocline and the return flow is confined to a relatively thin section near the base of the mixed layer.

If we visualize a cyclonic system suddenly imposed on a quiet ocean we might expect the following development. Ekman divergence beings imme-

diately, resulting in vertical transport of more dense material into the mixed layer. As the spin-up continues, the net influx of water typical of the top layers of the pycnocline toward the center of the system sets up horizontal density gradients. These gradients in turn cause secondary circulations that just balance vorticity at the base of the Ekman layer and bring the upward transport to a halt.

This was roughly the course of events observed during the storm. Early on there was a marked increase in mixed-layer density, but not much current activity in the pycnocline. As the storm matured the density build-up slowed and more currents were observed at depth. Finally, as winds and surface stress fell off and pressure reached a minimum on Apr. 14 (see Figure (10-2)) we were advected into a region characterized by an excess of water typical of the upper pycnocline and observed a strong baroclinic circulation. Clearly, the actual system is much more complicated than the simple picture presented here, but if the secondary circulations are a result of the vorticity balance mechanism, their energetics should be considered in modeling ice drag.

If we formulate a simple mixing problem it is possible to estimate the average density of water influxed by vortex pumping required to force the observed density change in the mixed layer. We assume that mixing is rapid and solve the resulting first-order differential equation to get

$$\rho_1 = \frac{\Delta\rho}{(1-e^{-wt/h})} + \rho_0$$

where ρ_0 is the original density,

            $\Delta\rho$ is the observed change,

            ρ_1 is the average density of introduced water,

            h is the depth of the mixed layer.

For the period Apr. 10 to Apr. 12, $\Delta\rho = .03$, wt/h = .3

$$\rho_1 = \frac{.03}{.26} + 24.05 = 24.17$$

This is typical of water at 35-40 m. Presumably the water that is transported vertically is replaced by fresher water flowing in along the base of the mixed layer to account for the decrease in density observed in the top layers of the pycnocline.

It is interesting to note that Hunkins observed a strong "eddy" with large vertical shears centered at around 100 m depth on Apr. 18 (Hunkins, 1974a). He argues that because the size scale corresponds to the Rossby radius of deformation and is much smaller than the synoptic scale of the storm, such eddies are spawned by baroclinic instability some distance off and are not directly related to the storm.

However, looking at Figure (10-2) and considering the arguments put forth above, it seems possible that the distortion near the top of the pycnocline observed on Apr. 14 through Apr. 17 might create such an instability. In fact, at a cursory glance, the presence of deep currents seems to be associated with calms following the passage of storms. As Hunkins points out, the kinetic energy associated with such phenomena is considerable and they should be the subject of more study.

Depth	$\Delta\rho$ ($\times 10^3$)	$\overline{\Delta\rho}$ ($\times 10^3$)	$-(g/\rho f)\Delta\rho/\Delta x$ ($\times 10^3$)	Δz (10^{-3})	Δv_g	v_g
25	.03					0
		.12	4.4	-.5	-2.2	
30	.21					-2.2
		.245	9.1	-.5	-4.6	
35	.28					-6.8
		.255	9.4	-.5	-4.7	
40	.23					-11.5
		.15	5.6	-.5	-2.8	
45	.07					-14.3
		.02	.7	-.5	-.3	
50	-.03					-14.6
		-.125	-4.6	-.8	3.7	
55	-.22					-10.9

$$\Delta t = 8 \text{ hrs} = 2.9 \times 10^4 \text{ sec}$$

$$\overline{u}_{ice} = 8.8 \cos 312 = -6.5 \text{ cm-sec}^{-1}$$

$$\Delta x = \overline{u}_{ice}\, t = -1.9 \times 10^5 \text{ cm}$$

Table 10-1 Geostrophic Shear Calculations
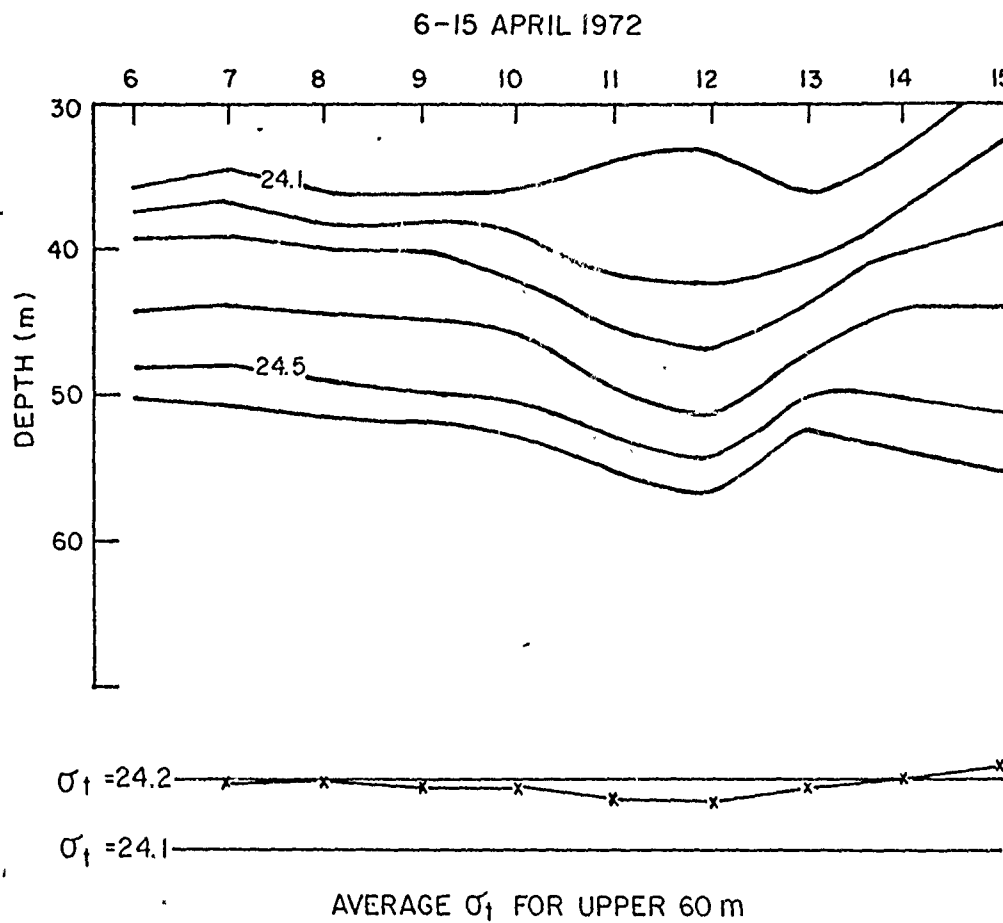
Fig. 10-1 Isopycnals (lines of constant density) vs. time in the
upper pycnocline
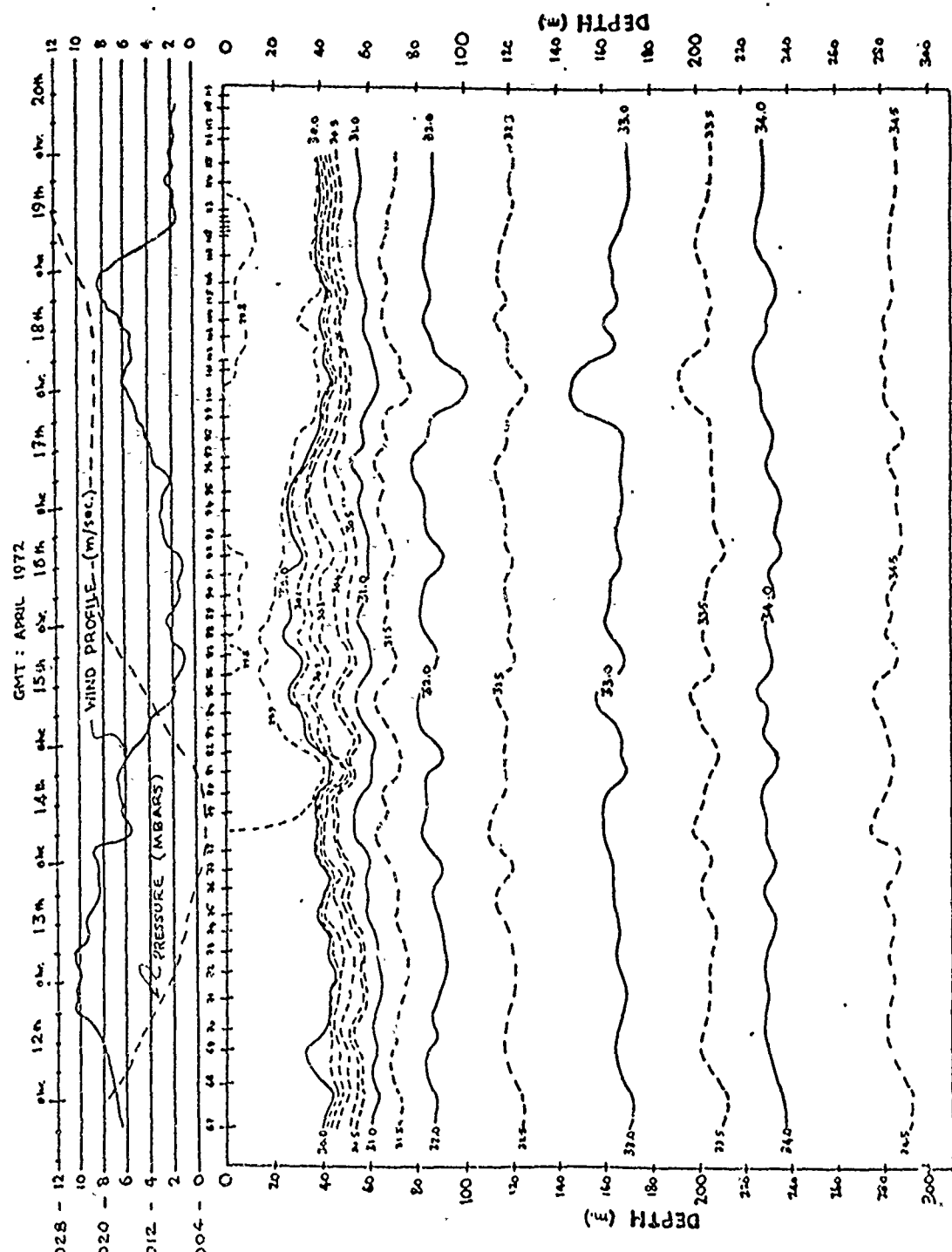
Fig. 10-2   Isohalines vs. time (adapted to include barometric
   pressure) from Hunkins (1974a)

14 APRIL 1972
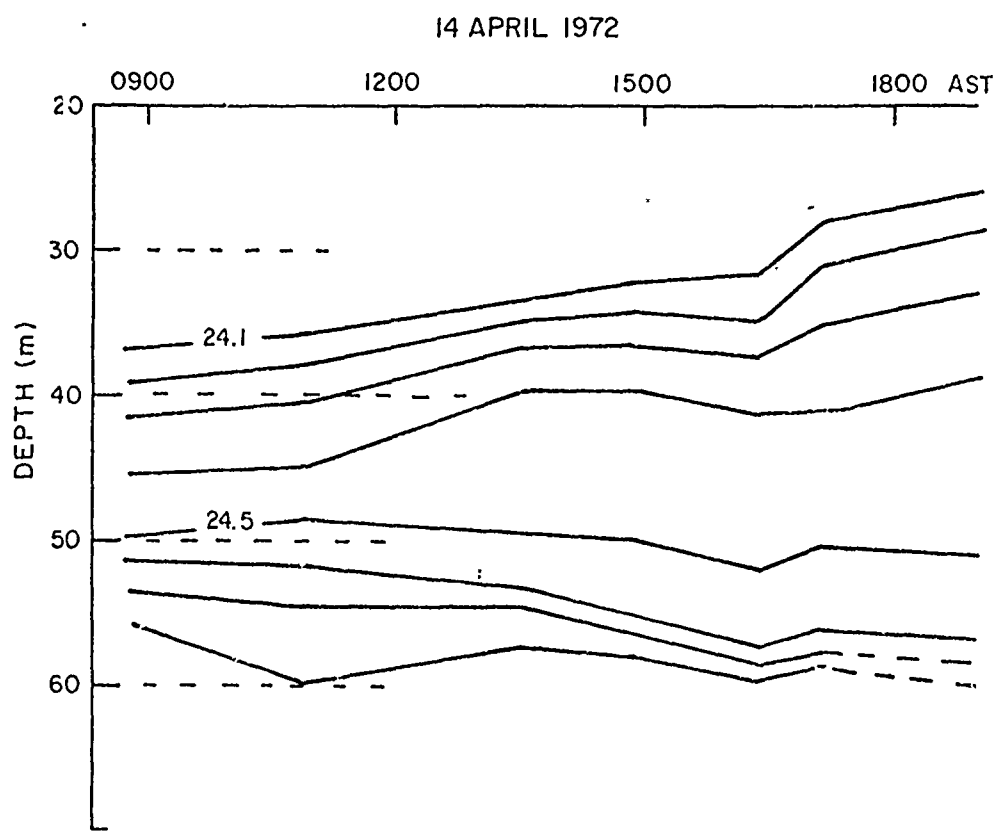
Fig. 10-3   Isopycnals vs. time showing steep density gradient
encountered on Apr. 14
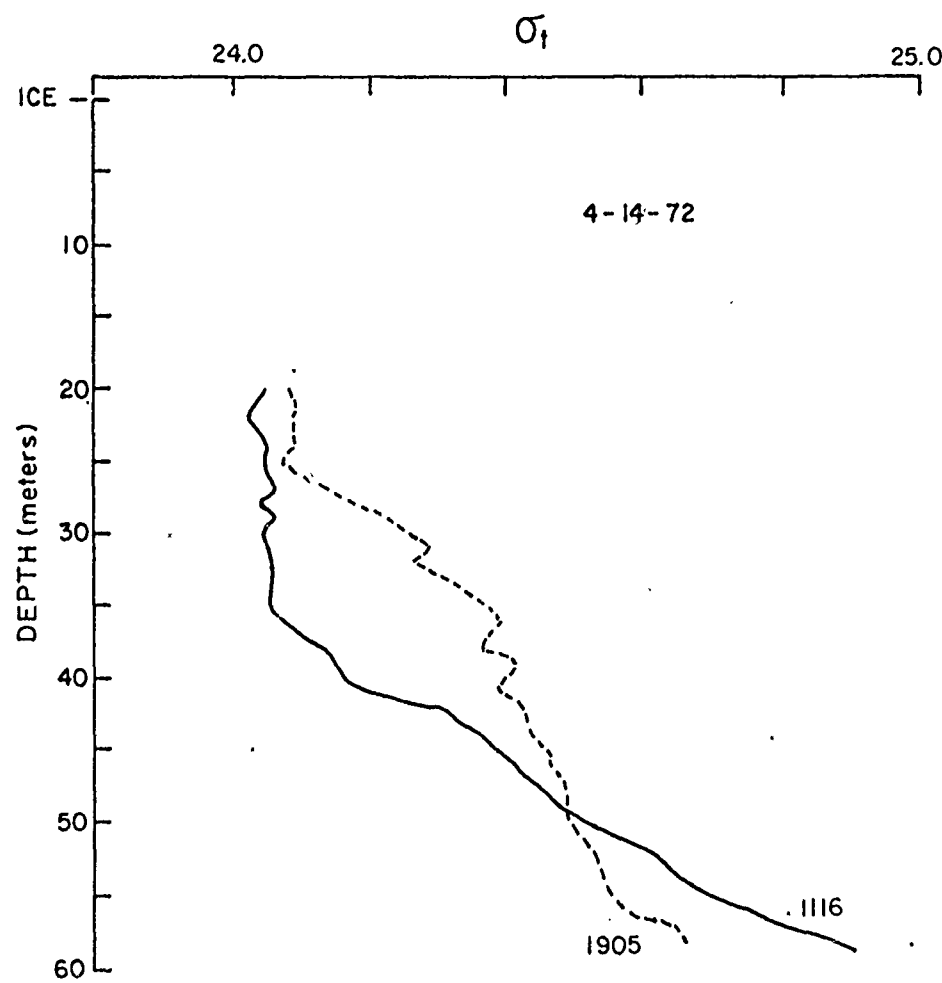
Fig. 10-4   Density profiles during the period of rapid change
depicted in Fig. 10-3
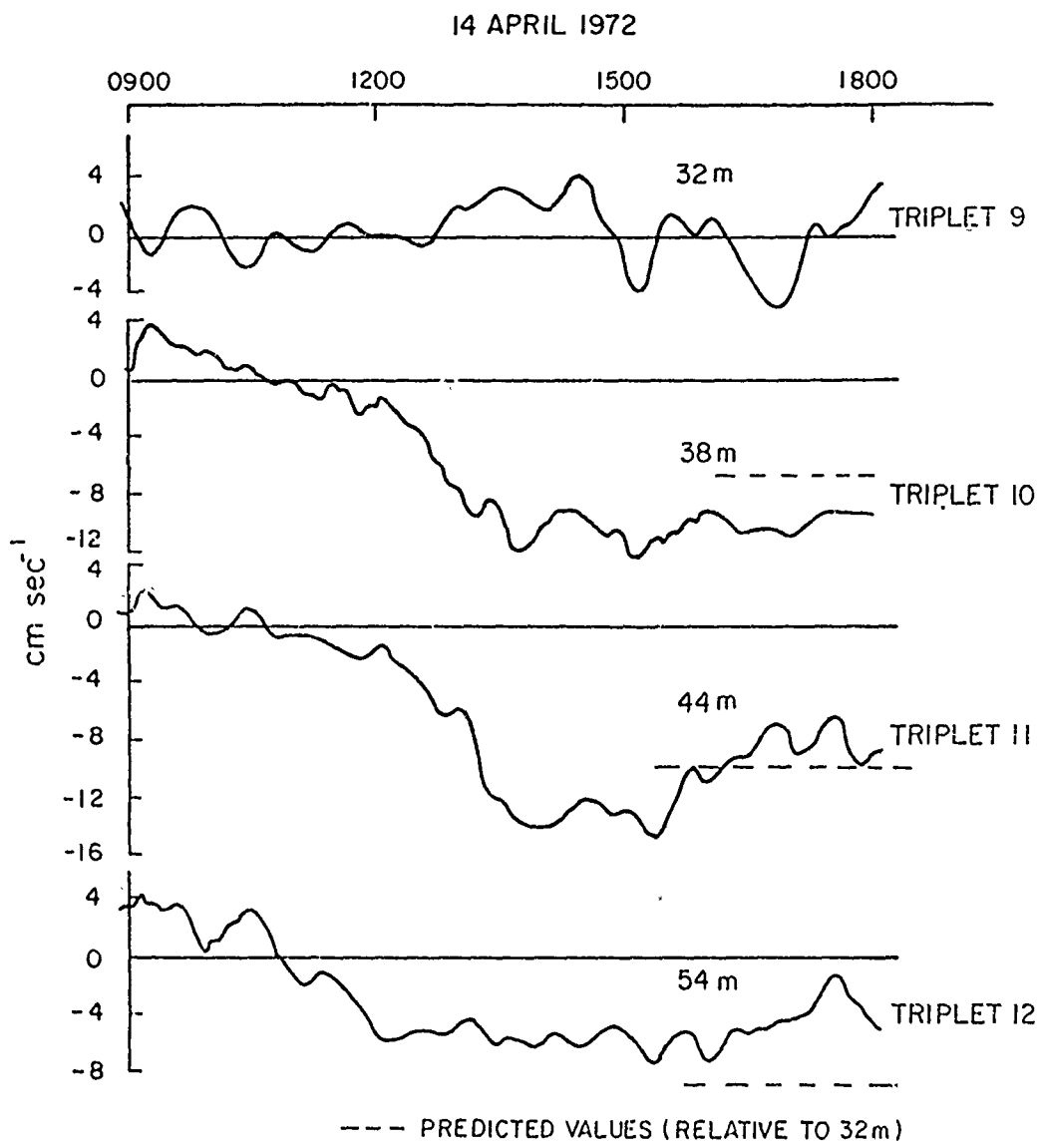
Fig. 10-5 North (positive)-south (negative) currents relative to the mean at 32 m showing geostrophic shear in response to density gradient
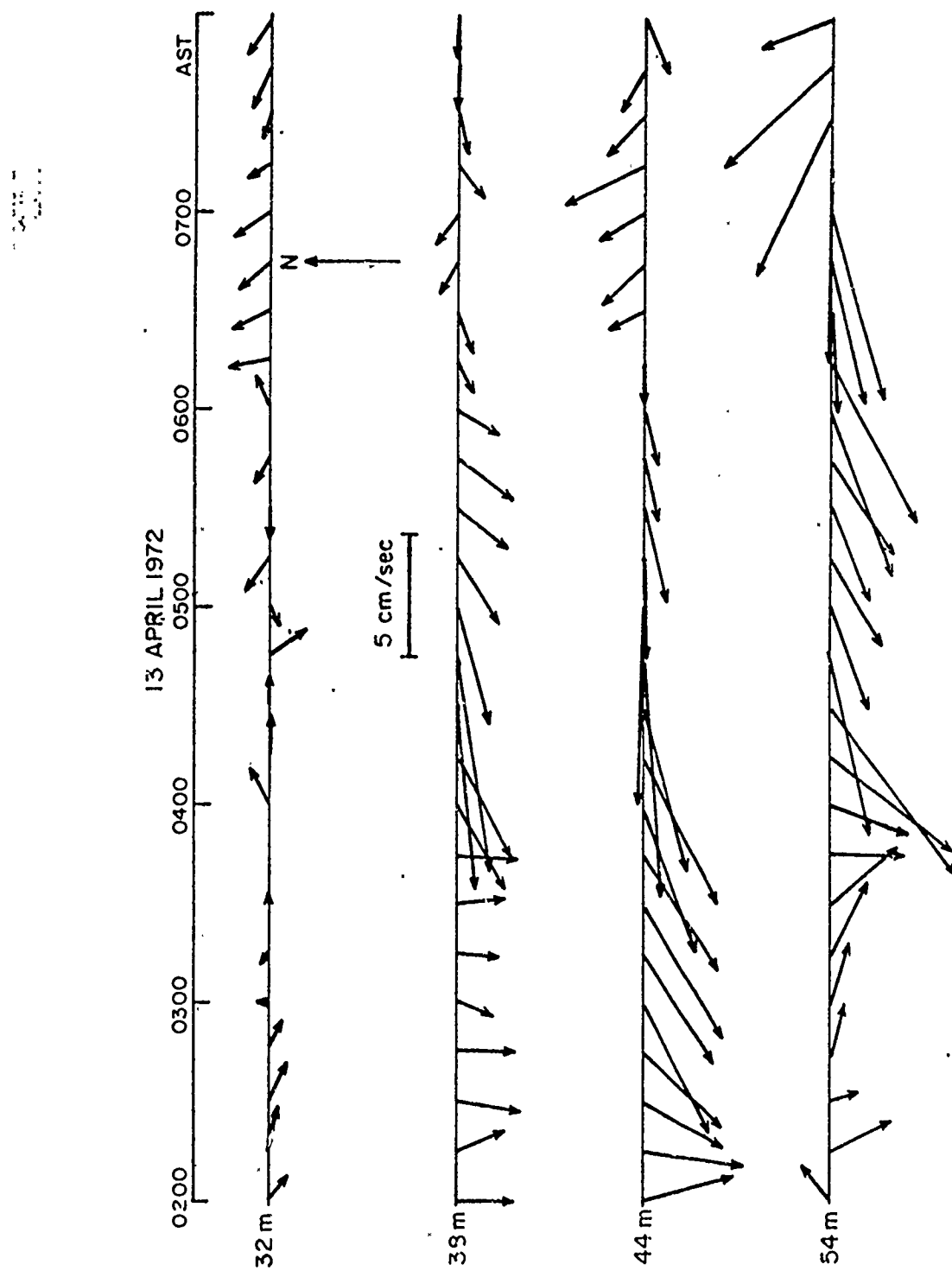
Fig. 10-6 Current vectors at four levels relative to the mean current at 32 m showing complicated baroclinic structure

11 CONCLUSIONS AND FINAL COMMENTS

11.1 The Total Stress on the Ice

In Section (7.5) we alluded to the contribution of form drag to the
total ice stress and deferred discussion until further results were pre-
sented. It has become apparent that the question of form drag and how to
treat it is one of the crucial problems in estimating both wind and water
stress on sea ice. Obviously, an ice model requires some sort of reliable
estimate for each. To this end, extensive measurements under varied con-
ditions are planned for the 1975 AIDJEX experiment hopefully to provide
drag coefficients that are functions of easily measured parameters.

F. A. Lee (1973, unpublished manuscript) has shown by modeling turbu-
lent flow without separation over a sinusoidal boundary under conditions
similar to flow under ice, that form drag determined by integrating the
surface pressure is comparable to skin friction. These results have been
substantiated by G. Spooner (personal communication) for arbitrary shapes
decomposed into Fourier components.

Arya (1973) has calculated the ratios of form drag per unit area to
surface friction for the upper ice surface, using observed values for
ridging intensity and a drag coefficient from laboratory flows over obsta-
cles similar to pressure ridges. He finds that in regions of fairly
intensive ridging, and particularly under stable stratification, form drag
can be quite significant even in the atmosphere, and suggests that in the
ocean form drag may completely dominate skin friction.

Hunkins (1974b) calculated average air stress at the AIDJEX site for

the afternoon of Apr. 12 and reports a magnitude of approximately 1.9 dynes-cm^{-2}. Clearly our skin friction estimate ($\sim$1 dyne-cm^{-2}) is a sizable portion of this. On closer investigation, however, Arya's method appears to give reasonable estimates. For instance, if we use his values for the drag coefficient (C_{Dn} = .4) and the dimensionless ridging intensity (R = .025), then for neutral conditions with an average underside ridge depth $\sim$ 3 m and $z_0 \sim$ .2 cm we get $F_D/\tau_D \sim$ 1 to 2 (see Arya, 1973, Figure 3). This might seem surprising but it should be noted that Ro_* for flow under the ice is considerably smaller than in the atmosphere and thus the roughness scale, z_0, is much larger in the ocean, other things being equal.

Unfortunately, we come up against a formidable problem in trying to describe a turbulent flow over varied topography, and at present we seem to be able to say only that the form drag is of the same order of magnitude as the skin friction. We can estimate the total stress by integrating the mean equations to get mass transport (this is discussed in detail in Hunkins, 1974b, Appendix; see also Faller and Mooney, 1971), but this requires that profiles be averaged over a representative surface area. We showed in Section (7.5) that the mean profile in any one location seems to be very sensitive to the particular topographic features of that point and questioned whether a suitable average is possible without sampling steady currents from every direction.

There is one feature in this, however, that should not be overlooked: the ice represents a rigid lid over a fairly large area compared to the depth of the boundary layer and thus the ice velocity is a representative average.

The significance of this becomes clearer if we consider the lateral (V) profile. First consider the following sketch depicting the lateral

from a neutral, horizontally homogeneous model (e.g., Wyngaard, et al.,
1973):
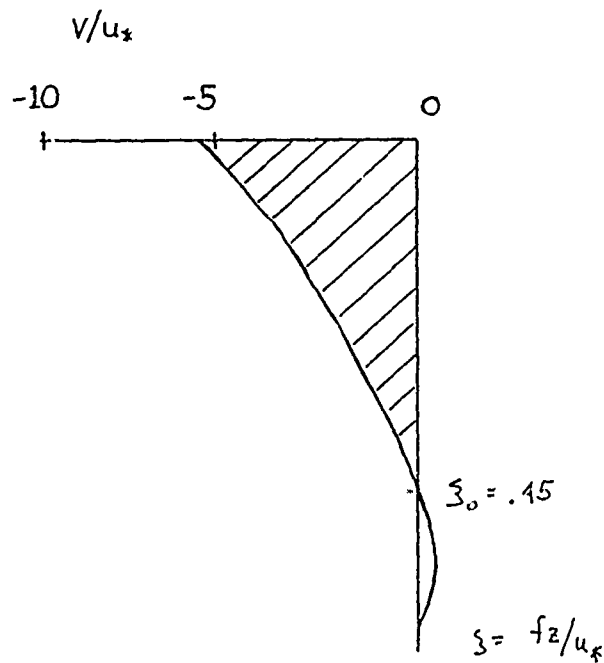
We can estimate the area under the curve by considering the triangle
with legs $\xi_0 = .45$ and $V/u_* = 5$. This illustration overestimates the stress,
τ_s/u_*^2, by about 10%, but demonstrates that a linear approximation for the
V profile is not too bad.

Next we superimpose curves from Hunkins' measurements and our own
sketched from hodographs in Figure (7-5).
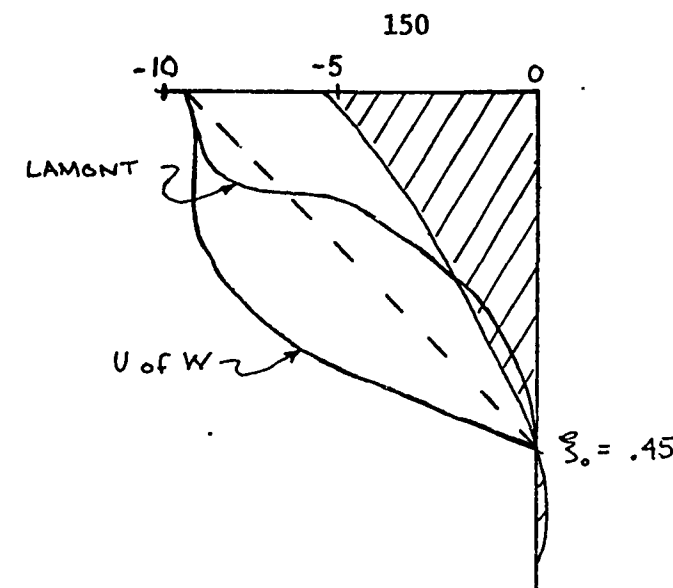
The upper value of the V curve at any location is clearly representative of the average throughout the region because of the rigidity of the ice. We then postulate the following:

(1) The point at which the V profile goes to zero is governed by the turbulent structure and is taken to be $\xi_0 = .45$, since the mixed layer is neutrally buoyant. In other words, the lower limit is set by the friction velocity, u_*. Although this cannot be proved, Figures (8-5) and (7-2) are strong supporting evidence. We assume that u_* does not vary greatly over the averaging region.

(2) Although V profiles may differ radically from point to point, the average over a large enough horizontal area can be crudely approximated by a straight line.

(3) The total non-dimensional stress can be related to the non-dimensional lateral velocity by a shape factor, γ, i.e., $\tau_b/u_*^2 = \gamma V_R/u_*$

The shape factor for the simple triangle with $\xi_0 = .45$ is
.22. By noting that in the horizontally homogeneous case,
$\tau_b/u_*^2 = 1$, we can round this to .2. Thus

$$\tau_b/u_*^2 = .2 \, V_R/u_*$$

It should be stressed that this shape factor is based more on intuition than evidence. We presume that on the average the V profile comes fairly close to a straight line from the surface to the depth of frictional influence, as it does in the horizontally homogeneous case. Our approximations may be crude, but they should be viewed in the context that even if our calculated stresses are wrong by 25% we would consider this a large improvement on other means available.

For reasonably steady conditions observed on Apr. 11 and Apr. 12, the total non-dimensional stress is approximately 1.9.

If $\underline{G}$ is the modulus of the reference velocity (equal to the absolute ice speed if no geostrophic flow is present) we can define a drag coefficient:

$$C_D = \tau_b/G^2$$

From our measurements

$$C_D \sim 3.4 \times 10^{-3}$$

If we accept this method of estimating drag as valid, an interesting implication is that stress can be estimated from relatively simple measurements. For instance, suppose the ocean is assumed still, i.e., geostrophic currents are small compared to the ice-drift velocity. Then the ice speed, G, and direction can be measured by navigation; u_* and the direction of water stress can be estimated from the mean measurements made in an area

of reasonably smooth ice at two locations in the log profile region, e.g.,
1 and 2 m. From these α can be determined and the stress calculated from
(11.1.1) with $V_R = G\sin\alpha$.
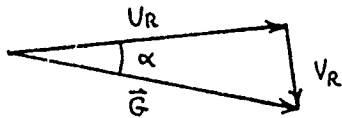
Alternatively, if α can be measured and u_* and z_0 estimated as above, U_R
can be calculated from the geostrophic drag law and the lateral velocity
given by $V_R = U_R \tan\alpha$. This method would require more extensive confirma-
tion of the downstream geostrophic drag law

$$U_R/u_* = \frac{1}{k}(\ln Ro_* - A)$$

since clearly we do not expect its homogeneous lateral counterpart

$$\frac{V_R}{u_*} = \frac{B}{k}$$

to hold. If this approach could be shown to work and the lateral coeffi-
cient, B, could be expressed empirically as, say, a function of the ridging
intensity, R, introduced by Arya (1974); then a geostrophic drag law might
be of considerable value. If, however, it is found that the density struc-
ture is not neutral except in isolated cases, obviously the problem is
more complicated and becomes analogous to the atmospheric case where both
diabatic effects and surface topography need to be considered.

The approach to estimating the overall stress outlined in this section
is offered as a practical alternative to the methods discussed in Chapter 7.
The assumptions on which it rests surely require more testing and hopefully
the 1975-76 AIDJEX experiment will provide such data.

11.2 Summary

The main features of this dissertation can be summarized as the following:

(1) The so-called mixed layer was found to coincide closely with the frictional boundary layer observed during maximum wind speeds and was very nearly dynamically neutral. This was confirmed by direct measurements and inferred from the dynamical properties of mean currents, Reynolds stresses and current spectra.

(2) The best estimate of the friction velocity, u_*, was determined from momentum flux measurements and consideration of the mean momentum equations. It agrees reasonably well with the value calculated by assuming a logarithmic mean profile to 4 m, even though the assumption is probably not justified in terms of surface layer theory. Stress estimated using a momentum-integral technique for the whole boundary layer gave a significantly higher value.

(3) With the important exception of lateral velocity, the profiles of mean current and Reynolds stresses, when non-dimensionalized by u_* and u_*/f, agreed quite well with recent atmospheric PBL models.

(4) The surface roughness, z_0, was found to be .18 cm from u_* and the mean velocity at 2 m (with k = .35). This implies a friction-velocity constant of .05; i.e., $u_* = .05\ U(2)$.

(5) Spectral analysis showed some evidence of an inertial subrange, although the Reynolds number of the flow was considerably smaller than in the atmosphere. Length scales associated with peaks in the weighted w-spectra were used to derive a K (eddy viscosity) distribution from the

relationship, $K \sim u_* \ell$, that agrees reasonably well with Deardorff's (1972) distribution. Contrary to common assumption however, there was no simple relationship between K and $\partial V/\partial z$ and $\overline{vw}$. Again this was attributed to inviscid topographic effects.

(6) Secondary currents at various levels in the pycnocline were observed and related to baroclinicity there. These were described heuristically by a spin-up argument and it was shown that such an argument could account for the increased salinity of the mixed layer observed as the storm developed.

(7) Finally, by assuming neutrally buoyant conditions and that the depth of the boundary layer was determined by the turbulent structure, the departure of the lateral velocity profile from what would be expected in the ideal horizontally homogeneous case was used to estimate the contribution of form drag to total drag. Form drag was found to be approximately the same (90%) as the skin friction drag and thus led to a total drag coefficient of 3.4×10^{-3}.

REFERENCES

Arya, S.P.S., Contribution of form drag on pressure ridges to the stress on arctic ice, _J. Geophys. Res., 78_, 7092-7099, 1973.

Arya, S.P.S., Neutral planetary boundary layer above a non-homogeneous surface, _Geophys. Fluid Dynamics_, 4, 335-355, 1973.

Batchelor, G.K., _An Introduction to Fluid Dynamics_, Cambridge University Press, London, 1967.

Batchelor, G.K., _The Theory of Homogeneous Turbulence_, Cambridge University Press, London, 1953.

Blackadar, A.K., and H. Tennekes, Asymptotic similarity in neutral planetary boundary layers, _J. Atmos. Sci._, 25, 1015-1019, 1968.

Blackman, R.P., and J.W. Tukey, _The Measurement of Power Spectra_, Dover Publications, New York, 1958.

Brown, R.A., A secondary flow model for the planetary boundary layer, Ph.D. dissertation, University of Washington, Seattle, 1969.

Brown, R.A., On the atmospheric boundary layer theory and methods, _AIDJEX Bull., 20_, 1-141, 1973.

Busch, N.E., J.A. Frizzola, and I.A. Singer, The micrometeorology of the turbulent flow field in the atmospheric surface boundary layer, _Acta Polytechnica Scandinavica (Physics including Nucleonics)_, 50, 1-45, 1968.

Busch, N.E., and H.A. Panofsky, Recent spectra of atmospheric turbulence, _Quart. J. Roy. Met. Soc., 94_, 132-148, 1968.

Businger, J.A., and S.P.S. Arya, The height of the mixed layer in the stably stratified planetary boundary layer, to appear in _Advances in Geophysics_, 1974.

Businger, J.A., J.C. Wyngaard, Y. Izumi, and E.F. Bradley, Flux-profile relationships in the atmospheric surface layer, J. Atmos. Sci., 28, 181-189, 1971.

Cooley, J.W., P.A.W. Lewis, and P.D. Welch, The finite Fourier transform, IEEE Transcations on Audio and Electroacoustics, AU 17, 77-85, 1969.

Csanady, G.T., Geostrophic drag, heat and mass transfer coefficients for the diabatic Ekman layer, J. Atmos. Sci., 29, 91-115, 1972.

Deardorff, J.W., Numerical investigation of neutral and unstable planetary boundary layers, J. Atmos. Sci., 29, 91-115, 1972.

Faller, A.J. and K.A. Mooney, The Ekman boundary-layer stress due to flow over a regular array of hills, Boundary Layer Met., 2, 83-107, 1971.

Holton, J.R., An Introduction to Dynamic Meteorology, Academic Press, New York, 1972.

Hsu, H.P., Fourier Analysis, Simon and Schuster, New York, 1967.

Hunkins, K., Ekman drift currents in the Arctic Ocean, AIDJEX Bull., 23, 9-36, 1974a.

Hunkins, K., The oceanic boundary layer and ice-water stress during AIDJEX 72, to appear in AIDJEX Bull., 1974b.

Jenkins, G.M., and D.G. Watts, Spectral Analysis and Its Applications, Holden-Day, San Francisco, 1968.

Kanasewich, E.R., Time Sequence Analysis in Geophysics, University of Alberta Press, Edmonton, 1973.

Lumley, J.L., and B. Khajeh-Nouri, Computational modeling of turbulent transport, to appear in Advances in Geophysics, 1973.

Lumley, J.L., and H.A. Panofsky, The Structure of Atmospheric Turbulence, Interscience, New York, 1964.

McPhee, M.G., and J.D. Smith, Flow in the vicinity of a small pressure ridge
keel, (abstract), EOS, Transcations of the American Geophysical Union,
53, p. 1012, 1972.

Martin, P., and A. Thorndike, Acoustic bottom referencing system, AIDJEX
Bull., 14, 59-60, 1972.

Mellor, G.L., and H.J. Herring, A survey of the mean turbulent field closure
models, AIAA Journal, 21, 590-599, 1973.

Monin, A.S., Weather Forecasting as a Problem in Physics, MIT Press, Cambridge,
Mass., 1972.

Morse, B.A., and J.D. Smith, Density structure of the mixed layer under multi-
year ice, EOS, Transactions of the American Geophysical Union, 53, p.
1011, 1972.

Neumann, G., and W.J. Pierson, Jr., Principles of Physical Oceanography,
Prentice-Hall, Inc., Englewood Cliffs, N.J., 1966.

Obukhov, A.M., Turbulence in an atmosphere with a non-uniform temperature,
Boundary Layer Met., 2, 7-29, 1971.

Panofsky, H.A., and C. Mazzola, Variances and spectra of vertical velocity
just above the surface layer, Boundary Layer Met., 2, 30-37, 1971.

Phillips, O.M., The Dynamics of the Upper Ocean, Cambridge University Press,
London, 1966.

Shir, C.C., A preliminary numerical study of atmospheric turbulent flows in
the idealized planetary boundary layer, J. Atmos. Sci., 30, 1327-1339,
1973.

Smith, J.D., Surface boundary layer study, AIDJEX Bull., 14, 40-43, 1972a.

Smith J.D., Upper ocean dynamics, proposal to the Office of Naval Research,
1972b.

Smith, J.D., Turbulent structure of the surface boundary layer in an ice-covered ocean, Proceedings of the 1973 ICES symposium on the physical processes responsible for the disposal of pollutants in the sea, with special reference to the near shore zone, Rapports et Proces-Verbaux series, Ed. by J.W. Talbot and G. Kullenberry, 1973.

Tennekes, H., The logarithmic wind profile, J. Atmos. Sci., 30, 234-239, 1973.

Tennekes, H., and J.L. Lumley, A First Course , Turbulence, MIT Press, Cambridge, Mass., 1972.

Welch, M., E. Partch, H. Lee, and J.D. Smith, Diving report, 1972 AIDJEX Pilot Study, AIDJEX Bull., 18, 31-44, 1973.

Wyngaard, J.C., O.R. Cote, and K.S. Rao, Modeling the atmospheric boundary layer, to appear in Advances in Geophysics, 1973.

Wyngaard, J.C., On averaging times, paper presented at Workshop on Micro-meteorology, 1973.

APPENDIX A

Velocity Conversion

Extensive calibrations of the meters used during the 1972 projects
were done at Harris Hydraulics Lab, University of Washington, in Feb.-
Mar., 1971. Those calibrations were best fit by straight-line segments
described by the following equation:

$$u = \begin{cases} 1.82f + 1.3 & .8 < f \leq 5 \\ 1.86f + 1.1 & 5 < f \leq 30 \\ 2.05f = 4.7 & f > 30 \end{cases}$$

where f equals 4 divided by the rotation period of a meter headon to the
flow.

Response of the meters to angle of attack (i.e., the angle the meter
makes with the streamline) can be described by the following:

$$f = f_m G(\cos \theta)$$

where f is the frequency to be used in the calibration equation, f_m is the
measured frequency and θ is the angle of attack (Smith, 1973).

$$G(\cos \theta) = \begin{cases} 1 & \cos \theta \geq .94 \\ 1.29(\cos \theta) - .21 & .84 < \cos \theta < .91 \\ .91 & \cos \theta \leq .87 \end{cases}$$

Given a triplet oriented arbitrarily to the flow, correction for angle
of attack involves an iteration scheme wherein first an uncorrected stream-
line is established, angles from the streamline are calculated for each
component, the components are corrected for angle of attack, a new stream-
line is established and the process repeated until the desired accuracy is

achieved. This procedure is quite time consuming, however, and should be simplified wherever knowledge of the flow allows it to be.

In our case we knew that the u_m and w_m components were at approximately 30° and 60° respectively to horizontal and that the strealine would always be nearly horizontal. Moreover, when turbulence measurements were made the masts were oriented so the u_m and v_m were nearly equal. Thus it could be said with reasonable certainty that the angles of attack of u_m and w_m were always greater than 30°. In the simplified scheme actually used for velocity conversion, the following procedure was used:

$$u_H/v_m \doteq (f_u/\cos 30°)/f_v$$

Let $\beta = (f_u)_m/(f_v)_m$, $\beta \doteq u_H \cos 30°/v$

$$f_v = \begin{cases} (f_v)_m & \beta < .31 = \tan 20° \cos 30° \\ .91 (f_v)_m & \beta > .49 = \tan 30° \cos 30° \end{cases}$$

In between f_v varies linearly with β, i.e., $f_v = (1.27 - .56 \beta) f_{vm}$. Although this is a compromise between computing time and accuracy it is considered to be at least as accurate as the more basic supposition of current meter response to angle of attack.

The final step in velocity conversion was to smooth the step-functions resulting from redundant data on the slower-turning meters linearly. It was supposed that this would more closely approximate the true velocity field and might affect the calculated turbulent stresses. In practice it was found to have little effect except at very low velocities, for which Reynolds stress calculations were questionable anyway.

APPENDIX B

Vector and Tensor Rotation

In order to rotate the mean flow vector and Reynolds stress tensor
into the co-ordinate system used in Chapter 8 from the experimental frame
of reference described in Chapter 2, a cosine matrix is calculated from
the conditions that the mean vertical velocity at each triplet is zero
over the averaging time and that the surface stress is aligned with the
mean flow at 2 m. Thus we can break the complete rotation into two steps.

First we rotate the measurement reference frame about the horizontal
(y_m) axis so that $u_i' = a_{ij}' u_j^m$, $\bar{w}' = 0$
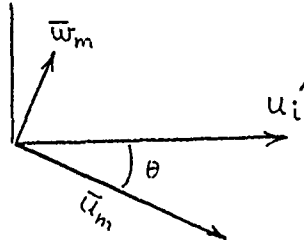
$$\theta = \tan^{-1}(\bar{w}_m/\bar{u}_m)$$

for each triplet.

Next we rotate the primed system about its vertical (z') axis so that
the average v- component <u>at 2 m</u> is zero:
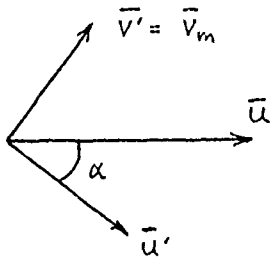
$$\alpha = \tan^{-1}\left(\frac{\bar{v}_m(2)}{\bar{u}'(2)}\right)$$

These two operations can be combined into one rotation matrix so that
any instantaneous vector is given by

$$u_i = a_{ij} u_j^m$$

and

$$A = \begin{bmatrix} \cos\alpha \cos\theta & \sin\alpha & \cos\alpha \sin\theta \\ -\sin\alpha \cos\theta & \cos\alpha & -\sin\alpha \sin\theta \\ -\sin\theta & 0 & \cos \end{bmatrix}$$

If $R_{ij}{}^{(m)}$ is the Reynolds stress component in the measurement frame of reference,

$$R_{ij} = a_{ik} a_{jl} R_{kf}{}^{(m)}$$

or in matrix notation:

$$[R] = [A][R^m][A]^T$$

APPENDIX C

Calculation of Spectra

The Fourier transform of a continuous function of time, $X_i(t)$, is usually defined by

$$A(f) = \int_{-\infty}^{\infty} x_i(t) \, e^{-2\pi i f t} dt$$

If $X_C(t)$ is sampled at discrete intervals of time, Δt, for N samples, then $X(j) = X_i(j\Delta t)$, $j = 0, 1, \ldots, N-1$; and the discrete Fourier transform (DFT) is

$$A(n\Delta f) = \Delta t \sum_{j=0}^{N-1} X(j) \, e^{-2\pi k n \Delta f j \Delta t}$$

If the basic frequency interval is chosen $\Delta f = 1/N\Delta t = 1$, the DFT is given by

$$A(n) = \frac{1}{N} \sum_{j=0}^{N-1} X(j) e^{-2\pi i n j/N}$$

Adopting the notation of Cooley, et al. (1969), the DFT pair is

$$A(n) = \frac{1}{N} \sum_{j=0}^{N-1} X(j) W_N^{-nj}$$

$$X(j) = \sum_{j=0}^{N-1} A(n) W_N^{nj} \tag{C-1}$$

$$W_N = e^{2\pi i/N}$$

From the properties of W_N it follows that $A(n)$ and $X(j)$ are cyclically redundant, i.e., $A(n) = A(n+kN) = A(-n)$, $X(j) = X(j+kN) = X(-j)$. Under these conditions the DFT has many easily proved properties analogous to those for continuous Fourier transform pairs. A few of these properties are listed here without proof; for straightforward derivations see Cooley,

et al. (1969).

Let $X(j) \leftrightarrow A(n)$ be a DFT pair (the symbol $\leftrightarrow$ represents the trans-form operations (C-1)). Also let $X(j)$ be real. Then $A(-n) = A^*(n)$ where $A^*(n)$ is the complex conjugate of $A(n)$ and

$$\frac{1}{N} \sum_{k=0}^{N-1} X(k)X(k+j) \leftrightarrow A(-n)A(n) = |A(n)|^2 \qquad (C-2)$$

The left-hand side of (C-2) can be identified as the discrete counter-part of the autocovariance function for the series $X_c(t)$. Thus the DFT of the autocovariance function is the absolute square of the DFT of the origi-nal series, allowing us to estimate the spectrum by taking the absolute square of the transform of the velocity series, rather than calculating and transforming the autocovariance function.

Parseval's Theorem follows directly from (C-2) by setting $j = 0$:

$$\frac{1}{N} \sum_{k=0}^{N-1} |X(k)|^2 = \sum_{n=0}^{N-1} |A(n)|^2$$

If $X(k)$ is a turbulent velocity component, the mean square of the velocity fluctuations is equal to the sum of the spectral components. Clearly this is twice the turbulent kinetic energy in that component divided by the density.

Finally, if $X(j)$ is even (and real), then $A(n)$ is real and even. Since the autocovariance function is real and even, we can represent its transform on the positive wave-number axis as the one-sided power spectrum $A^0(n) = 2A(n)$.